UNIVERSITÀ
DEGLI STUDI
FIRENZE

DOTTORATO DI RICERCA IN FISICA E ASTRONOMIA

CICLO XXXI

COORDINATORE Prof. D'Alessandro Raffaello

Mass imbalanced Fermi mixtures with 2- and 3- resonant interactions

Settore Scientifico Disciplinare Fis/03

Dottorando
Dott. Neri Elettra

Tutore
Dott. Zaccanti Matteo

Supervisore
Prof. Inguscio Massimo

Coordinatore
Prof. D'Alessandro Raffaello

Anni 2015/2018

A Valter e Matilde, per aver saputo insegnare
il valore delle domande.
"Di che colore è il nulla?".

Contents

Abstract

In this thesis I discuss the design and realization of a new experimental apparatus aiming at the production of a novel ultracold mixture of ^{6}Li and ^{53}Cr fermionic atoms. This goal is motivated by the fascinating prospects offered by the introduction of a mass asymmetry in strongly-correlated fermionic matter, expected to enable the investigation of a wealth of exotic new regimes, both at the few- and many-body level. Among a few other possibilities, our specific choice is triggered by two unique three-body properties, unforeseen thus far, expected at the Cr-Li mass ratio, $M_{Cr}/m_{Li} \sim 8.8$: On the one hand, this mixture is predicted to support a weakly-bound universal trimer state [1], which in turn may enable the resonant control of elastic three-body interactions on top of the standard two-body ones, in the vicinity of a heteronuclear Feshbach resonance. On the other hand, for repulsive interactions, such a bi-atomic combination is predicted to feature an extraordinary suppression of inelastic pairing processes [2], making such an ultracold system an ideal playground for the experimental investigation of ferromagnetism in strongly repulsive Fermi gases.

Given that this represents the first attempt to realize an ultracold chromium-lithium mixture, my project had to face the difficulty of devising and implementing a novel apparatus without the possibility to rely on any pre-established theoretical result nor experimental scheme. Additionally, while ^{6}Li Fermi gases are routinely produced in many laboratories worldwide, much less is known about the ^{53}Cr atom, which has been cooled down to quantum degeneracy only very recently and in one single laboratory [3]. In particular, the relatively low natural abundance of the ^{53}Cr isotope, its rich hyperfine and Zeeman structure and a rather strong light assisted collision rate [4] are known factors that limit the overall efficiency of optical cooling and trapping techniques, which need a complex laser setup to be implemented. Further

complications are introduced by the high chemical reactivity of the chromium element, which requires special care in choosing the proper materials for the vacuum and effusion cell setups. For these reasons, only recently we could complete the construction of the experimental apparatus and start to produce Cr-Li mixtures in the cold regime. In particular, within the last months of my PhD I was able to realize cold mixtures of ^{52}Cr-^{6}Li and to investigate their collisional stability. This study, which focused on the more abundant and easy-to-handle bosonic ^{52}Cr isotope, together with fermionic ^{6}Li atoms, has represented a simpler but important playground, before moving to the more challenging case of ^{53}Cr-^{6}Li Fermi mixtures, currently under investigation in the lab.

This thesis is structured as it follows:

- Chapter 1 outlines the motivations which triggered the setup of a new experimental apparatus for the production of Cr-Li mixtures. After a first general introduction to the physics of ultracold collisions and Feshbach resonances in atomic gases, the chapter provides a synthetic overview of the various phenomena that can be potentially addressed with this novel platform, encompassing both few- and many-body regimes.

- Chapter 2 presents in detail the vacuum apparatus that I designed and implemented within the first part of my PhD. The chapter also reports on the assembly and backing procedure followed to implement the final structure, and to reach ultra high vacuum conditions in the setup.

- Chapter 3 presents instead the spectroscopic properties of the Li and Cr isotopes considered in this work, namely the fermionic ^{6}Li, bosonic ^{52}Cr and fermionic ^{53}Cr, respectively, and details the optical setup devised and implemented to laser cool Li and Cr atoms. The chapter also provides an overview of the high-power bichromatic optical-dipole-trap (ODT) setup, already installed on the apparatus, which will allow to trap and cool the mixture down to the ultracold regime via evaporative and sympathetic cooling techniques. In particular, during the last year of my PhD we devised and tested a simple scheme that enables to obtain a high-power ODT free from thermal lensing effects. This part of my thesis work is summarized in Ref. [5], which is reported in Appendix C.

- The first experimental results attained with the apparatus that I designed and implemented during my PhD activity are presented in chapter 4. These results consist in the individual and simultaneous realization of cold clouds of ^{6}Li and ^{52}Cr atoms within a double species magneto-optically trap (MOT). As the lithium is concerned, the chapter also presents the first experimental results relative to the implementation of gray-molasses cooling routines operating on the D1 atomic line. The chapter also reports on the possibility to store in the MOT magnetic quadrupole large clouds of ^{52}Cr atoms within D metastable states. Finally, I present the first experimental realization and characterization of double-species MOTs of Cr and Li atoms, achieved during the last months of my PhD.

- In chapter 5 I report on the analysis of unpublished data on ^{6}Li superfluid mixtures at the BEC-BCS crossover, which I carried in collaboration with the lithium team at LENS, in parallel with the main activity on the Cr-Li machine. This latter study aims to investigate the superfluid and normal currents within a thin atomic Josephson junction, realized by splitting ^{6}Li superfluids clouds in two reservoirs through the imprinting of a 2μm thick optical barrier. Onset of dissipative flow exceeding the maximum Josephson current has been characterized under different configurations of barrier heights and initial energy mismatch between the two reservoirs, enabling to extract the critical values of particle imbalance beyond which dissipative dynamics is established. The critical boundaries between coherent and dissipative regimes wer experimentally determined both in the BEC and the crossover regimes. Collaborating with the team of Prof. N. Proukakis in Newcastle, we could obtain a direct comparison of my experimental BEC results with numerical simulations, which is the summarized in Ref. [6], currently under revision.

Chapter 1

From few to many interacting fermions: a basic introduction

This chapter aims to outline the motivations which triggered the setup of a new experimental apparatus for the production of Cr-Li mixtures. As I will show, the physics that can be potentially addressed by this novel platform is very wide, and it ranges from the few- to the many-body regime, with the existence of elusive trimer states unobserved so far, and the possible emergence of exotic and normal many-body regimes of strongly correlated fermionic matter.

The chapter is structured as it follows: Sec. 1.1 describes the basic concepts underlying the physics of ultracold collisions and Feshbac resonances. Sec. 1.2 summarizes the properties of a many-body system, recalling in particular the BEC-BCS crossover scenario and the topic of fermionic superfluidity. Sec. 1.3 briefly discusses the debated topic of *exotic* superfluidity, namely the emergence of superfluid phases beyond the standard Bardeen-Cooper-Shrieffer theory, and in particular the possibility to experimentally address such elusive regimes with mass imbalanced mixtures.
In Sec. 1.4 I move to the physics of repulsive Fermi mixtures and itinerant ferromagnetism. I will present here the Stoner instability, namely the instability of a paramagnetic two-component Fermi mixture against phase separation into polarized domains. In this section I will highlight the difficulties connected with the experimental realization of the Stoner model with homonuclear gases, and the beneficial role of mass asymmetry.
Finally, Sec. 1.5 focuses on few-body systems, and their general properties for generic mass rations. I will then outline how the peculiar Cr-Li mass

ratio potentially enables the unprecedented tunability of interactions on top of the standard two-body ones. I will finally discuss the possible impact of such few-body features at the many-body level, both within the attractive and repulsive regime.

1.1 The 2-body scattering problem and the Feshbach resonance phenomenon

Ultracold atomic gases are characterized by an exceptional degree of control on a large number of experimental parameters, which renders such systems extremely suited both for investigating major phenomena of many-body physics, and for probing subtle and elusive regimes of few particle ensembles. This section is dedicated to one of the most powerful tools provided to this end by ultracold atomic gases, namely the possibility to controllably tune the interparticle scattering properties thanks to the Feshbach resonance phenomenon. The section provides a brief introduction to the physics of elastic 2-body collisions within the low-energy regime, and outlines the main concepts underlying the derivation of such exceptional phenomenon.

Within the center of mass frame, the two-body scattering problem is described by the following Schrödinger equation

$$\left(\frac{\hbar^2\nabla^2}{2\mu} + V(\mathbf{r})\right)\Psi(\mathbf{r}) = E\Psi(\mathbf{r}) \tag{1.1}$$

for the single particle of reduced mass μ. Asymptotically far from the scattering center, the eigenfunctions of Eq. (1.1) take the form

$$\Psi(\mathbf{r}) \propto e^{ikz} + f(\theta, k)\frac{e^{ikr}}{r} \tag{1.2}$$

identifying the superposition of an outgoing plane wave along the longitudinal direction z, and a scattered radial wavefront with amplitude $f(\theta, k)$ (see sketch in Fig. 1.1). It is a well-known result of textbook scattering theory [7] that, for a short-range central potential $V(\mathbf{r}) \sim r^{-n}$ the scattering amplitude f can be expressed as a partial wave expansion in terms of phase shifts δ_ℓ, being ℓ the partial wave angular momenta. For $n > 3$, it can be shown that $\delta_l \sim k^{2\ell+1}$ as $k \to 0$. Then, at low temperature, the unique relevant contribution to the scattering amplitude is given by δ_0 (s-wave scattering). This great

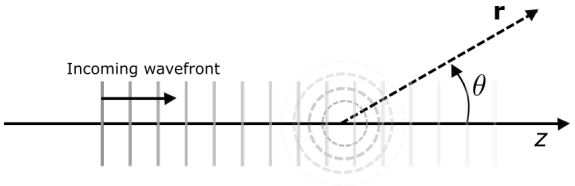

Figure 1.1: Sketch of the scattering process within the center of mass frame: a fictitious particle of mass μ (reduced mass) impacts on a fixed scatterer potential. The amplitude of the scattered wavefront is determined by the scattering amplitude f as a function of the scattering angle θ.

simplification of the scattering problem fully applies to non-dipolar atomic systems in the dilute regime, where interatomic interactions are mainly described by van der Waals potentials $V_{vdW}(r) \propto -r^{-6}$. Under ultracold conditions the range associated to such potentials is $r_{VdW} \ll k^{-1}$ [8], and the entire scattering problem reduces to the knowledge of the s-wave scattering amplitude

$$f_0(k) = -\frac{1}{k\cot(\delta_0) + ik} \simeq -\frac{1}{\frac{1}{a} + R^* k^2 + ik} \tag{1.3}$$

where the term $\cot(\delta_0)$ has been expanded to the second order in k. Under these conditions, the 2-body scattering problem results to be fully described in terms of only two parameters, the *scattering length* a and the *effective range* R^* [8–10].

It can be shown that the far field behavior of the scattered radial wavefunction $\chi(r) = \Psi(r)/r \sim \sin(kr - \delta_0)$, solution of the low-energy isotropic scattering problem, can be retrieved by imposing the well-known Bethe-Peierls boundary condition at $r = 0$ [9–11]

$$\frac{\chi'(0)}{\chi(0)} = k\cot(\delta_0) \simeq -\frac{1}{a} - R^* k^2 \tag{1.4}$$

In turn, this is the equivalent to approximate the (real) interaction term $V(r)$ in (1.1) by an effective contact potential $V_{eff} = \frac{4\pi\hbar^2}{2\mu}\delta(r)\partial_r(r\cdot)$ (zero-range approximation).

This approach is fully valid in the dilute and ultracold regime, where the large interparticle distances and the very low momenta at play render short-range effects inessential for an accurate description of 2-body scattering.

Aside for the scattering states, it can be shown that the contact potential associated with the scattering amplitude Eq. (1.3) can sustain a bound

molecular state for $a > 0$. Its energy is obtained by looking for the pole of $f_0(k)$ imposing $k \to i\kappa$, with κ real and positive. This is given by

$$\kappa = \frac{\sqrt{4R^*/a + 1} - 1}{2R^*} \tag{1.5}$$

This solution is admitted only for $a > 0$. It corresponds to a bound state with negative energy $E_B = -\hbar^2\kappa^2/2\mu$, described by the localized wavefunction $\chi(r) \propto e^{-\kappa r}/r$. Eq. (1.5) highlights a rather general fact: the value of the scattering length generically depends upon the existence of a real ($a > 0$) or virtual ($a < 0$) bound state near the scattering threshold $E = 0$. In particular, the scattering can become resonant - i.e. $\delta_0 = \pi/2$ and $1/a = 0$ - once the two-body bound state hits the collision threshold. This is a very general result of scattering theory (Levinson's theorem) and it can be better realized by noticing that Eq. (1.3) can be recast in the form

$$f(k) = -\frac{\hbar\gamma/\sqrt{2\mu}}{E^2 - E_{res}^2 + i\gamma\sqrt{E}} \tag{1.6}$$

This is the Breit-Wigner expression for the scattering amplitude in the presence of a quasi-discrete level E_{res}, coupled to the scattering channel by a coupling strength γ. As it can be straightforwardly verified, a and R^* in Eq. (1.3) are linked to γ and E_{res} in Eq. (1.6) via the relations

$$a = -\frac{\hbar\gamma}{\sqrt{2\mu}E_{res}}; \tag{1.7a}$$

$$R^* = \frac{\hbar}{\sqrt{2\mu}\gamma} \tag{1.7b}$$

In particular, one can notice how a is related to the energy of the bound (virtual) state, $a > 0$ ($a < 0$) corresponding to $E_{res} > 0$ ($E_{res} < 0$). R^* instead solely depends on γ, with strong coupling leading to small values of the effective range and vice versa.

Notably, from Eq. (1.7)(a) one can notice how the control of E_{res} directly enables the tunability of the scattering length. This is precisely what happens in correspondence of a Feshbac resonance: at a certain magnetic field B_0, the scatering threshold associated with a certain combination of the Zeeman sublevels of the atomic pair (open) channel becomes degenerate with a molecular state supported by a different (closed) channel. In this case

$E_{res} = \delta\mu(B - B_0)$, where $\delta\mu$ is the difference between the magnetic moments featured by the close and open channel, respectively. The scattering length than reads $a = -\frac{\hbar\gamma}{\sqrt{2\mu}\delta\mu(B-B_0)}$, which is usually expressed as

$$a = -a_{bg}\left(\frac{\Delta B}{B - B_0}\right) \tag{1.8}$$

where a_{bd} stems for the background (non-resonant) value away from the resonant condition $B = B_0$, and ΔB indicates the width of the Feshbach resonance. In turn, $R^* = \frac{\hbar^2}{2\mu a_{bg}\Delta B\delta\mu}$.
The dependence (1.8), and the possibility to resonantly tune the scattering properties associated to the 2-body system, are the key hallmark of the Feshbach resonance phenomenon.

The energy E_B associated to the bound state supported by the contact potential, see Eq. (1.5), can be tuned according to Eq. (1.8). In particular, for $R^*/a \gg 1$, Eq. (1.5) implies that $E_B \sim \hbar^2/2\mu a R^* = \delta\mu(B - B_0)$, with the bound state energy approaching that of the closed channel molecule. Close to the Feshbach resonance instead, where the scattering length (1.8) diverges ($R^*/a \to 0^+$), it is $E_B \sim \hbar^2/2ma^2$. Here, both the bound state energy and wavefunction are called "universal", since they are solely determined by of the scattering length and do not depend on the short-range details of the specific interparticle potential. The transition from one limit to the other strongly depends on the value of R^* [8]. Very generally, if $R^* \ll r_e$, being r_e the typical interaction range associated to the real scattering potential V (for example, the van der Waals length r_{VdW} for V_{vdW}), than the transition takes place at $|B - B_0| \sim \Delta B$. The scattering problem is uniquely described by a within a wide range around resonance, and the second order term in (1.3) and (1.4) can be neglected. In this case, the Feshbach resonance is said to be *broad*. On the contrary, if $R^* \gg r_e$, the transition happens much closer to resonance, for $|B - B_0| \ll \Delta B$. In this case, the resonance is said to be *narrow*, and the thorough description of the scattering problem requires essentially always to account for the k-dependence of the scattering amplitude.

1.2 The many-body problem: a toy model

The present section moves the attention from the few- to the many-body regime, considering the impact of 2-body resonant interactions onto a system

composed by N interacting fermions.
A very simple and qualitatively correct picture of such many-body problem is produced in the theoretical work of Ref. [12]. Here, the authors consider two fermions, with identical mass m and opposite spin, confined in a spherical box of radius R (see Fig. 1.2). In such a model, the presence of the N-2 remaining fermions is encoded within the box size, with the hardwall condition at $r = R$ mimicking the effect of Pauli blocking in the limit of low momenta (long wavelenghts).

For the non-interacting case, the system is described by the trivial radial wavefunctions $\chi_n(r) = A \sin(k_n r)$ for the single particle with reduced mass $m/2$, being $A = (2\pi R)^{-1/2}$ the renormalization factor in 3D, and k_n the quantized wavevactors defined as

$$k_n = \frac{\pi}{R} n \qquad n \in N \tag{1.9}$$

The corresponding eigenenergies are then defined as $E_n = \hbar^2 k_n^2/m$. In particular, the ground state energy E_1 and the Fermi energy $E_F = \hbar^2 k_F^2/2m$ can be linked by the following relation for the mean energy per particle

$$\frac{E_1}{2} = \frac{3}{5} E_F \tag{1.10}$$

which connects the box size R and the non-interacting Fermi wavevector k_F:

$$R = \left(\frac{5}{3}\right)^{1/2} \frac{\pi}{k_F} \tag{1.11}$$

Introducing now the zero-range interaction $V_{eff} \propto \delta(r)$ presented in Sec. 1.1, the system will be described by a new set of wavevectors $\{k'_n\}$ fulfilling the Bethe-Peierls condition (1.4). For a radial wavefunction of the form $\chi'_n = A \sin(k'_n(r - R))$, the condition reads:

$$-k'_n \cot(k'_n R) = k'_n \cot(\delta_0(k'_n)) = -\frac{1}{a} \tag{1.12}$$

where k^2 terms in the scattering amplitude have been neglected (broad Feshbach resonance regime, $R^* = 0$). The solutions of Eq. (1.12), together with relation (1.11), define the eigenenergies $E'_n = \hbar^2 {k'_n}^2/m$ as a function of the interaction strength parameter $-1/k_F a$. The behavior of the ground state and

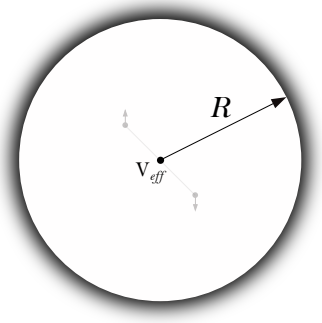

Figure 1.2: A particle of reduced mass $m/2$ colliding with a fixed scatterer at the center of the box mimics the scattering problem of the two particles with mass m. Adapted form Ref. [12].

the first excited state as a function of $-1/k_F a$ is shown in Fig.1.3, together with the two lowest solutions of the non-interacting system.

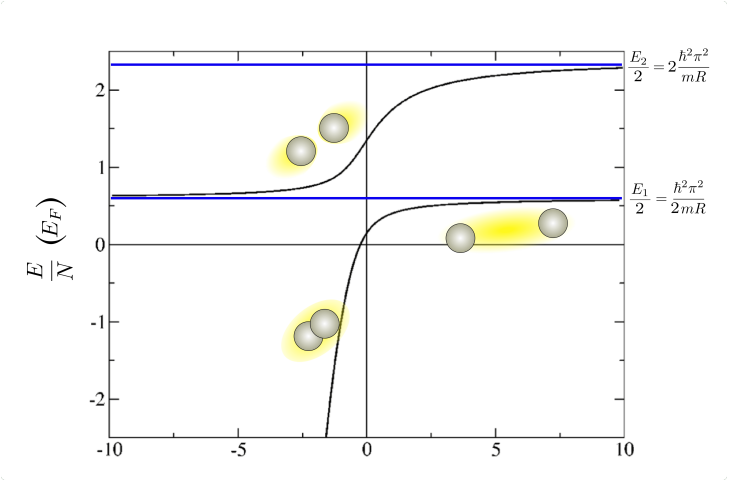

Figure 1.3: Energy per particle rescaled to the Fermi energy $E_F = \frac{\hbar^2 k_F^2}{2m}$ as a function of $-1/k_F a$, for the interacting (black) and non-interacting (blue) system according to the toy model of Ref. [12]. Only the first two energy branches are plotted. A cartoon mimics the behavior of the two interacting particles. Adapted from Ref. [12].

Interestingly, each energy branch E'_n lays below the corresponding non-interacting one E_n. In particular, for $a < 0$ (right side of the plot) the relation (1.12) admits real and positive solutions of the form $k'_n = n\pi - \delta_0$. From this, it is straightforward to show that the energy shift between the

interacting and the non-interacting states reads $E'_n - E_n \simeq -2E_n/R^2$ up to the second order in k_n [13]. Recalling that it is $|\phi_n(r)|^2 = |\frac{\chi_n(r)}{r}|^2 \xrightarrow[r\to 0]{} \frac{k_n^2}{2\pi R}$ for the non-interacting (radial) eigenfunction, the energy shift per particle can be recast as:

$$\frac{E'_n - E_n}{2} \simeq \frac{2\pi\hbar^2 a}{m} \cdot |\phi_n(0)|^2 \tag{1.13}$$

Eq. (1.13) is the analogous of the familiar mean-field interaction term in the Gross-Pitaevskii equation (GPE) [14], except for a factor 2^{-1}, as it must be for the case of two fermionic, rather then bosonic, particles.
In this regime the fermions experience a weak mutual attraction, as implied by the negative energy shift Eq. (1.13), vanishing as $a \to 0^-$.

By increasing the phase shift up to the resonant limit, $-1/k_F a \to 0$, Eq. (1.12) reduces to $k_n \cot(k_n R) = 0$. Remarkably, the value of the scattering length drops out of the problem, and the system energy solely depends on the box size R. The latter condition implies that $k_n R = \pi/2$, which yields an energy $E'_1 = E_1/4$ for the ground state.

On the left side of the plot, where $a > 0$, a specific value of the scattering length can be found, beyond which the relation (1.12) admits a solution for $k = i\kappa$, with κ real and positive. Such a solution corresponds to the emergence of a bound state with negative energy $E'_1 = -\hbar^2\kappa^2/m$.
In particular, in the limit $a \to 0^+$, relation (1.12) implies that it is $\kappa \to a^{-1}$, yielding $E'_1 \sim -\hbar^2/ma^2$. This corresponds to the limit derived in Sec. 1.1 for the binding energy of the Feshbach dimer in vacuum and in the broad resonance limit. In this case, fermions form tightly bound pairs described by exponential decaying wavefunction of the form $\propto e^{-r/2a}$, with $a/R \ll 1$. Owing to its small size, the dimer binding energy does not depend on the boundary conditions at $r = R$.

The first excited state of the interacting system shows instead a positive energy larger than E_1, which progressively increases when starting from $a \to 0^+$ and moving to $-1/k_F a \to 0$, asymptotically reaching the non-interacting value E_2 for $a \to 0^-$. This excited branch corresponds to two repulsively interacting fermions, with the repulsive strength increasing as a is varied from positive (left side of the plot) to negative (right side) values.

Although retrieved on the basis of a very simple toy model for describing the many-body system, the trend of the two energy branches in Fig. 1.3 is qualitatively valid. In a more complete treatment for the N-body prob-

lem, the lowest branch in Fig. 1.3 corresponds to the so-called *BEC-BCS crossover* [15,16]. Following this branch at T=0, the system can be adiabatically tuned from a weakly interacting condensate of bosonic molecules - the Bose-Einstein condensate (BEC) limit $k_F a \to 0^+$ - to a superfluid of weakly attractive pairs - the Bardeen-Cooper-Schrieffer (BCS) limit $k_F a \to 0^-$. As captured by the simple model presented above, in the BEC limit the dimer size is very small with respect to the interparticle distance ($a/R \ll 1$), and the associated energy is well described by Eq. (1.5) for the bare 2-body problem. Moving to the BCS side the dimer size increases, and eventually exceeds the interparticle spacing ($k \sim 1/a \gg R$). In this regime the system mimics the behavior of superconducting electrons, where fermions lying near the Fermi surface pair up through the Cooper pairing instability.
Finally, at resonance ($-1/k_F a \sim 0$), the system lies in the so-called unitary regime. Here the gas exhibits a universal character, the scattering length dropping out of the problem. As predicted by the box model, the system energy is here a positive fraction of the non-interacting energy. In particular it is found that $E_1' = \xi E_1$, being $\xi = 0.37$ the Bertsch parameter [17].

At present there is no exact theory able to quantitatively describe the many-body system throughout the BEC-BCS crossover. In the BEC limit, the weak dimer-dimer interaction can be approximated by a zero-range potential between point-like bosons of mass $2m$, with scattering length $a_{DD} = 0.6a$ [18]. Within a mean-field treatment this leads to the bosonic analogue of the interaction term Eq. (1.13) within the GP-equation for the (scalar) superfluid order parameter [14].
Moving to the BCS limit across unitarity, a scalar description is no longer sufficient to capture the emergence of the dimers composite nature. The system can be here modeled by the mean-field Bogoliubov-De Gennes (BDG) equations. These are spinorial equations for a two-component Fermi gas where the off-diagonal terms of the Hamiltonian account for the inter-species pairing interaction [19, 20] (see also Ch. 5 for further discussion and references).

Within this frame, Feshbach resonant atomic Fermi gases emerge as a unique framework enabling to experimentally address the smooth evolution between the two paradigmatic regimes of superfluidity, testing the validity of different theoretical approaches. Furthermore, these systems also allow the experimental investigation of the pairing mechanism itself, which originates the superfluid constituents and enables their condensation into a gapped phase, eventually in the presence of asymmetric Fermi gases. Sec. 1.3 generally introduces the debated topic of pairing mechanisms beyond the standard

BCS theory, in view of their experimental investigation within the Cr-Li platform presented in this work.

Besides the attractive branch, Feshbach resonances also allow for the investigation of repulsive Fermi gases along the upper branch of the many-body system. Here the repulsive interaction may lead to ferromagnetic instability and nucleation of polarized spin domains. Sec. 1.4 is dedicated to such repulsive phases and to their inherent instability against inelastic decay onto the lower-lying attractive branch. I will show in Sec. 1.5 how unprecedented few-body features predicted for the peculiar case of Cr-Li Fermi mixtures possibly hinder the pairing instability and open up new routes towards the experimental achievement of long lived ferromagnetic phases.

1.3 Fermionic superfluidity beyond standard BCS theory

As anticipated in Sec. 1.2, the emergence of a superfluid phase within a many-body fermionic system is understood in terms of the standard BCS theory, which predicts that two identical fermions, with opposite spin and momentum projection and lying at a common Fermi level, pair up in a bosonic quasiparticle -the Cooper pair- in presence of any (small) mutual attraction. The theory was first introduced [21] to explain the non-dissipative electron currents, the Meissner effect [22] and the specific heat divergence appearing in certain superconducting materials below a characteristic temperature: in such systems, the effective electron-electron attraction is induced by the exchange of virtual phonon modes of the substrate crystal, which compensates and eventually exceeds the screened short-range Coulomb repulsion [23, 24]. Within an intuitive picture, the bosonic nature of the Cooper pairs then allows for their condensation into a gapped phase, which is intimately connected to the presence of a macroscopically occupied energy state [25].
Although standard BCS theory does not apply to the case of two non-degenerate Fermi levels, supercurrents are still observed under such conditions in a variety of electronic systems: high-Tc (II) superconductors show non-dissipative currents even in presence of high magnetic fields, which foster a spin population imbalance (and thus a mismatch in the two components Fermi energies) by spin-polarizing the conductive electrons. Other celebrated examples are found in quantum chromodynamics, which predicts the exis-

tence of exotic superfluid phases within the quark matter composing the early universe and in the core of neutron stars [26,27]: here a mismatch among the Fermi energy of the different components is introduced by the mass asymmetry between quarks of different flavors.

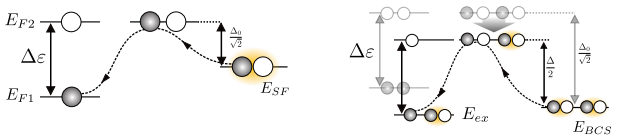

Figure 1.4: Pictorial sketch of the superfluid-to-normal phase transition, or vice versa: one of the two component fermion gains energy through a transition to the normal phase if $\Delta\varepsilon > \Delta_0/\sqrt{2}$, as stated by the CC limit (left). In the case $\Delta\varepsilon < \Delta_0/\sqrt{2}$ instead, partial breaking of Cooper pairs can still lead to the transition to a new energetically favored partially polarized superfluid (right).

Very generally, a transition from the normal (N) to the superfluid (S) phase is expected once $E_{SF} = E_N$ for the two related energies. If the normal phase is characterized by an energy mismatch between the two components Fermi levels, the pairing instability requires to overcome an additional energy cost ΔE to match the two and lead to superfluidity via the standard BCS mechanism (see the left panel in Fig. 1.4). Than the condition reads:

$$E_{SF} = E_N - \Delta E \tag{1.14}$$

This cost is eventually compensated by the negative pairs binding energy, $E_{SF} - E_N = -\Delta_0^2 n/2$, where Δ_0 stems for the superfluid energy gap and n for the density of states in the proximity of the (higher) Fermi energy. Relation 1.14 now reads

$$\frac{1}{2}\Delta_0^2 n = \Delta\varepsilon^2 n \tag{1.15}$$

where $\Delta\varepsilon$ is here an energy per particle. The superfluid phase is then allowed only for $\Delta\varepsilon < \Delta_0/\sqrt{2}$. This threshold is usually referred to as Chandrasekhar-Clogston (CC) limit [28], and it holds regardless of the nature of the energy cost ΔE in Eq. 1.14. In electronic systems, ΔE can be due to a paramagnetic instability which lowers the energy of the fully spin-polarized phase in presence of a magnetic field ($\Delta E \propto \chi H^2$, where χ is the magnetic susceptibility and H the field modulus) [28]. This is the case for high-Tc superconductors. Alternatively, ΔE can be associated with a

fixed population imbalance in generic two-component systems [29]: for equal mass mixtures with short range interactions the pairing instability competes with the s-repulsive interaction between dimers and unpaired fermions, see Ref. [30] and Ref. [2, 9] for the mass-imbalanced case. Alternatively, for systems with balanced populations a non-zero energy mismatch can arise from the different dispersion relations connected to a mass asymmetry.

In the following I will give a brief overview of the main microscopic theories predicting the existence of superfuid phases beyond the CC limit and the standard BCS paradigm. After that, I will discuss the possibility to experimentally address such peculiar superfluid phases in resonant two-component Fermi gases.

1.3.1 Two celebrated exotic superfluid phases

A theoretical approach attempting to describe the persistence of superfluidity beyond the CC limit relies on the idea that the imbalanced system undergoes a partial transition to the normal phase, breaking up only a limited number of pairs. Then, the ground state of the system quantitatively differs form the fully-paired BCS phase, with an energy lowered by the difference between the pair-breaking cost ($\Delta_0/2$) and the energy gained by the unpaired fermions ($\Delta\varepsilon$). This assumption is in contrast with the CC limit, that states that the fully unpaired phase is already favored for $\Delta\varepsilon = \Delta_0/\sqrt{2}$. Nonetheless, it can be shown [31] that the progressive breaking of pairs reduces the value of the effective superfluid gap Δ, until it is $\Delta/\sqrt{2} \leq \Delta\varepsilon < \Delta_0/2$, and a non-standard superfluid phase is still energetically favorable, with respect both to the normal and to the BCS phase (see left panel in Fig. 1.4).
The two most celebrated models predicting such *exotic* superfluid ground states are the FFLO theory (proposed by P. Fulde and R. A. Ferrell [31] and by A. Larkin and Y. Ovchinnikov [32]), and the Breached Pairing (BP) theory [33], strongly related to the so-called Sarma phase [34].

The FFLO approach predicts that the excess of majority fermions undergo an asymmetric occupation of the Fermi surface in the momentum space, yielding a non-zero normal current. In the lowest energy configuration, the normal current is balanced by a supefluid counter-flow, with the superfluid pairs having non-zero momentum. FFLO phases will then exhibit a spatially-varying order parameter. This is a plane wave in FF phases [31] a standing wave in LO phases [32]. In the latter case, due to the translation symmetry breaking, adjoining the superfluid character, the superfluid is re-

ferred to as supersolid.
Very generally, in FFLO phases the energy cost Eq. 1.15 is encoded in the kinetic energy associated with the non-zero momentum of the condensed pairs.

The Sarma theory predicts instead that pairing arises between fermions with opposite momenta, forming thus zero-momentum pairs as in standard BCS theory. Nonetheless, only one of the two fermions lays at its Fermi level E_{F1}, whereas the other occupies the energy $E_2 < E_{F2}$ corresponding to the selected momentum $|k_{F1}|$ (see Fig. 1.5(a)). Again here an energy cost is required for the superfluid phase to arise: fermions occupying energy levels in the vicinity of $E_2 < E_{F2}$ are promoted into the continuum. These excitations are explained in [35] by the incompatibility of BCS wavefunctions with a fully single-occupied phase-space region, since BCS theory postulates zero or double occupancy for the paired modes.
Very generally, the Sarma phase is experimentally identified by a spatially homogeneous partially-polarized superfluid phase.

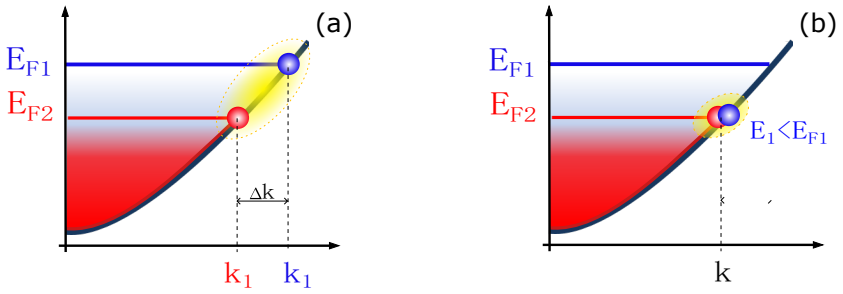

Figure 1.5: Pictorial sketch of the two pairing mechanisms of FFLO theory (a), and BP theory (b). The specific involved momenta and the mismatched Fermi energies are indicated in figure.

1.3.2 Addressing exotic superfluidy with Fermi gases: the role of mass asymmetry

Thanks to their exceptional degree of control, Feshbach resonant Fermi gases of ultracold atoms represent an appealing framework for the investigation of exotic superfluidity. In particular, the control of the population imbalance in double-species mixtures allows to directly tune the energy mismatch be-

tween the two associated Fermi energies, while Feshbach resonances enable to control the interspecies attraction, hence the pairing strength. Nonetheless, despite the recent advances in this experimental field, no unambiguous observation of exotic superfluidity has been reported so far. Previous experiments with homonuclear gases have observed a system instability towards phase separation, where an unpolarized superfluid core expels the excess of unpaired atoms within an outer shell of normal gas [36–40]. Among other kind of experimental platforms [41], only organic superconductors have shown so far indirect evidences of FFLO phases [42–44]).

In this section I discuss the possibility to experimentally address exotic superfluidity with heteronuclear mass-imbalanced Fermi mixtures. As already mentioned, mass asymmetry induces an energy mismatch between the Fermi surfaces of the two components. It thus naturally arises the question whether mass-imbalanced systems may be more promising to address exotic superfluidity, relative to their homonuclear counterparts. In this respect, various theoretical works agree on a positive answer [45–47]. To summarize the predicted advantages, I will mainly refer to the work of Ref. [46]. Here the authors consider the system Laundau thermodynamic potential, expressed as a power series of the superfluid order parameter and its spatial gradient. By investigating the relative coefficients as a function of temperature and population imbalance, they retrieve the order parameter features under each investigated condition. The resulting phase diagram at unitarity is reported in Fig. 1.6, for a homogeneous mass-balanced (Fig. 1.6(a)) and mass-imbalanced mixture (Fig. 1.6(a), for the case of a K-Li mixture). Remarkably, a spatially varying order parameter (signaling an FFLO phase) is predicted only in the mass-imbalanced case, for a majority of heavy fermions. The work in Ref. [47] additionally demonstrates that the critical temperature associated to the FFLO phase strongly increases with an increasing mass ratio.

The mass imbalanced diagram also signals a fostering of the Sarma phase or a majority of light fermions. Although this result is in agreement with present literature [45, 47], it is important to point out that the work [46] follows a mean field approach, which fails in distinguishing between uncondensed homogeneusly polarized gas of pairs (pseudogap phase), and strictly condensed BP or Sarma phases.

Finally, the forbidden regions (FR) correspond to non uniform superfluid order parameter densities: here the system phase separates [47].

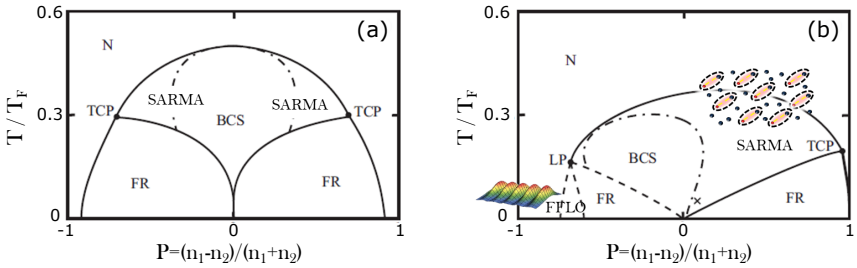

Figure 1.6: Predicted temperature-population imbalance phase diagram for the mass balanced (left hand plot) and mass imbalanced case of Li-K (right hand plot). The phase space regions hosting an FFLO or a Sarma superfluid are indicated, as well as those hosting a normal (N) and a standard superfluid (BCS) phase. Tricritical (TCP) and Lipshitzian (LP) points are also indicated. The Modified from [46].

As a conclusion to this section, the novel Cr-Li experimental platform presented in this work emerges as an extremely promising candidate for the investigation of exotic superfluid phases, combining the high degree of control on population imbalance and pairing interaction typical of ultracold gases, with a reasonably large mass ratio $M_{Cr}/m_{Li} \simeq 8.8$.

1.4 Itinerant ferromagnetim in 2-component Fermi systems

In this section I briefly focus on the physics of repulsive Fermi mixtures. Above a critical coupling strength, such systems are expected to manifest the paradigmatic phenomenon of spin demixing, leading to anti-ferromagnetic ordering in optical lattices [48–55] and ferromagnetic domain formation in continuum systems [56–59].
In this latter frame, the possibility of itinerant ferromagnetism -namely the phase separation of freely moving two-component fermions with fixed population imbalance- was first considered by E. Stoner [60] within a mean-field description for an electron gas subjected to a screened short-range Coulomb repulsion. The Stoner model is based on the competition between the repul-

sive interaction experienced by the system in the homogeneous case, and the kinetic energy cost inherent to phase separation. For the first (mean-field) contribution it is $E_{int} \propto a n_1 n_2$ being $n_i = N_i/V$ the single component density. For the kinetic energy of a single component Fermi gas it is instead $E_{kin} \propto n_i^{2/3}$, which increases by a factor $(V/V_i)^{2/3}$ when the Fermi gas gets shrunk into the final volume $V_i < V$. While the kinetic energy saturates around a finite value, E_{int} keeps increasing as $k_F a$ is cranked up until the critical value $k_F a = \pi/2$ is reached. Beyond this point, the paramagnetic, mixed phase becomes energetically favored against the development of non-zero magnetization. In the absence of spin-flip mechanisms, this turns into the emergence of partially polarized or fully polarized spin domains.
Although more accurate approaches, ranging from mean-field descriptions including next order interaction terms [61], low-energy theories [62], up to quantum Monte-Carlo calculations [63,64], predict a somewhat lower critical interaction strength, critical interactions of about $k_F a \sim 1$ are required for ferromagnetism to develop. As such, in contrast to BCS superfluidity, ferromagnetism is unavoidably a strong coupling phenomenon, therby challenging to treat theoretically. The nature itself of the transition to the ferromagnetic phase (I or II order) remains instead strongly debated [10].

In the following I will discuss the prospects for the experimental investigation of such ferromagnetic transition with ultracold Fermi mixtures with tunable interspecies interactions.

1.4.1 The pairing instability

As suggested in Sec. 1.2, Feshbach resonant Fermi gases populating the upper branch of the many-body spectrum appear as an ideal framework for the experimental investigation of itinerant ferromagnetism. [61]. Indeed, such systems uniquely features the two main ingredients of the Stoner model -Fermi pressure and strong short-range repulsion- free from intricate band structures, additional types of interaction or disorder, typical and somewhat unavoidable in condensed matter systems.

However, pioneering investigations [56,57] revealed that the quantum simulation of the Stoner Hamiltonian with ultracold fermions is complicated, if not fundamentally impeded, owing to the short-ranged nature of the interatomic interaction: the very strong repulsive strengths therein required can only be attained at large and positive scattering lengths, on the order of the interparticle spacing ($k_F a \sim 1$). As illustrated in Sec. 1.2, this inherently

implies the existence of a weakly bound state below the two-atoms scattering threshold. At the many-body level, this makes the repulsive Fermi gas a metastable state of the system: a three-body collision between the two repulsive fermions and a third atom can yield the formation of a dimer plus an extra particle with increasing momentum and kinetic energy, thereby depopulating the upper branch and heating the system. This process is referred to as three-body recombination. The rate γ_{3B} associated to three-body recombination processes features a strong dependency on the scattering length $|a|$ [2], monotonically increasing moving towards the unitary limit. In particular, for the case of a Fermi gas strongly confined within an ODT potential, it can be shown that [59]

$$\frac{\hbar\gamma_{3b}}{\varepsilon_F} \propto \frac{(k_F a)^6}{1+(k_F a)^2} \tag{1.16}$$

being ε_F the averaged Fermi energy over the gas density profile, within a local density approximation.

In spite of the intrinsic competition of the ferromagnetic instability with the pairing one, recent experiments [58, 59] possibly unveiled the ferromagnetic behavior of repulsive homonuclear Fermi mixtures. In particular, the recent work [58] demonstrated that a proper preparation of a Li-Li Fermi mixture in a domain-wall-like configuration -where the initial overlap of the two polarized gases is zeroed- enables to attain a semi-stationary ferromagnetic configuration, stable on the $10\,ms$ timescale, for large enough $k_F a$ values. The same mixture has enabled via a pump-probe spectroscopy protocol to unveil the development of micro-domains of spin-polarized fermions following a rapid quench of the repulsion strength within the two-component gas [59]. At long evolution times after the interaction strength, such domains appear to coexist with dimers formed through inelastic pairing processes in a semi-stationary emulsion state. Although subsisting as an interesting phenomenon in itself, the observation of such complex dynamics clearly undermines the prospects for a clean study of Stoner ferromagnetism in such homonuclear experimental systems. Indeed, the transition from a paramagnetic to a ferromagnetic phase with spatially separated domains remains at the present time unobserved.

1.4.2 Addressing itinerant ferromagnetism with Fermi gases: the role of mass asymmetry

In analogy to the discussion presented in Sec. 1.3.2 in the contest of exotic superfluidity, in this section I consider how mass asymmetry may positively affect the experimental addressability of Stoner ferromagnetims within ultracold itinerant Fermi mixtures.
To this end, I refer to the theoretical work in Ref. [65]: within the same mean field approach discussed above for the Stoner criterion in the mass-balanced case, the authors of Ref. [65] evaluate the energy of the ferromagnetic and the paramagnetic states as a function of the mass ratio. Applying a Stoner criterion generalized to $m_\uparrow \neq m_{downarrow}$ they could obtain, as a function of the mass ratio, the critical phase boundaries separating the different regimes. The main results for a 3D mixture are summarized in Fig. 1.7. The labels indicate the allowed equilibrium phases: (L&H) stems for the fully ferromagnetic phase with spatially separated light (L) and heavy (H) particles; (L,H) stems for the paramagnetic phase, where the two component homogeneously coexist; (L',H')&(L",H") indicates instead the partially polarized phase, with the coexistence of two homogeneous separated domains where the light and heavy fermions have different densities. The dot-dashed line indicates the Li-K case. Interestingly, the ferromagnetic phase results always to be energetically favored in the limit of diverging mass asymmetry (low plot region, $m_L/m_H \to 0$) although in presence of vanishing repulsion (right side, $1/k_F a \to \infty$).
The authors account for repulsive interactions via a mean-flied contact term, an approximation which is in principle valid only in the weakly interacting limit. Nonetheless, the authors point out that the energy gain in favor to the ferromagnetic phase is cranked up by the interaction strength: if the gas undergoes phase separation for a certain value of m_L/m_H and $k_F a_S$, it will certainly continue to phase separate at larger values of $k_F a$. As a consequence, the monotonic decrease of the Stoner critical interaction as a function of m_L/m_H emerges as a sound theoretical result, irrespective of the modeling employed to describe the repulsive interactions. A decrease of the critical Stoner interaction inherently implies the possibility to experimentally address itinerant ferromagnetism within more stable repulsive Fermi systems, where inelastic decay processes are sizeably reduced, see again relation Eq. (1.16) [59]. As a conclusion, the Cr-Li mass-imbalanced mixture arise as an exiting framework also in this respect. As already anticipated, such mixture

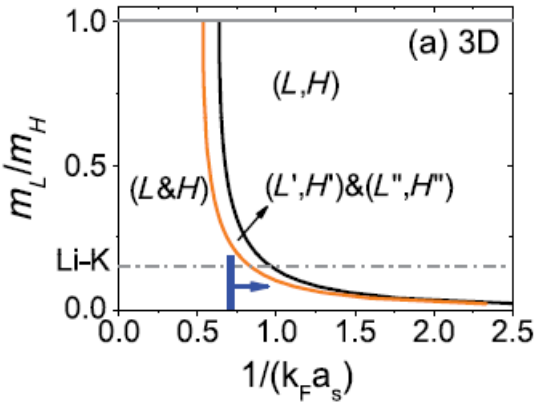

Figure 1.7: Phase diagram for the repulsive double-species Fermi gas in terms of mass ratio (m_L/m_H) and interaction strength ($1/k_F a$). The paramagnetic (L,H), partially polarized (L',H')&(L",H") and fully polarized (L&H) phases are separated by the related boundary conditions (solid lines). Beyond the marked interaction threshold it is $E_{int} < E_{kin}/2$, being E_{int} and E_{kin} the homogeneous phase interaction and kinetic energy respectively. Taken from [65].

offers additional peculiar features, able to further suppress the pairing instability within the upper branch. This features will be extensively discussed within the next section.

1.5 The atom-dimer interaction: few and many body features

Fermions represent the fundamental building blocks of ordinary matter, whereas bosons only exist as composite particles. A dimer formed by the combination of two fermions consists in the simplest system to study the physical nature of composite bosons, whereas the fundamental role of fermionic quantum statistics clearly emerges as soon as we move to the study of its interaction with a third fermionic particle.
I n the following I discuss the generic features of a three-body state consisting of two identical fermions plus a third particle, with a generic mass ratio among the two components. From such a discussion it will become evident how Cr-Li mixtures may enable uniquely the observation of very peculiar few-body regimes, unattained so far. Furthermore, I will discuss how such mixture may provide an appealing many-body framework with non-

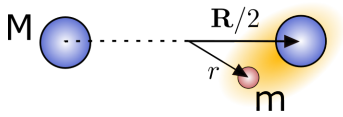

Figure 1.8: A light atom of mass m attractively interacts with two heavy atoms of mass M, having relative distance R.

perturbative few-body correlations.

1.5.1 The atom-dimer problem within a Born-Oppeneimer description

I approach here the atom-dimer scattering problem for a two-component Fermi system. I will show how the composite nature of the dimer has deep consequences on the scattering properties, and discuss the strong mass ratio dependency of the related three-body potential. To this end, it is instructive to first look at the strongly imbalanced case of two identical fermions of mass M attractively interacting with a third fermion of mass $m \ll M$, as depicted in Fig. 1.8. Such system is well described by the Born-Oppenheimer approximation, with a total three-body wavefunction factorized as follows:

$$\Psi(\mathbf{r}, \mathbf{R}) = \phi_{\mathbf{R}}(\mathbf{r})^{\pm}\psi(\mathbf{R})^{\mp} \tag{1.17}$$

$\phi_{\mathbf{R}}(\mathbf{r})^{\pm}$ describes the motion of the light particle, adiabatically adjusting itself at the distance $\mathbf{R}$ between the two (slowly moving) heavy fermions. For convenience, let us consider the $a > 0$ case, where a stable dimer $m - M$ exists in the vacuum. In the presence of the third particle, the light fermion wavefunction can be written as a symmetric $(+)$ or anti-symmetric $(-)$ superposition of the dimer wavefunction localized around the "left" and "right" heavy fermion, and takes the form [9]

$$\phi_{\mathbf{R}}(\mathbf{r})^{\pm} \propto \frac{e^{-k_{\pm}|\mathbf{r}-\mathbf{R}/2|}}{|\mathbf{r}-\mathbf{R}/2|} \pm \frac{e^{-k_{\pm}|\mathbf{r}+\mathbf{R}/2|}}{|\mathbf{r}+\mathbf{R}/2|} \tag{1.18}$$

Assuming a heavy-light contact potential, the wavevector $k_{\pm}$ must fulfill the Bethe-Peierls condition (1.4) at $\mathbf{r} = \pm\mathbf{R}/2$, and satisfy the free-particle Shrödinger equation otherwise. It can be easily verified that $k_{\pm}$ must obey the relation

$$k_{\pm} \pm \frac{e^{-k_{\pm}R}}{R} \tag{1.19}$$

yielding the eigenenergy $E^{\pm}(R) = -\hbar k_{\pm}(R)/2m$. This, then, represents an effective interaction potential $U_{\pm}(R) = E_{\pm}(R) - |\epsilon_b|$ for the Shrödinger equation of the heavy particles, described by the wavefuntion $\psi(\mathbf{R})^{\mp}$. The additional term $-\epsilon_b(a, R^*)$ removes here the constant offset associated to the bare in-vacuum dimer energy; this quantity solely depends on the 2-body scattering parameters a and R^*, as set by relation (1.5) for a reduced mass $\mu \to m$ (which is exact in the limit $m/M \to 0$). It can be shown that such potential is purely attractive ($U^+ < 0$) for the symmetric configuration $\phi_{\mathbf{R}}(\mathbf{r})^+$, and purely repulsive ($U^- > 0$) otherwise [66,67]. Within an intuitive picture, the symmetric configuration corresponds to the light atom having maximal probability distribution in between the two heavy fermions, mediating their reciprocal attraction. In particular, it can be shown that $U_{\pm}(R)$ is long ranged, falling off as a Yukawa-like potential as $R \gg a$, whereas it behaves as $\sim 1/(mR^2)$ at intermediate distances $R \leq a$ [9,67].
In the absence of any heavy-heavy atoms interaction, the (radial) wavefunction $\psi(\mathbf{R})^{\mp}$ experiences the total potential

$$V_\ell(R) = U^{\pm}(R) + \frac{\hbar^2 \ell(\ell+1)}{2MR^2} \tag{1.20}$$

with an effective centrifugal barrier set by the angular momentum ℓ.

The role of quantum statistics and the composite nature of the dimer clearly emerge within the anti-symmetrization of the total wavefunction (1.17), directly leading to the ℓ-dependence of the atom-dimer scattering properties: in particular, only anti-symmetric heavy-atom wavefunctions $\psi(\mathbf{R})^-$ (odd ℓ) can orbit within the attractive energy surface U^+, and vice-versa, whereas all even partial wave channels experience a net repulsion, primarily in the s-wave. As a result, the atom-dimer scattering length is always positive, irrespective of the mass ratio.
In the low energy limit, the attractive atom-dimer problem then restricts to p-wave ($\ell = 1$) scattering channel. The associated potential $V_1(R)$ results as the competition between the repulsive centrifugal barrier $\propto 1/M$ and the attractive mediated interaction $U^+ \propto 1/mR^2$. Fig. 1.9 reports examples of $V_1(R)$ for different M/m values, in the broad resonance limit $R^* = 0$. Remarkably, for small M/m values (dashed curve) the centrifugal barrier dominates at any R, inducing a fully repulsive potential. The result is reversed at large M/m values (dotted curve), exceeding the critical value 13.6, where the potential is fully attractive. This potential, which scales as $\sim 1/R^r$, is responsible for the appearance of the Efimov effect. This is associated with

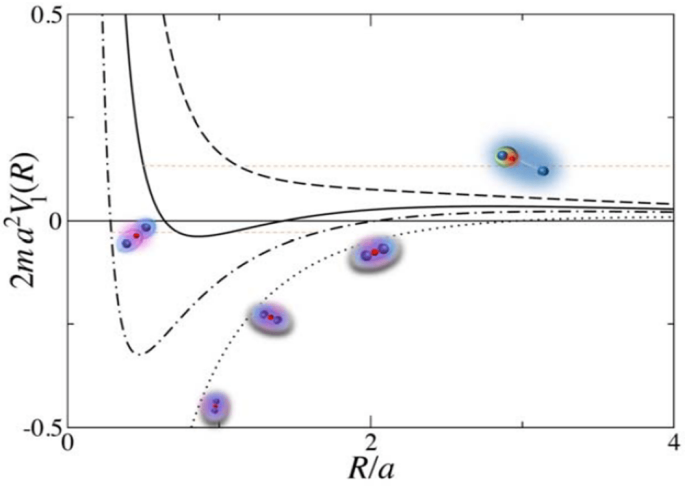

Figure 1.9: Born-Oppenheimer atom-dimer effective potential V1(R)=U+(R)+Ucb(R) in the l=1 channel and wide resonance limit $R^* = 0$ for mass ratios $M/m = 13.6$ (dotted line), 8.2 (dash-dotted), K/Li (solid) and 5 (dashed). A cartoon exemplifies the expected atom-dimer system in each case. Image adapted from [67].

the existence of trimers states featuring a log-periodic energy spectrum and discrete scaling symmetry [68–70]. In the limit $a \to \infty$ the Efimov trimers compose an infinite set with logarithmic energy-spacing low. Within a more complete treatment beyond the zero-range approximation, it can be shown that Efimov trimers persist as bound states also for $a < 0$ [9], where the two body state is absent. For this reason, in the $a < 0$ regime Efimov trimers have Borromean character.

For intermediate values of M/m instead ($8.17 < M/m < 13.6$), the potential develops a well at $R \sim a$, and the centrifugal barrier only dominates at shorter distances. As I will discuss within the next subsection, a more complete theoretical approach demonstrates the possibility for such potential well to sustain up to two trimer stable states. The main features of such trimers, as well as their experimental investigation, are also discussed in the following.

1.5.2 The peculiar case of Cr-Li: the Kartavsev-Malykh trimers

The *exact* derivation of the p-wave channel potential for any M/m value was first derived by O. I. Kartavstev and A. V. Malykh [1], for an interspecies (heavy-light) contact potential with $R^* = 0$ and zero intraspecies (heavy-heavy) interaction. Quite remarkably, the calculation quantitatively validates the key results of the Born-Oppenheimer approximation (see also Fig. 1 in Ref. [2]). In particular, the authors demonstrate that the potential sustain one and two bound states for $\lambda_1 \simeq 8.17 < M/m < \lambda_2 \simeq 12.9$ and $\lambda_2 < M/m < 13.6$, respectively. This states, referred to as Kartavstev-Malykh (KM) trimers, significantly differ from the Efimov ones: they exist only at positive interspecies scattering lengths, and very importantly, they are collisionally stable thanks to the presence of the centrifugal barrier, which impedes particles to approach each other at short distances.

To my knowledge, no double-species experimental platform currently available within the ultracold atoms community fulfill the required mass ratio for the KM trimers to arise, and the existence of such few-body features remains unobserved so far. The novel Cr-Li mixture object of my thesis, exhibiting a mass ratio $M_{Cr}/m_{Li} \simeq 8.8$, emerges to this end as an exceptional candidate. Furthermore and very importantly, the strong dependence of the atom-dimer scattering properties upon finite range effects encoded into a non-zero R^* - via the term $U^+ \propto k_+(a, R^*)^2$ in equation (1.20) - experimentally allows for a resonant tuning of the three-body interaction on top of the standard 2-body ones. As shown in Ref. [67] for the K-Li case, the three-body attractive potential is progressively and strongly weakened by an increasing R^*, with the ratio R^*/a plying qualitatively the same role of a decreased mass ratio. In particular, the Cr-Cr-Li trimer is predicted to lie extremely close the atom-dimer threshold already for $R^*/a = 0$ thereby being extremely sensitive to any finite-range effect. Fig. 1.10 shows how the KM trimer state already hits the atom-dimer threshold at $R^*/a \sim 0.03$. For larger values, the trimer converts into a virtual state lying above the atom-dimer threshold, leading to the occurrence of a p-wave scattering resonance between Cr and Cr-Li dimers [71].
Since R^* is fixed by the character of the specific Feshbach resonance, and a can be tuned via the Feshbach field, the Cr-Li system uniquely enable to control three-body resonant interactions, on top of the two-body ones. In particular, the purely elastic character of such effect makes it an unprece-

dented new experimental tool both within the few- and many-body context.

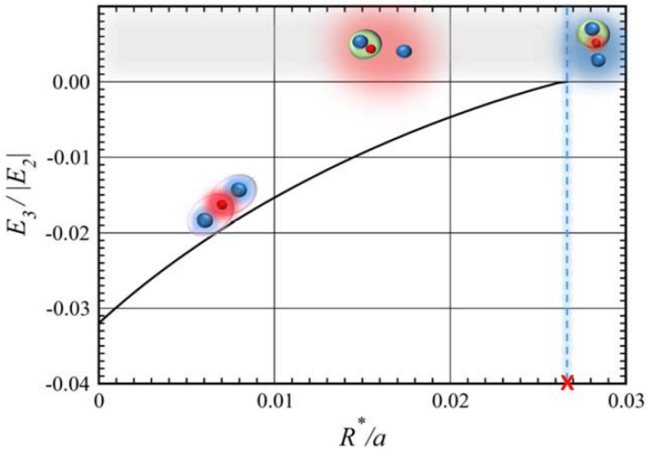

Figure 1.10: Cr-Cr-Li binding energy detuning from the atom-dimer Cr-CrLi energy threshold (E_3), normalized to the dimer energy E_2, as a function of R^*/a. In the $R^* \to 0$ limit and up to $(R*/a)_c \sim 0.03$ (marked by the red cross), the trimer is stable. Figure from D. Petrov (private communication).

1.5.3 Impact of the Cr-Li three-body features on ferromagnetic phases

In this subsection I briefly discuss another key three-body feature of the Cr-Li mixture, intimately connected with the existence of the KM state discussed above. This second property expected for the system subject of my thesis deals with Cr-Li mixtures in the repulsive branch of the Feshbach resonance. In Ref. [2] the author investigates the low energy limit of the atom-dimer scattering problem with $M/m < 13.6$. In this non-Efimovian regime, the presence of a centrifugal barrier at short interatomic distances makes short-range parameters unessential for a quantitative description of the three-particle interaction, with the scattering problem being fully determined by the interspecies scattering length a, and the mass ratio. Under such conditions, the author analytically derives the open channel wavefunction describing the atom-dimer product of a three-body recombination event. Such a three-body inelastic process, as discussed in subsection 1.4.1, strongly destabilizes the repulsive Fermi liquid within the upper branch of the many-body spectrum.

By comparing this result with the free-atom wavefunction for the three approaching fermions, the author obtains the three-body recombination rate shown in Fig. 1.11 as a function of the mass ratio.

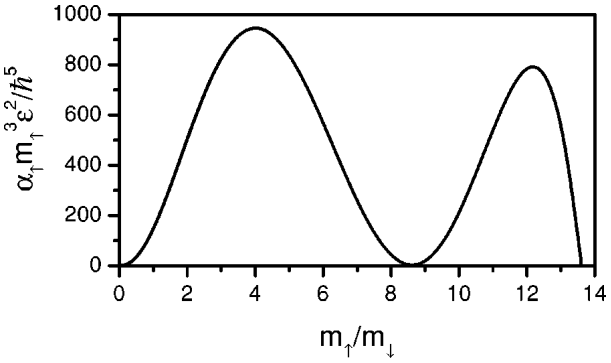

Figure 1.11: $\alpha_\uparrow m_\uparrow^3 \varepsilon^2/\hbar^5$ is an dimensionless quatity proportional to the recombination rate $\alpha_\uparrow$ associated to the process $\uparrow + \uparrow + \downarrow \rightarrow \uparrow + \uparrow\downarrow$. ε is here the dimer ($\uparrow\downarrow$) binding energy. This quantity is plotted as a function of the mass ratio, within the non-Efimovian regime. As shown, the decay rate features a minimum point $\alpha_\uparrow = 0$ for $m_\uparrow/m_\downarrow \simeq 8.62$. Figure taken from [2].

Very remarkably, the recombination rate for $\uparrow + \uparrow + \downarrow$ processes is perfectly zeroed at two specific mass ratios: $m_\uparrow/m_\downarrow \simeq 8.62$, significantly close to the threshold $\lambda_1 \simeq 8.17$ for the emergence of a stable KM trimer. The authors of Ref. [1] interpret this feature as arising from a quantum destructive interference phenomenon connected with the presence of the KM trimers underlying the atom-dimer threshold. Such a peculiar quantum interference mechanism resembles the one experimentally observed in the context of Efimov physics: the existence of Efimov trimers below both the three atoms and atom-dimer scattering thresholds yields the resonant suppression of three-body losses [9,18,72–76]. In these cases, though, such a suppression does not yield a perfect zeroing of three-body recombination, since the Efimov states wavefunctions always feature a non-negligible weight at short distances, in contrast with the KM trimer case.

1.5.4 Further effects of atom-dimer interaction within Cr-Li few- and many-body systems

I conclude this section by pointing out additional appealing extensions of the atom-dimer interaction enabled in Cr-Li systems within a many-body

context, although such possibility has not been considered at the theoretical level so far.

In the first place, the presence of a strong atom-dimer attraction on top of the standard 2-body one could represent an interesting tool for the investigation of exotic superfluid phases within the attractive branch of the many-body spectrum. For large but finite $a > 0$ values, the KM trimers are expected to convert into virtual states lying above the atom-dimer threshold due to finite range effects ($R^*/a > 0$), leading to the resonant enhancement of the p-wave atom-dimer interaction [67]. It is reasonable to expect that such large Cr-dimer attraction may favor the creation of polarized superfluids even at strong coupling [77], while the p-wave character of such attractive interaction could foster pair condensation into non-zero momentum states, hence the development of FFLO regimes.
Moreover, the strong p-wave Cr-CrLi attraction and the proximity of a tetramer state [78] could facilitate p-wave paring of polarized Cr atoms, mediated by the exchange of a CrLi dimer.
Within the resonance limit instead ($R^*/a \sim 0$), the KM trimers will be well defined below the atom-dimer threshold, and at low temperature they could form a degenerate Fermi gas. Here, their p-wave character, together with the magnetic nature of Cr atoms, might also allow for further appealing extensions: since the Cr-Cr-Li trimer is a p-wave bound state, it has three possible degenerate configurations ($m_\ell = \pm 1, 0$), and therefore, a non-polarized cloud of such trimers will generally be an interacting system. However, because of the tiny distance of the trimer state from the atom-dimer threshold, the weak, though appreciable magnetic dipole-dipole interaction between the Cr atoms can sensitively affect the stability and the energy of such states. More precisely, dipolar interaction will generally tend to stabilize the $m_\ell = 0$ component, and destabilize the $|m_\ell| = 1$ ones. Another interesting mechanism to selectively polarize the three-body states could be the exploration of strongly anisotropic trapping potential: confining the trimers in a 1D tubes (2D pancakes) parallel (orthogonal) to the magnetic field orienting the dipoles could favour the $m_\ell = 0$ ($|m_\ell| = 1$) Fermi gas component.

Chapter 2

Vacuum apparatus: design & realization

In this chapter I present in detail the experimental vacuum apparatus that I designed and implemented for the realization of ultracold samples of Li and Cr mixtures.
The chapter is divided in three main sections: Sec. 2.1 provides an overview of the apparatus design and describes its main components; Sec. 2.2 presents the main coils assemblies implemented onto the apparatus in terms of their structure and magnetic field profiles; finally, Sec. 2.3 reports on the assembly and backing procedure followed to implement the final structure, and to reach ultra high vacuum conditions in the apparatus.

2.1 Vacuum structure

Our apparatus design is based on a general key strategy: the two species are effused along two independent vacuum lines that recombine within the main experimental chamber. This choice is mainly due to the strongly different sublimation temperatures needed for Li and Cr atoms, of $\sim 450°$ and $\sim 1500°$, respectively.

In order to design the vacuum setup I made use of well-established models in vacuum technology for molecular flow ([79–82]), to associate a flow conductance to the various setup components and optimize their shape, as well as to determine the suitable pumping speeds that must be applied to the apparatus. The vacuum quality within the setup is indeed of fundamental

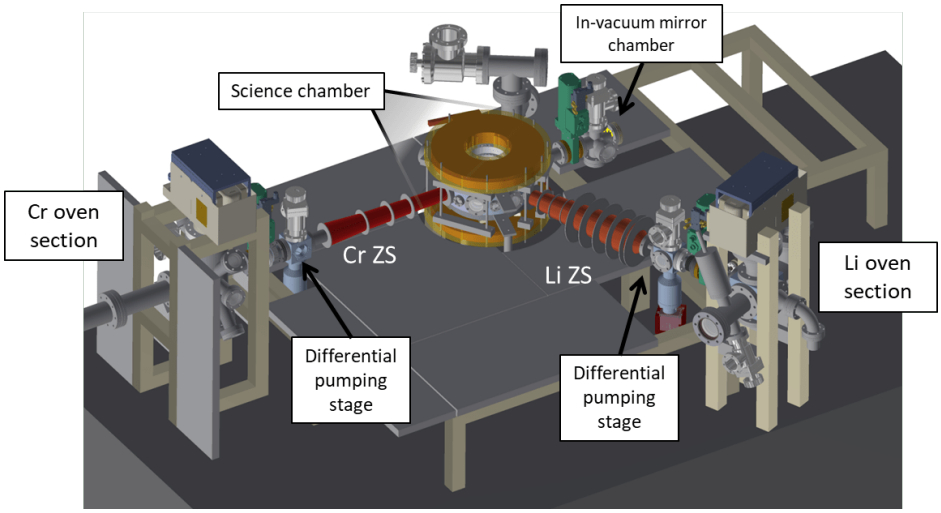

(a)

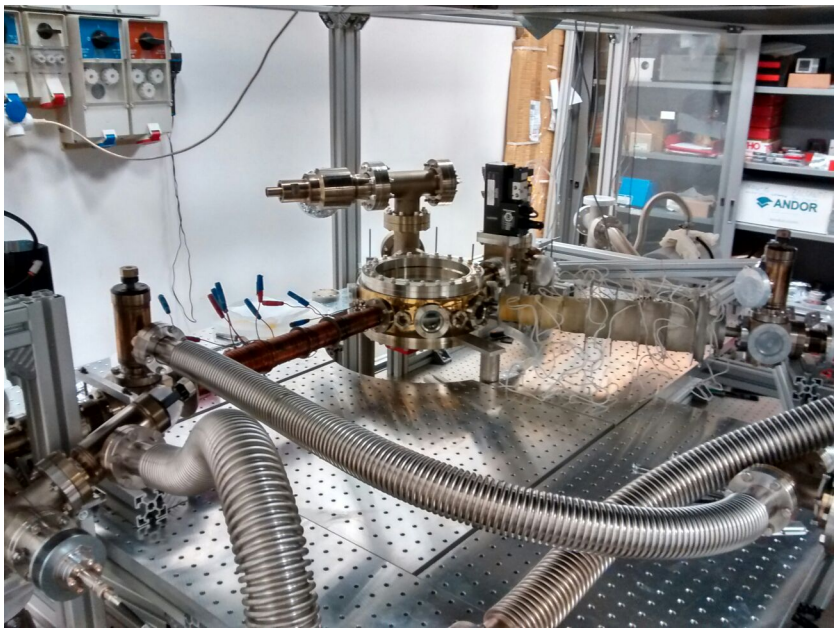

(b)

Figure 2.1: Overview of the vacuum apparatus plus sustaining frame system of breadboards and aluminum profiles. (a): CAD sketch. (b): photo of the assembled vacuum apparatus; the flexible tubes which connect the vacuum apparatus to the pre-pumping system are also visible (see Sec. 2.3).

importance to guarantee a high collection efficiency of the atoms and a long lifetime of the degenerate mixture: background atoms can collide with the cold and ultracold Cr and Li samples, reducing the slowing process efficiency and heating up the Cr-Li gas, causing atoms to escape from the trapping volume.
A schematic overview of the apparatus is shown in the computer-aided design (CAD) of Fig. 2.1(a), and in photo 2.1(b), taken at the very last step of the assembly stage of the apparatus.
The detailed design of each of the main components of the vacuum setup is presented in the following.

2.1.1 Oven chambers

The design and the operation temperature of a sublimation reservoir are set by the optimal atomic flux, which, within the effusive regime[1], is characterized by the following longitudinal velocity distribution [4]:

$$f_{v_L}(v_L, T) = \left(\frac{\pi\phi}{2}\right)^2 \frac{P_{sat}(T)}{k_B T}\left(\frac{m}{2\pi k_B T}\right)^{3/2} v_L^3 \exp\left(-\frac{m v_L^2}{2k_B T}\right) sin^2(\theta) \quad (2.1)$$

for the atoms emitted within the small solid angle defined by the azimuth angle θ. Here ϕ is the emission hole diameter, and T the temperature. k_B is the Botzmann constant, m the mass of the atomic species and P_{sat} the vapor pressure of the sample.
The behavior of P_{sat} as a function of T for the specific case of Cr and Li solid samples can be found in Ref. [4] and [83]; the resulting suitable values of the reservoir temperatures are $\sim$1500° and $\sim$420°, respectively. Typical values for ϕ are of he order of $1\,mm$. Fig. 2.2(a) and (b) show the probability distribution relative to our Cr and Li reservoir respectively.

Owing to the extremely high temperatures required for Cr sublimation, the Cr oven chamber is an industrial HT-cell[2]. The chamber is composed by a core crucible in ZrO_2/CaO, inserted into a second crucible of tungsten; the two crucibles are heated up by a tungsten filament, and water cooled within a stainless steel (SS) CF40 chamber. We decided to employ this specific combination of materials for the realization of the core crucible due to

[1] This regime is satisfied when the diameter of the emission hole is much smaller than the mean free path of the particle within the effusion reservoir.

[2] CreaTec, model: HTC-40-10-284-SHM

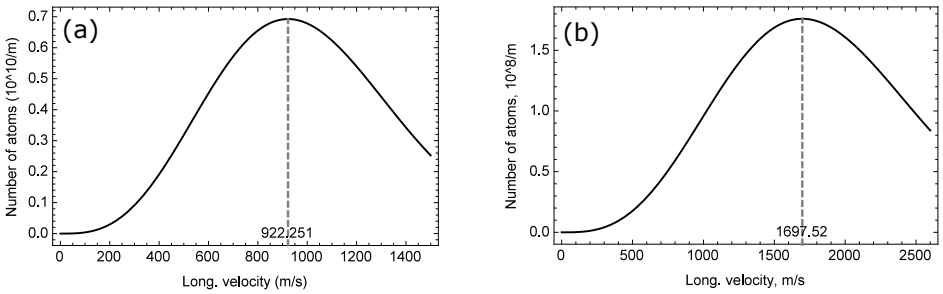

Figure 2.2: Atomic flux per longitudinal velocity class for Cr (a) and Li (b) atoms, calculated for the experimental values of T (1500°C and 420°C) and ϕ ($3\,mm$ and $2\,mm$ respectively). The considered solid angle subtends respectively a magneto-optical trap section of $5\,mm$ and $3\,mm$ radius from the distance set by the oven position. A vertical dashed line marks the velocity corresponding to the maximum flux.

the chemical reactivity of Cr with other compounds, as previously reported by the Paris group [4]. Furthermore, based on test performed by the same group, the combination of ZrO_2 with Cao results in a better temperature stability, relative to the one featured by the natural zirconium dioxide. The ZrO_2/CaO crucible is closed by a cap with a $1\,mm$ diameter hole.
The Cr solid sample, featuring natural abundance, was delivered by the producers within plastic containers in air. After filling the ZrO_2/CaO crucible with the Cr sample, the cap was glued in place with a high-temperature glue[3].
The Cr oven chamber is provided with a thermocouple temperature sensor and readout contacts, and with a SS shutter controlled by a pneumatic actuator. The oven chamber is host into a CF63 edge-welded bellow. This allows to finely align the atomic flux towards the experimental cell by adjusting the length of four threaded rods fixed at the two bellow flanges, see Fig. 2.3(a). The Cr effusion cell is connected to a CF100 vertical chamber with six lateral CF40 arms, three for each side, oriented at 45° one with respect to the other, see CAD in Fig. 2.1(a). The four arms placed at 90° terminate with anti-reflection coated windows enabling to implement a transverse cooling stage. The additional two arms simply provide a direct optical access to the oven output from one side and the connection to a gauge for pressure monitoring and to the prevacuum pumping system from the other. Two vertical breadboards (also sketched in CAD) provide a working surface for the assembly of

[3]Resnond, 904 Ultra Temp Zirconia, delivered by Cotronic Corporation.

the transverse cooling optical setup. The sizes of the CF100 cross and the oven CF63 bellow are such that the effusion cell extremity protrudes into the CF100 cross body for a few centimeters, thus being visible from the lateral optical accesses: this greatly facilitates the alignment of the Zeeman slower laser light which is shined onto the oven nozzle to slow down the effused atoms.

The Li reservoir requiring significantly lower operation temperatures is composed by a CF40 flanged cup plus a nozzle, is based on a custom design, see Fig. 2.3(b). A standard fixed band heater[4] heats up the cup base up to the desired temperature. The nozzle has been realized by drilling a $1\,cm$ diameter hole at the center of a blank CF40 flange, on top of which it is screwed a thin plate with a tapered hole of smaller dimensions. The adjustment of the tapered hole position with respect to the flange center allows to adjust, if needed, the orientation of the outgoing atomic beam. The design of the Li oven nozzle is inspired by the one developed in the MIT experiment described in Ref. [84], also employed in the LENS experiment, see Ref. [82].
To avoid undesired chemical reactions, we employed Nickel gaskets at the interfaces within the oven section.
The Li reservoir is vertically oriented and connected to a CF63 cube through a 90° elbow. One lateral side of the cube hosts a viewport, allowing to monitor the Li slowing laser light alignment. At the opposite aperture, a CF63 tee hosts a Ti-sublimation pump[5].
Frontally with respect to the oven, a reducing cone connects the CF63 cube to a CF40 in-line mechanical shutter[6] provided with pneumatic actuator.
Our Li atomic source is composed of an enriched (95%) sample of ^{6}Li. The sample was delivered by the producer in glass vials under Ar atmosphere in order to prevent oxidation. The sample was inserted into the reservoir before the final bake-out procedure operated on the assembled vacuum apparatus, see Sec. 2.3. In order to inhibit oxidation processes, the oven chamber was flooded with a constant flux of Ar. Under Ar atmosphere, we could thank brake the protecting glass vial and fill the oven reservoir.

[4]Watlow, model *Miniband*.
[5]Varian, Mini-Ti Ball source.
[6]Kurt Lesker, model DS275VPS-P

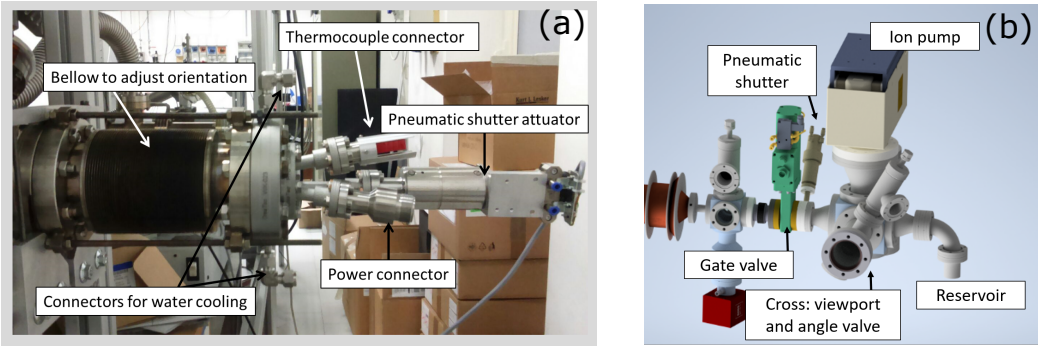

Figure 2.3: (a): Cr effusion cell; the cell flange is attached to an edge-welded bellow which is aligned and fixed by four longitudinal rods, screwed at the two bellow flanges. (b): Li custom oven structure. The heatable cup is vertically oriented and hold by a 90° elbow pipe. The nozzle is fixed at the opposite side of the elbow, in vertical position.

An ion pump[7] is connected to both Cr and Li oven chambers from the top, see again Fig. 2.3(b). Here the worst vacuum is expected, and NEG (Non-Evaporative Gettering) elements would get immediately coated to saturation. The additional titanium-sublimation pump at the Li oven chamber helps to maintain a good vacuum pressure by means of gettering chemical activity. This latter device is not necessary at the Cr oven, thanks to the good gettering properties of Cr itself.
Finally, an all-metal gate valve[8] is separates both Cr and Li oven sections from the rest of the vacuum apparatus, enabling to quickly isolate the experimental chamber in case of an oven malfunctioning or during substitution of exhausted atomic sources

2.1.2 Zeeman slowers and differential pumping stages

The thermal atoms emitted from the ovens are slowed down by two dedicated Zeeman slowers (ZS) coils systems plus a counter-propagating laser beam, by exploiting a spatially-varying Zeeman effect. A ZS is composed by two concentric tubes, around which a series of coils is externally winded up with appropriate number of loops/layers to reproduce the desired field profile. While the designing features of the Li and Cr ZS coils are detailed in Sec. 2.2, in this section I present their vacuum holding structure.

[7] Agilent Technologies, model Vaclon plus 75 star cell.
[8] MDC, model E-GV-1500M-P-11, kalrez seal option.

The Cr ZS structure is composed by two concentric CF16 and CF40 SS tubes of total length $L = 47.7\,cm$, comprehensive of extremal CF40 flanges. The gap between the two tubes is exploited for water cooling: two walls run along the axial direction and divide the gap in two symmetric chambers, linked only at one extreme of the ZS tube to let the water flow from one into the other; at the opposite extreme, a water connector for each chamber allows the water to flow in and out, respectively. This system ensures a uniform cooling of the ZS structure.

The Li ZS is also composed by two concentric CF16 and CF40 SS tubes, but here the inner CF16 tube protrudes at the extremities of the ZS and it allows for a CF16 flanged connection on both sides. Two transverse $12\,mm$ thick SS disks seal the gap between the two tubes at the CF40 tube extremities. Again in this case two inner walls run along the axial direction driving the water flow. Two threaded holes, drilled along the radius of one of the disks, enable the fastening of input and output water connectors. The inner surface of the disk is also drilled to let the water flow inward and outward the inner gap. The total length of the object is $L = 48.73\,cm$. A detailed view of the structure is provided in Appendix A.

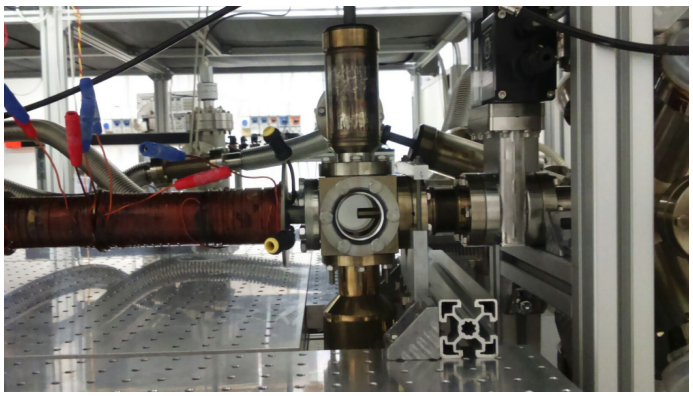

Figure 2.4: Cr differential pumping stage: the small tube is visible from inside the CF40 cube. A small pump is connected to the cube from below. On top, an all-metal angle valve allows the pre-pumping operation. The Cr ZS is visible on the left side, on the right side the bellow connects the stage to the gate valve.

Both ZS are separated from the oven chambers by a very compact differential pumping stage, based on a custom design with similar features for both species and shown in Fig. 2.4. The stage reduces the flow conductance between the oven and the following section and enables to attain a regime of

ultra-high vacuum within the experimental cell. It is composed by a narrow tube of $8\,cm$ and $10\,cm$ length, for the Li and Cr stage, respectively, fastened in axial alignment at the center of a pierced blank CF40 flange, which is connected to a CF40 cube. The tube protrudes inwards and outwards the cube wall; on the outward side, a CF40 bellow protects the tube and allows the connection to the gate valve. The opposite side of the cube directly connects the ZS.
At the bottom of the cube a Saes Getter NexTorr pump[9] enhances the differential stage efficiency. This pump is characterized by a very small body volume, composed by a NEG element plus a small ion-pump body. The NEG element slightly protrudes into the CF40 cube volume and greatly increases the pumping speed, despite the limited ion-pump body[10].
An all-metal angle valve is connected from the top to allow for pre-pumping access. Uncoated windows are installed at the lateral cube sides: again here the lateral view has been very useful to optimize the ZS beam alignment.

2.1.3 Experimental cell and in-vacuum mirror chamber

Our experimental cell is a custom Kimball Physics spherical octagon chamber, with 8 perimeter CF40 windows, spaced out by CF16 windows. Due to the many in-plane optical accesses, our experimental cell has a very large radius of $\sim 13\,cm$.

The in-plane arrangement of the optical accesses dedicated to the magneto-optical trap (MOT) beams, the optical dipole trap (ODT) beams and the imaging beam is described in Ch. 3. For an overview of the relative optical setup I refer to Fig. 3.17.
Within the vertical direction instead, a very wide optical access to the experimental cell is left free for a high resolution imaging setup, not implemented yet. The access is provided by two CF200 windows[11] with a $\sim 11\,cm$ diameter glass[12]. The two viewports have a re-entrant shape that places the glass as close as possible to the atomic cloud, as shown in Fig. 2.5. As I will explain

[9] Model D 100, 100 L/s.
[10] The small ion-pumping element is anyway necessary to eliminate noble gases.
[11] UKAEA, custom design.
[12] Custom anti-reflective coating for all the exploited wavelengths by Laseroptik.

in Sec. 2.2.3, I exploited the space available within the re-entrant viewports to place a very compact set of coils. These coils, designed to produce a very flat magnetic field profile, will provide the homogeneous Feshbach field with which to tune the inter- and intra- two body scattering properties of the atomic cloud within the experimental routine.

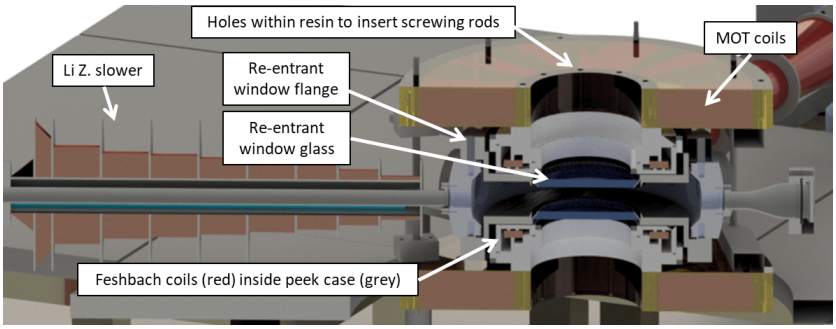

Figure 2.5: CAD section of experimental cell, re-entrant windows, Feshbach coil cases and MOT coils system. The Feshbach coil cases are inserted into the re-entrant windows.

A vertically oriented CF63 4-way cross is connected at one of the viewports dedicated to the MOT beams. This chamber is exploited for the pumping and pre-pumping system. The bottom flange of the cross is connected to a pump, while a CF63 tee is fastened to the top flange and holds an all-metal angle valve from one side, and a pressure measuring gauge[13] from the other. The pump is also in this case a NexTorr[14], and the NEG element protrudes some millimeters within the volume interested by the CF63 axial optical access to guarantee the best working efficiency.

Two opposite CF16 accesses of the main chamber are exploited to connect the Li ZS tube from one side and to enable the transmission of the Li ZS beam from the other. Here a reduction cone connects a CF40 window to the CF16 aperture[15], see again Fig. 2.5.
The window is made of sapphire[16], which is known to hinder metallic surface

[13]Varian, UHV-24P hot-cathode gauge.
[14]Model D500, 500 L/s
[15]Within the original design a CF40 bellow could allow to displace the window optical access in case of Li aggregations on the inner surface. Unfortunately the bellow got damaged during the assembly procedure and it is not present in the final setup.
[16]Vaqtec, UV grade sapphire viewport with 24 mm optical access. AR coated on atmosphere side for 671 nm.

coating, arising in this case from the exposure to the Li beam emitted from the oven. Furthermore sapphire windows, contrarily to fused silica windows, can be heated up to 450° without damage. In our apparatus the window is constantly kept at 210°[17] to facilitate the sublimation of Li depositions.

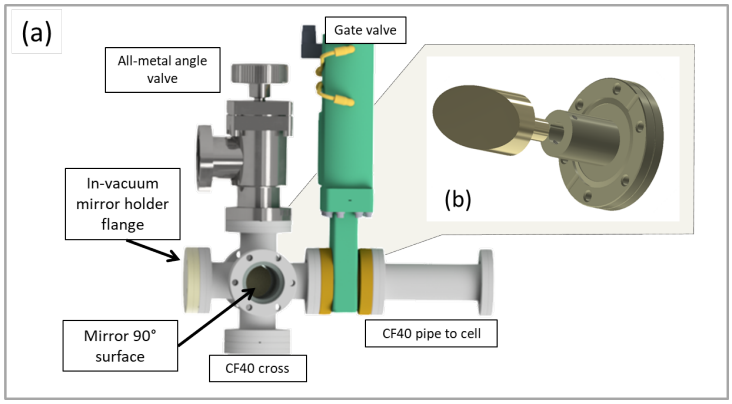

Figure 2.6: (a): In-vacuum Cr mirror chamber; a CF40 pipe connects the structure to the cell, a gate valve seals the main vacuum in case the mirror has to be exchanged or moved. (b): mirror and mirror holder CAD model.

Two opposite CF40 entrances of the chamber are instead exploited for connecting the Cr ZS tube and to provide optical access to the Cr ZS light beam. Due to the high sublimation temperature of Cr, in this case surface coating cannot be avoided by heating up the window. As an alternative, I designed an in-vacuum mirror with a 90° reflecting surface, that is installed within a 6-ways CF40 cross, see picture 2.6(a): the light is shined from a lateral window outside the effusion cone of Cr atoms, and reflected onto the oven by the 90° mirror. The mirror surface will be soon coated with Cr, which is a good reflector for 425 nm light and will thus anyway allow for a proper operation of the mirror over time.
In order to ensure a flat and homogeneous Cr coating, I relied on the experience gained by other research groups on already running setups [4, 85] and decided to realize the mirror from a SS polished substrate[18], which was further coated with Cr. The resulting smooth substrate provides an optimal flatness of the reflective surface, whereas the Cr coating ensures a good

[17] Fix band heater from Watlow, model *Miniband*.

[18] The SS polishing was obtained by means of a lapping procedure. The mirror was manifactured by the local company Pecchioli Research.

roughness, while being still chemically compatible with Cr itself[19]. To avoid uncontrolled and detrimental chemical reactions, the mirror surface does not have any protective layer, which makes the object very delicate to handle and not cleanable.
An Al substrate could have been preferable in terms of weight and clamping strength, but at the cost of a reduced edge sharpness. Nevertheless, the elliptic shape of the reflecting surface has limited the mirror flatness to $\lambda/2$ due to machining difficulties.
The mirror and its holding structure are shown in Fig. 2.6(b). The mirror sizes are such to maximally exploit the housing cross section while avoiding contact with the inner walls. The SS mirror substrate has a protrusion which is inserted into the flanged holder. The holder has two threaded lateral holes, exploited two clamp the mirror by means of headless screws. A longitudinal groove along the insertion hole ensures optimum vacuum venting.

2.2 Magnetic fields and coils assemblies

The overall coils assembly implemented on the experimental apparatus is designed on a main driving strategy: the MOT radial field and the two ZS axial fields smoothly merge at the edge of the experimental cell, forming a single, monotonically decreasing profile. As it will be further discussed in the following, this strategy potentially allows to collect all the atoms exiting from the ZS, enabling larger MOT atom numbers and increased loading rates with respect to a standard design.
In this configuration a single pair of coils provides the MOT field for both Cr and Li. The two species can be collected in the MOT either simultaneously or separately within the experimental cycle. The anti-Helmholtz field gradient, optimum for each species, can be eventually tuned by adjusting the current of two additional small coils concentric with the MOT ones, and hosted within the re-entrance of the CF200 viewports. This latter set of coils, primarily devoted to the creation of the Feshbach field, can be switched to the anti-Helmoltz configuration through a custom made circuit.
Given our conceptual design strategy, all the main four coils systems - Cr and Li ZS, MOT and Feshbach coils - result to be strongly interdependent

[19]The Cr layer is actually composed by Cr oxide. Al coating would have been an alternative, but it is less mechanical resistant to scratches and high temperatures. The surface roughness is of $\sim 2\,nm$ (average peak-valley distance).

one from the other.
In the next I describe the iterative designing work that I carried out in order to define the overall coils assembly. Then, I will present the main setup components, motivating the choice of a merging configurations.

2.2.1 Zeeman slowers coils

As already anticipated, the atoms emitted from the ovens are slowed down by two ZS: a resonant laser beam, counter-propagating against the atomic flux, slows down the particles thanks to momentum transfer during several absorption/spontaneous emission cycles. A decreasing axial magnetic field maintains the atoms in resonance with the laser light by compensating the Doppler shift of the resonant transition through a spatially varying Zeeman shift. Imposing a constant deceleration a, the field profile $B(x)$ along the atoms propagation axis is set by the well known equations [86]:

$$a = \frac{(v_i - v_f)^2}{2L} \tag{2.2a}$$

$$B(x) = \frac{1}{\mu}(\delta_l + k\sqrt{v_i - 2ax}) \tag{2.2b}$$

δ_l and k stem for the laser light detuning and wavevector modulus, respectively; μ is the magnetic moment expressed in units of $\mu_B/\hbar$, being μ_B the Bohr magneton. L denotes the length of the ZS, v_i the maximum velocity of an atom captured by the ZS, and v_f its velocity at the ZS output.

The value of v_f is upper bounded by the maximum MOT capture velocity; typical values are a few tens of m/s, and depend both upon the MOT beams size and intensity, as well as upon the magnetic field gradient.
The value of v_i sets instead the maximum atomic flux that can be collected within the MOT. Suitable values for v_i must be defined in relation to the effused velocity distribution described by Eq. (2.1), and reported in Fig. 2.2 for the case of Cr and Li.
In any case, the resulting deceleration must be such that $a < a_{max} = \hbar k\Gamma/(2m)$, a_{max} being set by the intensity saturation limit. For this reason, the deceleration is usually expressed in terms of a *safety parameter* $\eta < 1$, yielding $a = \eta a_{max}$.

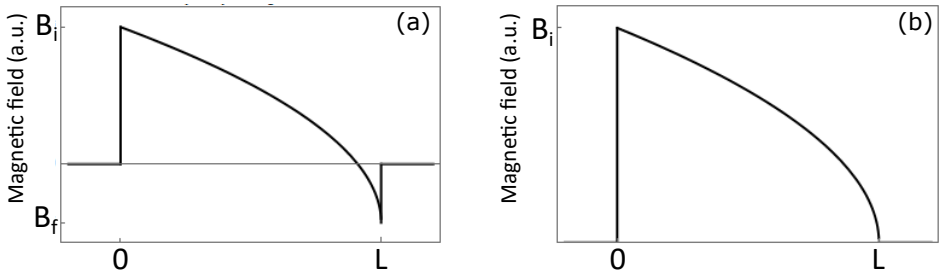

Figure 2.7: Sketches for the ideal ZS field in the non spin flip configuration (a), and in the spin flip configuration (b).

Finally, the laser detuning δ_l sets the maximum and minimum values of the exploited axial magnetic field. In this respect, both Cr and Li ZS implemented on our setup have a non-spin flip design, see Fig. 2.7(a): in this case the field has the same sign all along the ZS length, with $B(L) = 0$. This configuration avoids low field regions along the ZS path, which is of extreme importance to maximize the ZS efficiency in the case of ^{53}Cr, as I will explain in more details in the following.
On the other hand, the non-spin flip configuration has the drawback of requiring high initial magnetic fields to ensure a large value of v_i, and, most importantly, the condition $B(L) = 0$ implies that the ZS light is fully resonant with the exiting atoms, that is, with the MOT atoms. As a consequence, the ZS laser beam can perturb (heat or even push away) the collected atomic cloud.

Another limitation to the MOT collection efficiency which has to be taken into account while designing a ZS is set by the divergence of the atomic beam. The divergence is generally caused by two main contributions to the atomic transverse velocity: one is intrinsically possessed by the thermal atoms as they exit the oven aperture; the second is induced by spontaneous emission of photons with isotropic direction probability within the ZS path.
The first contribution is cured by focusing the ZS beam on the oven nozzle, profiting of its off-axes $\vec{k}$ components. Experiments can also exploit couples of counter-propagating laser beams transversally shined at the output of the nozzle, as we do for Cr atoms in our setup. Further improvement is gained by maximizing the solid angle subtended by the MOT volume by reducing the ZS length. For this reason, both our Cr and Li ZS have a compact design, with $L \sim 50\, cm$.

The second contribution to the atomic transverse velocity is reduced by minimizing the distance d between the ZS output and the MOT. Here the atoms move at the low final velocity v_f, and hence accumulate the largest amount of transverse path $r_\perp$. Recalling that the number of photons absorbed by an atom within the ZS is $N(t) \simeq a(v_i, v_f)t/v_{rec}$, being $v_{rec} = \hbar k/m$ the recoil velocity, one has:

$$\begin{aligned} & r_\perp = v_{trans} \times t_d = v_{rec}\sqrt{N(t)} \times t_d = \sqrt{v_{rec} a t_i} \times t_d \\ & \text{with} \qquad t_i = \frac{v_i - v_f}{a}; \qquad t_d = \frac{d}{v_f} \end{aligned} \tag{2.3}$$

where t_i is the time spent in resonance within the ZS. This estimate gives a lower bound for $r_\perp$: it does not take into account the initial transverse thermal velocity, the transverse path accumulated within the ZS, and the additional scattering of photons along the distance d, which is dominant in a non-spin flip configuration.
Under this approximations, the maximum oven emission angle interested by the MOT capture section of radius R_{MOT} reads:

$$\theta(v_i) = \arctan \frac{R_{MOT} - r_\perp(v_i)}{L} \quad \text{for} \quad R_{MOT} - r_\perp(v_i) > 0 \tag{2.4}$$

Inserting Eq. (2.3) and Eq. (2.4) in Eq. (2.1) and integrating over all the ZS velocity classes $\{v_i\}$, one can give a rough estimate of the atom number captured by the MOT as a function of the distance d.
Our experimental chamber is characterized by an uncommonly large radius, see Sec. 2.1.3: even assuming a direct connection of the ZS output to the cell, we would have $d \sim 15\,cm$. Comparing the expected captured flux with respect to a more standard situation where $d \sim 8\,cm$, I could estimate a reduction of the collected atomic fraction as large as $\sim 95\%$. For this reason, I have decided to get rid of the spacing between ZS field and MOT field by merging the two together, as anticipated in the introduction to this section.
I carried out the overall designing work starting from the determination of the Cr ZS profile. This choice is due to the availability of an already existing ZS for Cr atoms, that could be modified only to some extent, as explained in the following.

Cr Zeeman slower

As already anticipated above, a non-spin flip design is of crucial importance in the case of fermionic ^{53}Cr. Indeed, at ~ 25.4G the ^{53}Cr hyperfine spec-

trum is characterized by a so-called "bad crossing" [4]: namely, two states adiabatically connected at zero field with $|F = 11/2, m_F = +11/2\rangle$ and $|F = 9/2, m_F = +7/2\rangle$, respectively, become degenerate. This allows the atoms to escape from the main cooling transition $|F = 9/2, m_F = +7/2\rangle \longleftrightarrow |F = 11/2, m_F = +11/2\rangle$ whenever a residual component of σ^- light is present within the ZS beam. Although this issue may be mitigated by exploiting high quality polarization optics, it will be a rather unavoidable problem: in fact, our ZS in-vacuum mirror will get coated by Cr atoms with time, and therefore won't ensure a perfect conservation of the light polarization. Nevertheless, in our MOT-ZS merging configuration, the critical field region is reached only at the very edge of the MOT capture volume, and eventual losses can be hindered by finely increasing the MOT gradient.
Table 2.1 summarizes the parameters that I have chosen to design the ideal Cr ZS profile.

v_f	$40\, m/s$
v_i max.	$400\, m/s$
$L + d$	$61\, cm$
δ_l	$-20\, \Gamma$
η	~ 0.3
B_i	$600\, G$

Table 2.1: Design parameters for the ideal Cr ZS magnetic field curve. η and B_i are derived from the above listed ones.

In order to reproduce such a profile, I made use of the first segment of an already available spin flip ZS, whose sustaining structure has been already presented in Sec.2.1. Five transversal discs welded to the holding tube define four different decreasing coils (from left to right in Fig. 2.8). Each coil is composed by continuously winded layers, with varying axial length such to reproduce a conical shape. A small correction coil is also winded between the first and the second coil from left, onto the outer surface. The exploited enameled wire has a nominal diameter of $1.8\, mm$. Each coil is equipped with independent voltage contacts.

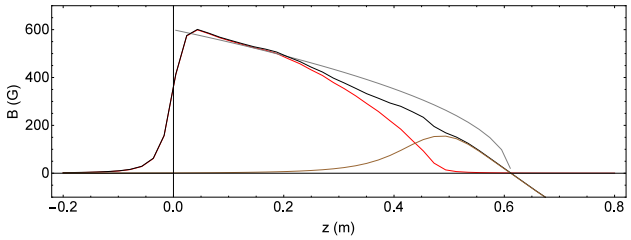

Figure 2.9: Cr ZS field implemented in lab. Gray: ideal field profile; red: ZS optimized coils profile (18 A, 19 A, 19 A, 19 A from left to right coils); brown: MOT profile along the ZS axes; black: total ZS field profile.

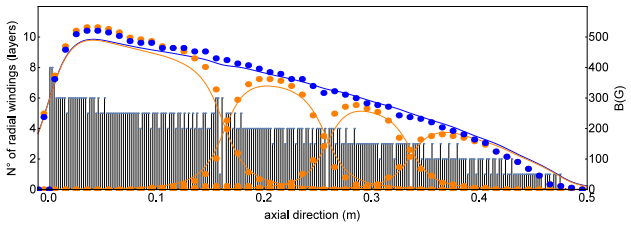

Figure 2.8: Scheme of coils setup composing the CrZS. Histogram indicates the number of layers at each position, in steps defined by the wire thickness. Dots reproduce the experimental data taken at $\sim 5\ A$ with a Hall probe, and rescaled to a current of 15 A for the single (yellow) and total (blue) field. Solid lines (same color code) reproduce theoretical field profile expected at 15 A for an effective wire diameter as explained in the main text.

[H]

First of all, I simulated the expected magnetic field along the ZS axis and compared it with the actual field measured with a Hall probe. To obtain a good matching, I increased the ZS wire diameter by a correction factor (8.33 %) within the simulating model, accounting for winding packaging imperfections. The resulting theoretical profile (solid lines) is compared to the experimental data (dots) in Fig. 2.8, yielding a satisfactory accord.

Second, I made use of the simulated curves to introduce a guess for the MOT field profile that could optimize a smooth merging just upon adjusting the ZS coils currents. The resulting MOT design, presented in Sec. 2.2.2, was optimized to obtain a gradient of $\sim 20\, G/cm$ with less than 40 A, which is commonly exploited for Li MOT clouds.
The final matching configuration is reported in Fig. 2.9.
By performing a classical simulation of the average force experienced by the traveling atoms, I checked the influence of the mismatch between the best

final curve and the ideal one, which causes a non-constant deceleration along the ZS path. Nonetheless, I obtained a value of the safety parameter η that never exceeds 0.7, and a final velocity of 45-50 m/s.

Li Zeeman slower

Once the MOT coils profile has been defined and optimized to merge the Cr ZS, I identified an optimum configuration for the Li ZS. The ideal curve characteristics are listed in Table 2.2. Rather than designing a ZS square-root profile ending at the MOT center (gray curve in Fig. 2.10), I decided to implement a two-sections profile: the first part is composed by the square-root profile of the ZS coils (black), the second by the MOT field profile (brown). To do so, I simulated the slowing effect of the MOT field alone, starting from the decided merging point, and I extracted the maximum initial velocity v'_f that this field can capture and slow down to the desired $\sim 45\, m/s$ range. I then designed the ZS coils curve such to yield v'_f as a final velocity in correspondence of the merging point.

v_f	$45\, m/s$
v_i max.	$700\, m/s$
L+d	$61\, cm$
δ_l	$-18\, \Gamma$
η	~ 0.3
B_i	$750\, G$

Table 2.2: Main design parameters for the Li ZS magnetic field curve. See main text for solid curves color meaning.

Finally, I designed a set of ZS coils that could best reproduce the total overall field. The resulting design is shown in Fig. 2.11. The Li ZS is composed by 9 main coils, winded with a $0.8\, mm$ enameled wire[20], separated by $2\, mm$ thick SS disks. All coils have a square section to simplify the winding procedure, except for the first one that features a conical shape at the outer layers, in order to increase the steepness of the field in the rising region. Additionally, a small full conical coil is winded before the main 9

[20]Copper wire produced by Essex, specific for industry applications at high magnetic fields and winding friction stresses: Magnetemp CA-200 Gr 2.

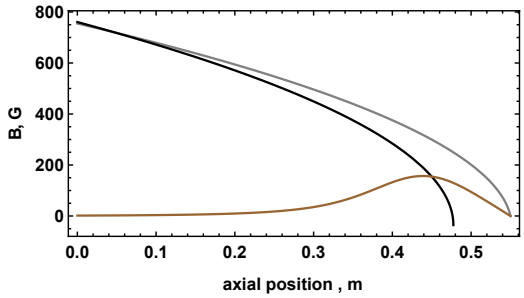

Figure 2.10: Rather than corresponding to a ZS square-root profile ending at the MOT center (gray curve in Fig. 2.10), the Li SZ overall profile is composed by two distinct sections: a first one has a square-root profile, and is provided by the proper ZS coils (black), the second section is directly by the MOT field profile (brown).

ones. Operating at an opposite current, this coil is optimized to cut the rising field tail.

The expected axial field curve is also reported in Fig. 2.11 (solid blue curve), and compared with the field measured with a Hall probe inserted within the holding tube (blue dots). The discrepancy in the field intensity may be ascribed to an imperfect probe orientation relative to the ZS axis, or to a small discrepancy between the supply current and the theoretical one. As for the Cr ZS, I simulated the ZS deceleration and efficiency, obtaining a fluctuation of η between 0.3 and 0.45 along the ZS, and an expected output velocity of 45-50 m/s.

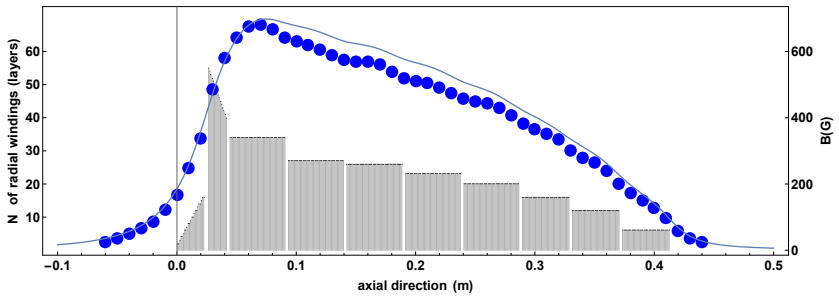

Figure 2.11: Sketch of the coils structure (black histogram). Total simulated field (blue solid curve) measured field (dots) at a current of $2A$, not comprehensive of the contribution of the first small conical coil, which got broken during the manufacturing process.

The coils are cemented by a mixture of resin glue (very resistant at high

temperature) plus a flexibilizer[21] that reduces the possibilities of cracks during heating and long operation, able to resist at the typical baking temperatures.

2.2.2 MOT coils

The MOT coils and holding structure are designed in order to reproduce both the radial field profile fixed by the merging configuration and the desired gradients. The final products were manufactured by the German company Oswald Elektromotoren GmbH, with the characteristics listed in Table 2.3.

Layers	2×4
Loops	20
Current	$37\,A$
Inner radius	$72\,mm$
Wire thickness	$4\,mm$ + enamel
Relative minimum distance	$15\,cm$

Table 2.3: Main design parameters for the MOT coils, corresponding to a final MOT gradient of $20\,G/cm$

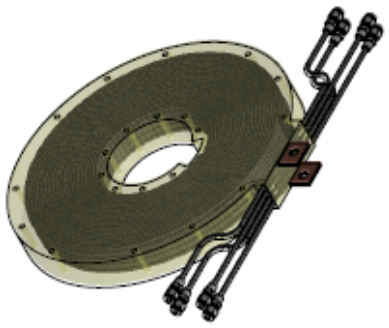

Figure 2.12: CAD sketch of one MOT coil, provided by Oswald Elektromotoren GmbH.

The large radius dictated by the merging design imposes a large vertical spacing between the two coils to reproduce a MOT anti-Helmholtz configu-

[21] Both glue and flexibilizer were delivered by Duralco.

ration. The vertical position is anyway lower bounded by the large size of the experimental chamber plus the thickness of the flanges of the re-entrant windows. At these distances, on the order of 7.5 cm from the center plane, the current required to obtain the required radial field in the merging region (of the order of $\sim 200\,G$) can be very high, and the coils must be water-cooled. For this reason, I opted to wind up the coils with a hollow core copper wire, which enables a very efficient water cooling. The hollow core wire has a square section[22] to facilitate a compact winding.

Additionally, the manufacturer embedded the assembled coils within a custom designed resin structure that self-constraints the coils and automatically provides a sustaining frame, see Fig. 2.14. The resin protrudes inward and outward along the coils radius; M6 holes are drilled within the exceeding thickness to allow the insertion of SS threaded bars, which constraint in a concentric position the two MOT coils, and also relatively to the Feshbach coils, and will fix the whole system to the experimental table (see Fig. 2.18(a) in Sec. 2.3.1 and text therein).

Fig. 2.14 also shows the water connectors assembly: each coil is composed by a superposition of four two-layers sections, with an input and output water connector at each section, to ensure a homogeneous water flow. All sections are soldered in series, with two copper flags to serve as general voltage connectors.

In order to test the final coils structure supplied by the manufacturer, I measured and compared the magnetic field profile with the one expected by the simulation. I did this both along the vertical and the horizontal directions, measuring the vertical field component with a Hall probe. Examples of such characterizations are shown in Fig. 2.13(a) and (b). Apart from small discrepancies between the amplitudes of the measured and simulated field (see caption in Fig. 2.13), which I mainly ascribed to a mismatch between the nominal and effective sensitivity featured by the Hall probe, I observed a somewhat faster decay of the vertical field component within the horizontal plain (see refFigMOTcomp(b), black dots) at large radial position with respect to the simulated one (black solid line). I found that this discrepancy is due to a thinner enamel layer thickness of ~ 0.1 (yielding the red solid curve) featured by the coils wire, with respect to the expected one, of $0.3\,mm$. The exact wire thickness and total MOT radius cannot be measured due to the

[22]The wire was supplied by the manufacturer. The wire has a thickness of 4 mm, inclusive of insulating enamel, and a size of the hollow square section of $2.5\,mm$.

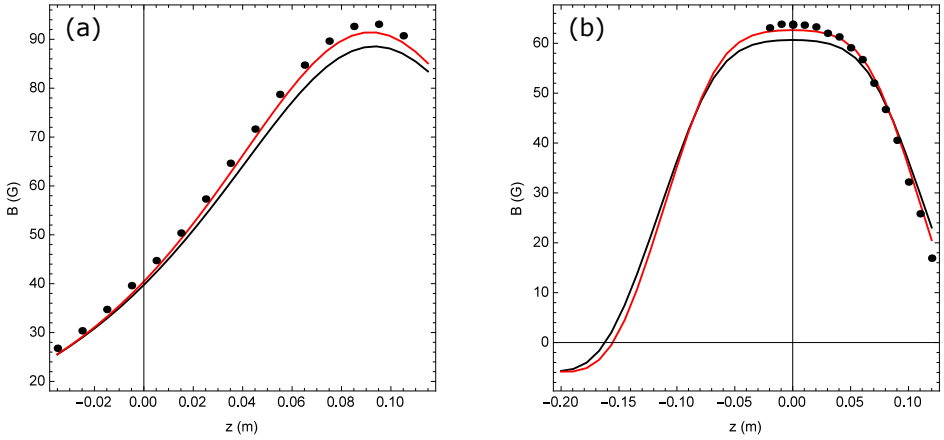

Figure 2.13: Measured (points) and expected (solid curves) vertical field component produced by one single MOT coil at $10\,A$ as a function of the probe vertical position along the coil axial direction (the y-axis origin indicates the atoms plain position) (a), and as a function of radial direction (the x-axis origin indicates the axial coil center) (a). In both figures the black solid line corresponds to the field expected for a coil winded up with a wire provided with a $0.3\,mm$ enamel thickness. The final objects presented instead an enamel thickness of $\sim 0.1\,mm$. At this value, the behaviors exemplified by the red curves are expected. The matching between the expected field amplitude and the measured one was obtained allowing for a variation of the 10% of the probe gain.

resin encapsulation. Nonetheless a deviation within $2\,cm$ of the total coil radius is not expected to affect the efficient merging of the MOT field with the ZS one.

The very large size of the coils implies a very large inductance. While this helps to suppress high frequency noise on the field, it prevents a fast tuning of the magnetic field during the experimental routine. To solve the issue, we installed an insulated gate bipolar transistor system[23] (IGBT) at the power supply output, which enables to reduce down to $\sim\ ms$ the MOT switching off time. We also implemented a magnetic field transducer circuit in series to the coils, to create an input monitoring signal for a PID, which in turns stabilizes the power supply output in voltage control mode. This reduces the current fluctuations during fast ramps of the applied current, induced by the L-C circuit composed by the power supply internal capacitors and the coils themselves.

[23]Semikron, SKM400GAL12E4.

2.2.3 Feshbach coils and water cooling structure

A pair of coils in Helmoltz configuration is required during the experimental cycle to create tunable homogeneous magnetic fields. This will allow to search, pinpoint and exploit both inter- and intra-species Feshbach resonances.

Layers	2
Loops	25
Inner radius	64 mm
Wire width	3.5 mm + enamel
Wire thickness	0.6 mm + enamel
Relative minimum distance	66.7 mm

Table 2.4: Main design parameters for Feshbach coils.

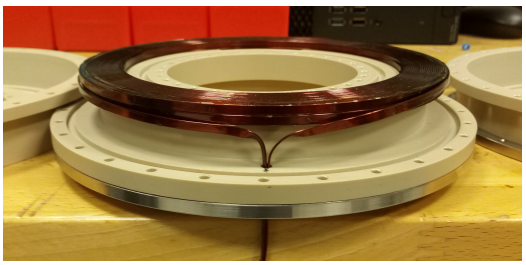

Figure 2.14: Photo of one coil produced by Oswald Elektromotoren GmbH, installed within the water cooling case.

In order to obtain large magnetic fields with relatively low operation currents, I decided to install the Feshbach coils as close as possible to the atom position by exploiting the re-entrance of the top and bottom CF200 viewports presented in Sec. 2.1.3. The coils, also in this case manufactured by Oswald Elektromotoren GmbH, are winded up with a flat ribbon-shaped wire to allow a very compact design which ensures a free optical access to the cell within a diameter of $\sim 10\,cm$.
The parameters of the designed coils are reported in Table 2.4 and they were optimized to obtain homogeneous fields up to $\sim$ 1000 Gauss with less than $200\,A$. As an example I report in Fig. 2.15 the Feshbach field profile obtained at 130 A, and the relative potential curvature that I calculated for Li atoms in the ground state. In order to check the vertical magnetic field produced

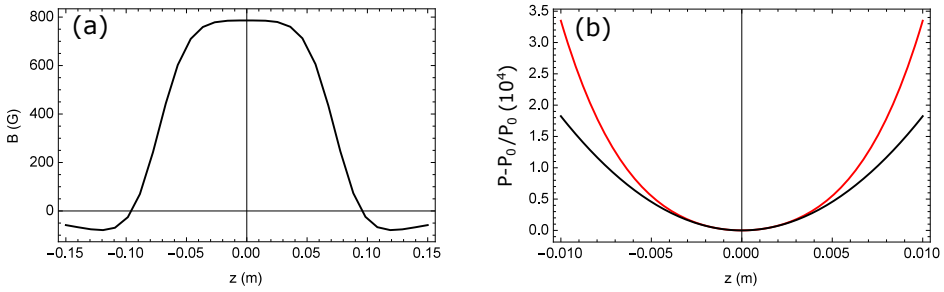

Figure 2.15: (a): Magnetic field profile along radial direction on the atom plane created by the two quasi-Helmoltz coils at 130A. (b): simulation of the potential energy felt by Li atoms in the ground state (black) and parabolic fit (red). The parabolic approximation is extremely good within $\sim mm$ from the center (typical cloud size are $\sim 10^2 \mu$m); the fit curvature corresponds to $\sim$ 2.5Hz.

by the single coil close to the atom position, I recorded the signal yield by a Hall probe sliding on a radially oriented guide guide placed at 2.9 cm from the bottom surface of the coil, with the chip surface facing the coil plane. Fig. 2.16 shows the comparison of the expected field with the measured one for one single coil. The observed asymmetry, due to a slight but sizable tilt of the sensor with respect to the coil axis, is well reproduced by the simulation taking into account the contribution of both the radial and axial field projections along the direction perpendicular to the sensor surface.

Together with the coils design, I projected a holding system that ensures the concentricity of Feshbach and MOT coils and at the same time provides the external water cooling of the Feshbach coils. Figures 2.17 shows the housing structure of one single coil[24]: it consists of a toroidal case that forces the coil in place both axially and vertically, thanks to inner protrusions. The empty gaps between the protrusions drive the water flow, ensuring a homogeneous cooling at standard water pressures and temperatures.
The outer dimensions of the case are such that the desired distance between each Fesbach and MOT coil is obtained by directly fixing the latter one on top of the case, see again CAD section of Fig. 2.5; amagnetic threaded rods are inserted through the M6 holes drilled within the inward resin thickness of the MOT coil, and screw the Feshbach case structure in place. The corresponding set of threaded M6 holes drilled onto the top surface of the case is visible in figure 2.17(a).

[24]The housing was realized by the external company RMP.

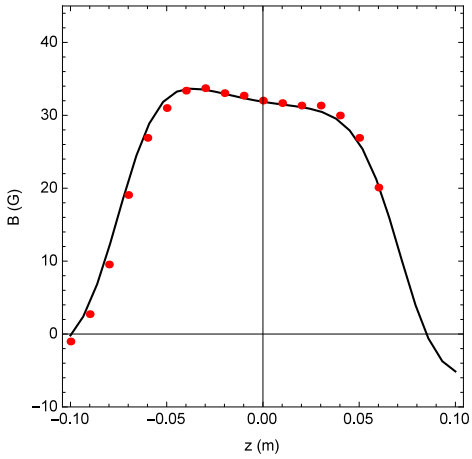

Figure 2.16: Measured (dots) and calculated (solid line) vertical field component along the radial direction created by one single coil at 2.9 cm from the bottom surface of the coil, at a current of 10 A. The calculation takes into account the non-zero sensor tilt with respect to the vertical axis.

Two amagnetic 316LN SS threaded rings are housed at the inner and external perimeter of the toroidal case, and serve as plate nuts for the amagnetic 316LN screws that seal the case.
The cases are realized in peek material, a plastic commonly used for industrial applications; such a material combines good resistance to heating, strains and bending, with small weight and complete insensitivity to magnetic fields. The technical drawing of the object is reported in Appendix B.

2.3 Final setup assembly and vacuum preparation

In this last part of the chapter I describe the final assembly work of the vacuum setup described in the previous section.
A first part of the section presents the mechanical structure that holds the setup in place on the optical table, and that allowed for a step-by-step assembly of the apparatus.
A second part describes the so called pre-pumping and bake-out procedure, namely the procedure that is needed to create the vacuum within the machine for the first time. This was also done in steps, in parallel to the assembly

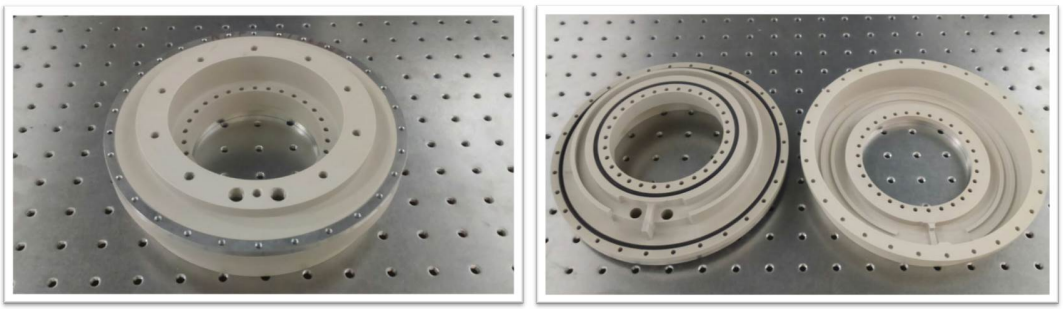

(a) (b)

Figure 2.17: (a): top view of the water cooling case of the Feshbach coils; M6 holes for mechanical holding and M10 holes for water connectors are shown. The outer SS sealing ring is also visible. (b): cup and lead, open; the photo shows the external and internal o-ring, and the inner peek protrusions which keep the coil in place and drive the water flow.

work, as further explained in the following.

2.3.1 Vacuum setup holding structure

The complete vacuum setup that I have described so far must be positioned onto the dedicated table, at the desired high. To do this I designed and built a structure made of aluminum Bosch profiles, that serves to sustain both the vacuum apparatus and six optical breadboards, see again Fig. 2.1(a).

The structure is mainly divided in three independent parts: two of them support the ovens sectors, from the heated reservoir up to the gate valve; the third part holds instead the six custom optical breadboards that surround the experimental chamber. The shape of each breadboard is optimized to lay as close as possible to the chamber. This has two advantages: it provides a working surface for a close optical access, and it allows to clamp all the vacuum components that are protruding from the experimental cell (Cr and Li ZS, pumping CF63 cross, Cr in-vacuum mirror chamber).

Due to its significant weight, the system composed by the experimental chamber plus MOT and Feshbach coils is furthermore sustained by an independent holding structure. The structure exploits the narrow ring of cell surface left free by the bottom re-entrant window flange, as shown in Fig.

2.18(a): two 8 mm thick SS forks are introduced under the cell to reach this free surface, the two forks are then connected to 350 mm long SS legs of 3.81 mm diameter [25], clamped to the table.

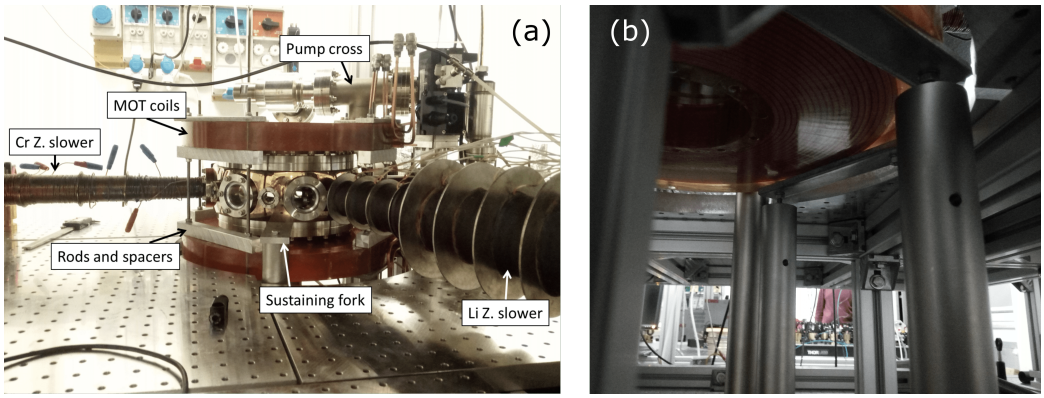

Figure 2.18: (a): one of the two SS forks that are introduced below the cell, and the system of rods and spacers that clamp the two MOT coils together but maintaining the relative distance fixed. (b): one of the 3 coils legs, fixed by means of the threaded rod to the horizontal SS bar and thus to the MOT coil.

The Cr and Li oven sections are instead held by a simple structure composed by four Al frame legs and by additional horizontal frame bars which block the vacuum components at the desired height. The vertical and horizontal frames are visible in Figs. 2.1, 2.3 and 2.4, respectively.

In order to install the whole vacuum apparatus, we first positioned the cell onto the two dedicated sustaining system at the center of the table, and surrounded it with the main frame structure and the breadboards. We proceeded by connecting to the cell the in-vacuum mirror chamber, the pump cross, and the two ZS plus the differential pumping stages. We then fixed all these protruding elements to the breadboards in order to completely constrain the cell.

At a later stage, we matched the previously assembled and independently hold Cr and Li ovens sections together with the central setup section. In doing this, the presence of the bellow at the junction point between the differential pumping stages and the oven gate valves has been of extreme importance to reduce the stress applied to the junction in case of slight relative misalignment.

[25] By Thorlabs.

Finally, we installed the top and bottom MOT plus Feshbach case structures around the experimental cell. The two structures are kept at the correct relative spacing by a system of nuts plus counter-nuts along the six threaded rods inserted within the resin outside thicknesses. Large amagnetic bars horizontally connect the rods in pairs, preventing any angular torsion, see again Fig. 2.18(a). Three of the rods are prolonged downwards below the cell, and are screwed into further three 3.81 mm SS legs, see Fig. 2.18(b). Each leg is then fixed to the table. In this way, the whole coils system is independently held on these three legs, suspended around the experimental cell.
In order to install the coil system at the desired distance with respect to the re-entrant top and bottom windows, I designed Al spacers to be temporarily introduced between the bottom MOT coils and the bottom window flange to adjust the three legs at the right height. Other dedicated spacers were then placed onto the top flange surface. The second coils structure was inserted from top and laid onto the spacers; the nut plus counter-nuts system could then be tightened at the correct final position.

2.3.2 Pre-pumping and bake-out procedure

The pumps installed on the apparatus can be safely activated only at a pressure lower than $\sim 10^{-7}\, mBar$. In order to reach this starting pressure it is necessary to first evacuate the setup by means of a pre-pumping system, composed by Turbo pumps and dry scroll pumps[26].

The vacuum setup is designed such as to allow a temporary connection to the pre-pumping system in correspondence to each of the installed pumps: referring to the overview in Fig. 2.1, it is possible to recognize the presence of an all-metal angle valve[27] at both the Cr and Li oven chambers, on top of each of the differential pumping stage cubes, and on top of the CF63 cross where the D500 is installed. This arrangement ensures a homogeneous pre-pumping of the apparatus, and it guarantees optimum operation starting conditions for the ion-pumps and the NexTorr pumps. An all-metal angle valve is also present at the chamber hosting the in-vacuum Cr mirror. This guarantees a connection to the pre-pumping stage and a good vacuum conductance flow

[26] Varian Technologies.

[27] CF40 valves: MDC model MAV-150-Vand. CF63 valves: Varian Technologies model 9515032.

also in this area. Moreover, it will enable in the future to re-establish UHV conditions after replacement of the in vacuum mirror.

Assuming a correct activation of all pumping stations, I estimated that the overall ion and NEG pumps system installed on the apparatus could ensure a final pressure of $\sim 10^{-11} \div 10^{-12}\, mBar$ within the experimental cell. Standard vacuum pressures are lower limited at $\sim 10^{-12}\, mBar$ by outgassing of H and H_2 from the SS walls of the apparatus itself. Indeed, these gases are so light that any pumping method is quite inefficient, although NEG elements have better performances relative to standard ion-pumps.
Besides H and H_2, many other atoms and molecules are outgassed from the SS surfaces (O_2 in primis, H_2O, etc.), and they all contribute with even higher partial pressures than the ones of H and H_2. Furthermore, any residual deposition (especially organic deposition) onto the apparatus inner surfaces may release material during operation, preventing the pressure to reach the desired UHV level.
For these reasons, the pre-pumping procedure needed for the first vacuum realization must be combined with a so called bake-out of the system: namely, the setup must be constantly and homogeneously kept at the highest allowed temperatures during the pre-pumping in order to enhance the background molecules mobility, as well as the outgassing of the materials and the chemical decomposition of any organic residual.
Unfortunately, maximum temperatures are in general limited below 200° by of the presence of delicate vacuum elements, such as optical viewports: in these element the glass is welded to the SS flange by means of heating techniques[28], if the bake-out temperature is higher than the fabrication one, the glass starts to tilt or even leak. The efficiency of the bake-out procedure at these relative low temperatures is compensated by prolonging the procedure for longer time. Nonetheless, standard limits due to H and H_2 outgassing would require unfeasible timescales to be exceeded.

In order to speed up the bake-out and at the same time minimizing the H and H_2 outgassing, I decided to operate a four days long pre-assembly baking of each single vacuum component separately, exploiting an under vacuum HT-oven. Most of the vacuum components have been chosen to be entirely made of SS: in these cases I could safely apply bake-out temperatures[29] up to

[28] Typically a metal powder is placed at the contact perimeter between a metal ring and the glass, and the whole object is then heated at ∼200° to let the powder melt and join them together. The metal ring it then soldered to the flange.

[29] SS can bare up to a maximum temperature of ∼450°: beyond this threshold the alloy

400°. Under these conditions the decided timescale of 4 days is the minimum one that is expected to push down the boundaries of UHV-pressures due to Hydrogen outgassing in SS [87–89]. Nevertheless, many parts were baked out at lower temperatures due to their composite structure (viewports, bellows and gate valves, the Li shutter and the Zeeman slower coils).

After this pre-bake-out stage, we proceeded by assembling the three main apparatus subsections as previously described; we then pre-pumped and baked them independently for circa 10 days. This intermediate stage permitted to test the sealing of the most of the vacuum junctions. The bake-out temperature was maintained by wrapping the assemblies with flexible heating tapes, and insulating them with Al foil. After having connected the three sections together, we proceeded with a second and final pre-pumping and bake-out stage of the overall apparatus for circa 15 days.

The final pressure obtained within the experimental cell is confirmed to be lower than $\sim 10^{-11}$ mBar, below the reading range of the UHV pressure gauge installed at the cell.

starts to suffer from local modifications.

Chapter 3

Optical setup

This chapter illustrates the optical setup exploited to laser cool and trap Li and Cr atoms.
The chapter is structured as it follows. Sec. 3.1 introduces the spectroscopic properties of the Li and Cr isotopes considered in this work, namely the fermionic ^{6}Li, bosonic ^{52}Cr and fermionic ^{53}Cr, respectively.
Sec. 3.2 reports on the optical scheme and laser locking system that I designed and implemented to laser cool ^{6}Li atoms. Sec. 3.3 describes the scheme and locking system exploited for the main cooling transition of both ^{52}Cr and ^{53}Cr isotopes. The design and implementation of this setup was realized in parallel to my work on the Li optical setup implementation.
Aside for the main cooling transition of Cr, at about 425 nm, the presence of metastable D states in the Cr atomic spectrum requires the use of two further red repumper laser lights. Sec. 3.3 illustrates the setup implemented to frequency lock these additional lights, running at 663 nm and 654 nm, respectively.
Sec. 3.4 gives an overview of the optical setup on the experimental table, detailing the beam paths implemented for the ZS and MOT lights of both species around the experimental chamber, together with the imaging beam setup.
Finally, Sec. 3.5 illustrates the main designing feature and the final optical setup of the high-power bichromatic optical-dipole-trap (ODT) exploited to trap and evaporatively and simpathetically cool Li-Cr mixtures. The characterization of the high-power induced thermal lensing effect on the position of the ODT beam waist is the subject of the work of Ref. [5], which is reported in Appendix C. The ODT and the repumper laser lights setups were realized

in parallel during my last months PhD activity within the lab.

3.1 The chromium and lithium atoms

While laser cooling and trapping techniques are well established and relatively easy to implement for Li atoms, the very rich electronic structure of Cr atoms requires a challenging optical scheme, especially for the case of the fermionic isotope.
I present here in the following the main physical properties of the atomic species treated in this work in view of the laser cooling and trapping techniques that we exploit within our experimental routine.

The chromium atom

	Chromium				
Isotope	^{52}Cr	^{53}Cr	^{50}Cr	^{54}Cr	
Nuclear spin	0	3/2	0	0	
Abundance	83.789(18)	9.501(17)	4.345(13)	2.365(7)	%

Table 3.1: Properties of Chromum isotopes [90].

Cr has four stable isotopes, listed in Table 3.1. Fig. 3.1 shows the electronic level structure of the two isotopes of interest for our study, namely the most abundant bosonic isotope ^{52}Cr and the fermionic ^{53}Cr.
The laser cooling light addresses the $|S_3\rangle \rightarrow |P_4\rangle$ transition, which is characterized by a wavelength of 425.553 nm and a natural linewidth of $2\pi \times 5.06 MHz$. In the case of fermionic ^{53}Cr, featuring a non-zero nuclear spin, see Table 3.1, the specific hyperfine cooling transition is $|F = 9/2\rangle \rightarrow |F' = 11/2\rangle$. As shown in Fig. 3.1, the hyperfine structure of ^{53}Cr encompasses about $\sim 1\ GHz$ wide spectral region for the $|S_3\rangle$ state, and a $< 200\ MHz$ wide region for the $|P_4\rangle$ state. This allows to exploit the same laser sources for both isotopes, while suitably tuning the frequencies by means of acusto-optic modulators (AOMs).
In the case of ^{53}Cr, the non-zero probability to excite higher-lying hyperfine states during the cooling cycle requires at least two additional blue repumper lights, as reported in previous studies of this Cr isotope [4]. These transitions

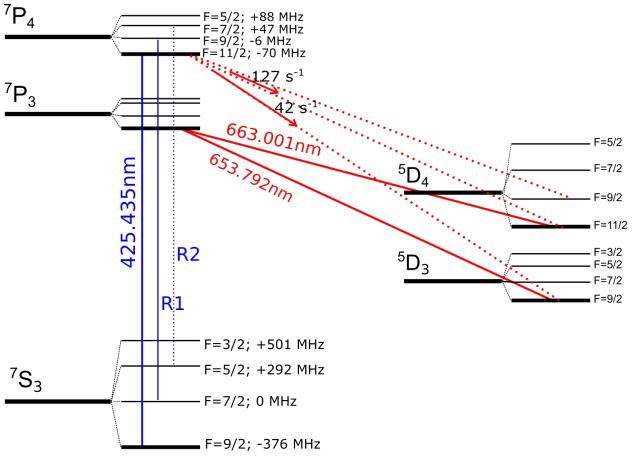

Figure 3.1: Fine and hyperfine electronic structure of ^{53}Cr. Hyperfine splitting values taken from [4].

are indicated in Fig. 3.1 as R1 and R2, respectively. In particular, the R1 repumper light is fundamental to ensure an efficient Zeeman slowing of the atoms due to the "bad crossing" between the excited levels $|F' = 11/2\rangle$ and $|F' = 9/2\rangle$ expected at a magnetic field of $\sim 25.4\,G$, as already discussed in Ch. 2.

Contrarily to the most familiar alkali species, both ^{52}Cr and ^{53}Cr MOTs features strong two-body losses, mainly induced by photon-assisted inelastic collisions. In particular, Refs. [91,92] reports a measure of the two-body loss rate parameter on the order of $10^{-9}\ cm^3 s^{-1}$ for both the bosonic and the fermionic isotopes. This value is about two order of magnitude higher with respect to the typical values found in for alkalis MOTs.

Chromium levels			
Level	J	g_J	$\lvert\mu\rvert$
^7S	3	2.00	$6\mu_B$
^7P	4	1.75	$7\mu_B$
^7P	3	1.92	$5.8\mu_B$
^5D	4	1.50	$6\mu_B$
^5D	3	1.50	$4.5\mu_B$

Table 3.2: Properties of the main Cr atomic energy levels of Cr. Data are taken from Ref. [4].

An additional issue that differentiates the laser cooling of Cr from alkali atoms owes to the fact that atoms in the excited $|P_4\rangle$ state can radiatively decay also into the $|D_3\rangle$ and $|D_4\rangle$ states. The associated decay rate to the $|D_3\rangle$ ($|D_4\rangle$) state is $\gamma_D = 42\ s^{-1}$ ($127\ s^{-1}$). These states are metastable, and feature lifetimes exceeding several tents of seconds [4]. Owing to their large dipolar magnetic moment (see Tab. 3.2), these states can remain magnetically trapped within the MOT quadrupole gradient. This is extremely advantageous, since atomic clouds much larger than those collected in the MOT can be efficiently produced in the magnetic quadrupole, thanks to the fact that metastable states are not affected by the cooling light, and they are hence immune from light-assisted collisions. From these metastable states, the atoms can be repumped back into the cooling cycle by addressing the inter-combination repumper transitions $|D_3\rangle \rightarrow |P_3\rangle$ ($653.973\,nm$) and $|D_4\rangle \rightarrow |P_3\rangle$ ($663.973\,nm$).
For a thorough characterization of the decay rates of the MOT atoms into the $|D\rangle$ states, as well as the two-body scattering properties of these states within our experimental platform I also refer to Ch. 4.

The lithium atom

	Lithium		
Isotope	^{7}Li	^{6}Li	
Nuclear spin	0	1/2	
Abundance	92.41(4)	7.59(4)	%

Table 3.3: Properties of lithium isotopes [90].

Lithium possesses only the two stable isotopes listed in Table 3.3: the most abundant bosonic ^{7}Li, and the fermionic ^{6}Li. Our optical setup is designed to cool and trap ^{6}Li, whose level scheme is reported in Fig. 3.2. The cooling transition is based on the so called D2 line, $|S_{1/2}\rangle \rightarrow |P_{3/2}\rangle$, characterized by a wavelength $\lambda_{D2} = 670.977\,nm$ and a natural width $\Gamma = 2\pi \times 5.87\,MHz$. In particular, the hyperfine cooling transition of interest is $|F = 3/2\rangle \rightarrow |F' = 5/2\rangle$.
Due to the relatively small excited state hyperfine splitting smaller than Γ, the cooling light can populate higher excited hyperfine substates, which can de-excite into the hyperfine ground state $|F = 1/2\rangle$. To bring the atoms

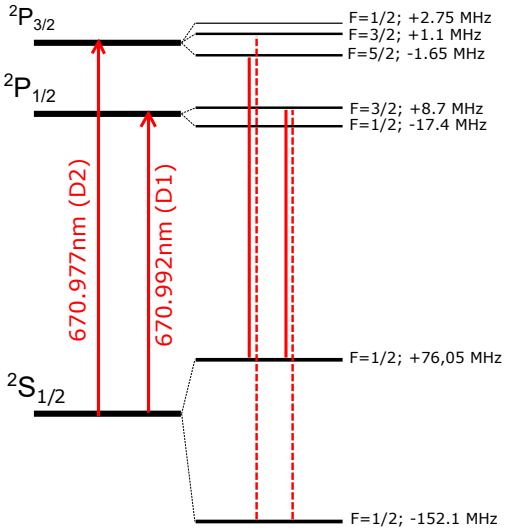

Figure 3.2: Lithium fine and hyperfine splitting electronic scheme. Cooling and repumper transitions for both D1 and D2 spectroscopic lines are indicated by solid and dashed lines respectively. Hyperfine shift values taken from [83].

back into the cooling cycle, we therefore need a repumper light, addressing the $|F = 1/3\rangle \rightarrow |F' = 3/2\rangle$ transition.
In addition to the D2 line, our loading routine also exploits a gray-molasses cooling stage based on the D1 transition $|S_{1/2}\rangle \rightarrow |P_{1/2}\rangle$. This technique was first applied to ^{6}Li in the work reported in Ref. [93], where it was demonstrated that the D1 cooling stage enables to reduce the MOT cloud temperature down to $\sim 50\,\mu K$.
I refer to Ch. 4 for the characterization of our Li MOT cloud, as well as for the optimization of the D1 cooling stage.

Lithium levels		
Level	J	g_J
^2S	1/2	2.0023
^2P	1/2	0.6668
^2P	3/3	1.335

Table 3.4: Main Li atomic energy levels [83].

3.2 Lithium laser system

Figure 3.3 shows the block scheme of the laser setup that I designed and implemented to (i) slow and collect the thermal Li atoms within the MOT, and (ii) further cool them via gray-molasses techniques [93].

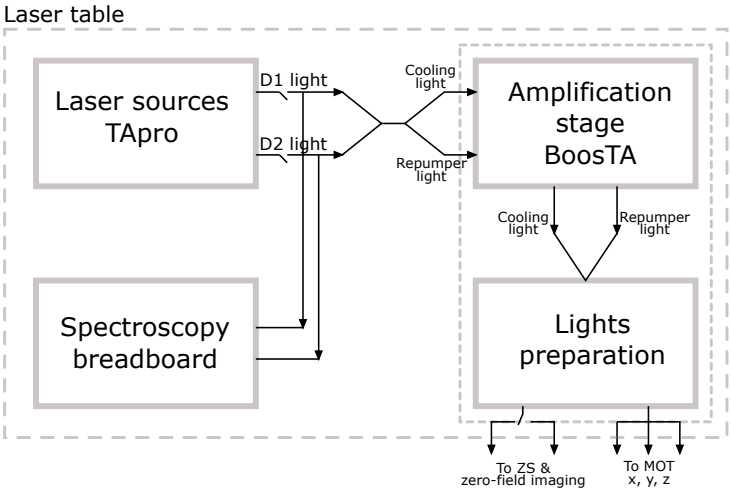

Figure 3.3: Sketch of the lithium optical setup main structure.

Two commercial master lasers[1] at 671 nm provide independent laser sources for the D1 and D2 atomic transitions. The two laser lights are overlapped on a beam splitter cube, so to follow the same optical path: two AOMs are therefore used prior to the mixing cube as fast shutters to select the desired light during the experimental cycle.
The beams delivered by the master lasers are split into a repumper and a cooler laser beam, which are independently amplified by tapered amplifiers (TA)[2]. The two lights are recombined within two common paths which prepare the MOT and ZS beams, respectively. The ZS light is also exploited for zero-field absorption imaging in a switch configuration. The lights are then brought onto the vacuum table by means of five polarization maintaining (PM) fibers.
A dedicated breadboard hosts both the amplification stage and the lights preparation stage. Two pickup beams exiting the main laser sources are sent

[1] Toptica TA Pro.
[2] Toptica BoosTA.

to a laser locking setup onto a dedicated breadboard.
The description of each block composing the optical setup is detailed in the following.

3.2.1 D1 and D2 laser sources and lights preparation

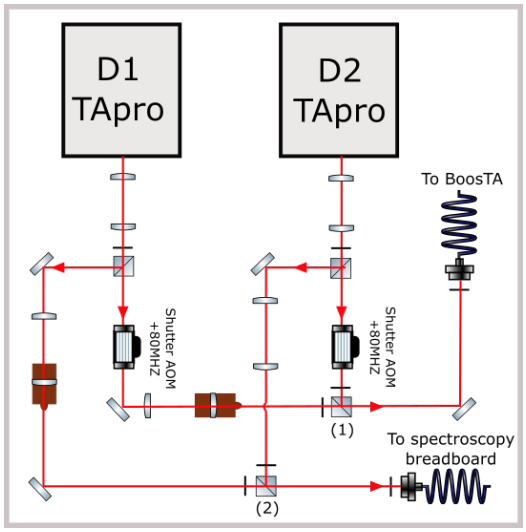

Figure 3.4: D1 and D2 laser light sources setup.

Fig.3.4 shows the main D1 and D2 sources optical setup. The two $+80\,MHz$ single pass AOM exploited as fast shutters are visible in figure.
The two main beams are prepared with relative orthogonal polarization; this allows to recombine them onto a polarizing beam splitter (PBS) cube (1) and to couple them into the same optical fiber: from this point on, therefore, D1 and D2 lights follows the same paths.
The same combining method is applied to the D1 and D2 spectroscopy beams, which are collected before the two shatter AOMs and recombined onto PBS (2) and injected into a common fiber. Fig. 3.5 shows the setup dedicated to the amplification stages and to the splitting into the subsequent paths for ZS, imaging and MOT lights. The first PBS plus waveplate system at the fiber output (1) splits both D1 and D2 light into a cooling and repumping optical path with a $\sim 50 - 50$ ratio.
The paths are composed by two double pass AOMs, centered respectively at $2 \times 80\,MHz$ (2) and $2 \times 200\,MHz$ (3) and adjusted to yield a relative shift

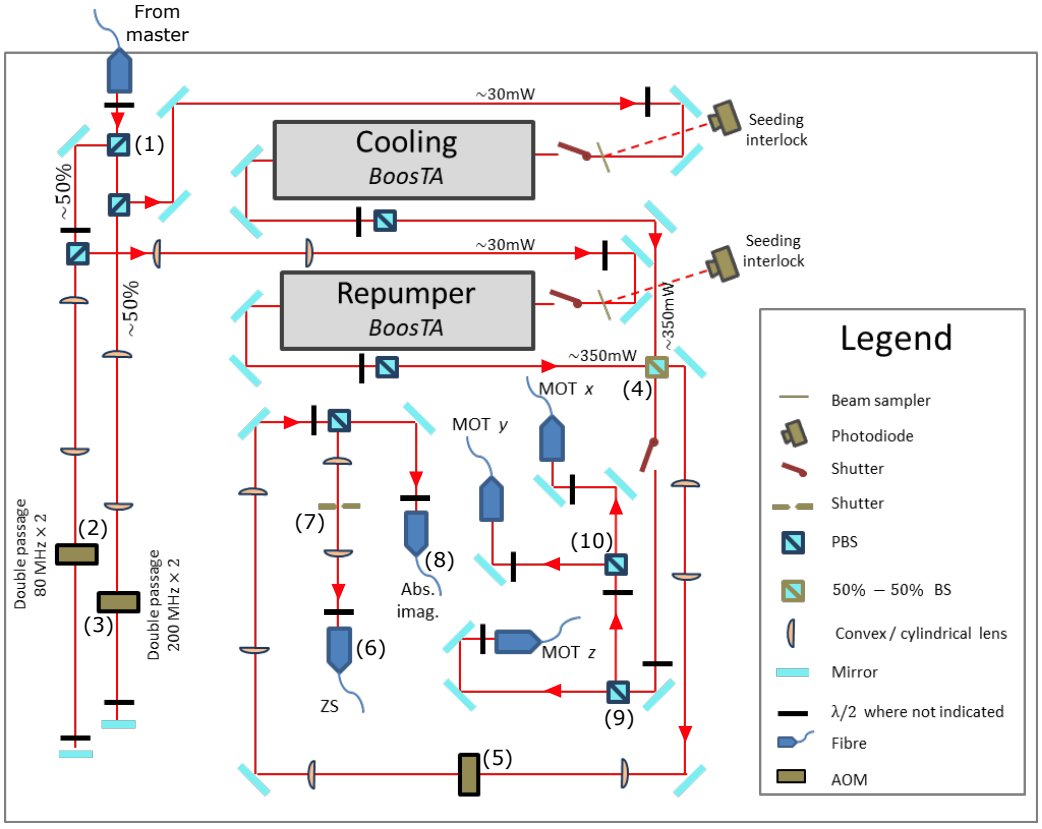

Figure 3.5: Optical setup for amplification and preparation of ZS, MOT and zero field imaging lights, both for the cooing and the repumping frequency.

of $\sim 228\,MHz$, matching the hyperfine splitting of the Li level system, see again Fig. 3.2. The double pass configuration allows for the fine frequency tuning of the laser light while not causing beam misalignment.
The cooling and repumping lights are then independently injected into the Toptica BoosTAs, eventually passing through shaping optics. Owe to the fragility of the BoosTAs chip against long zero-current holding time[3], the amplifiers are injected overnight at low seeding current ($\sim 300\,mA$). For this reason I have built and set an interlock system which monitors the TAs seeding and switch them off in case of too low power injection[4].
The amplified lights are again recombined on a 50-50 non-polarizing BS, marked as (4) in Fig. 3.5: half of the power is exploited for the ZS and zero-field imaging, the other half for the MOT beams.

During the MOT loading, the ZS single pass AOM (5) is set to about $-100\,MHz$ and injected into the ZS fiber (6). In front of the fiber, a home-made shutter composed by two blades spaced by about $100\,\mu m$ is placed into the focus of a cylindrical telescope. In case the ZS AOM is set to $-125\,MHz$, the beam is instead coupled to the zero field imaging fiber (8). Spurious light injected into the ZS fiber during the imaging routine is stopped by the blade shutter. The imaging light is brought onto a small breadboard placed above the optical table and not shown in Fig. 3.5. Here an AOM in double pass allows frequency tuning of the imaging light.
The MOT light is simply split in the three separate beams by means of two PBS, indicated as (9) and (10) in Fig. 3.5.

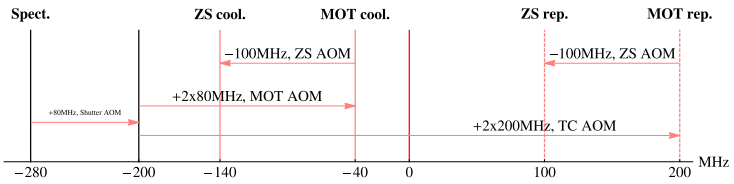

Figure 3.6: Schematic view of the different frequency detunings exploited for D2 laser cooling. The D1 scheme differs only for the value of the spectroscopy AOM frequency, set to $2 \times 100\,MHz$. This value allows to tune the D1 cooling and repumper frequencies on the blue side of the resonance, as required by the gray molasses technique [93].

[3]This issue only pertains to the new generation of Toptica chips at $670\,nm$, and it is likely related to water condensation onto the chip surface when the diode is not powered.
[4]The interlock setup is based on an ARDUINO platform.

The overall AOM frequency scheme relative to the Li optical setup is shown in Fig. 3.6. The D1 and D2 laser lights are frequency locked by means of a modulation transfer spectroscopy (MTS) scheme. This technique exploits a standard saturated absorption setup, where a modulation is added to one of the two counter-propagating beams. The modulation introduces two frequency sidebands around the carrier frequency, that owing to the interaction of the light with the atomic sample within the spectroscopic cell are transferred from one beam to the other (four-wave mixing -FWM- process). The two sidebands create a beat signal on a probe photodetector that is an odd function of the detuning between carrier and resonance frequencies. As a consequence, this technique provides a dispersion signal that has a zero crossing in correspondence of the matched resonance, featuring a slope that depends on the resonance linewidth.
MTS is a well established technique and holds on textbook theory: I refer to Ref. [94] for an extended review on the MTS and FWM process.

3.2.2 Locking scheme and design of the spectroscopy cell

Figure 3.7(a) shows a sketch of the apparatus MTS optical setup: a PBS (1) at the fiber output produces the probe and pump beams, respectively; an electro-optic modulator (EOM) is introduced within the pump path (2) and phase modulates the light at 12.5 MHz. The pump and the probe beam overlap within the spectroscopy cell, where effused Li atoms transfer the frequency modulation to the probe light. Pump and probe beams are characterized by a $1/e$ waist of $\sim 1mm$, and a power of $\sim 2mW$ and $\sim 1mW$, respectively.
The feedback signal sent to the master laser is processed by a FPGA-based heterodyning and PID electronics [5].
In figure 3.7(b) I show an example of the D2 sub-Doppler spectroscopy signal that I could obtain with this setup (or a detailed overview of D1 and D2 spectroscopy signals see, e.g., Ref. [82]).
Along the pump and probe common path, a double-pass AOM (3) operating at $+2 \times 140\ MHz$ ($+2 \times 100\ MHz$) sets the frequency detuning of the D2 (D1) master laser with respect to the atomic resonance, see again Fig. 3.6.

[5] DigiLock 110 from Toptica

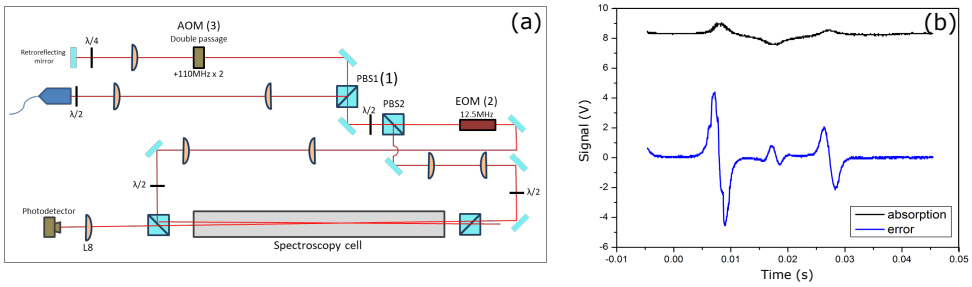

Figure 3.7: (a): Optical setup for laser locking. The scheme is analogous for the D2 and D1 laser lights, the only difference being the AOM frequency. (b): saturated absorption signal (black) and the MTS signal (blue).

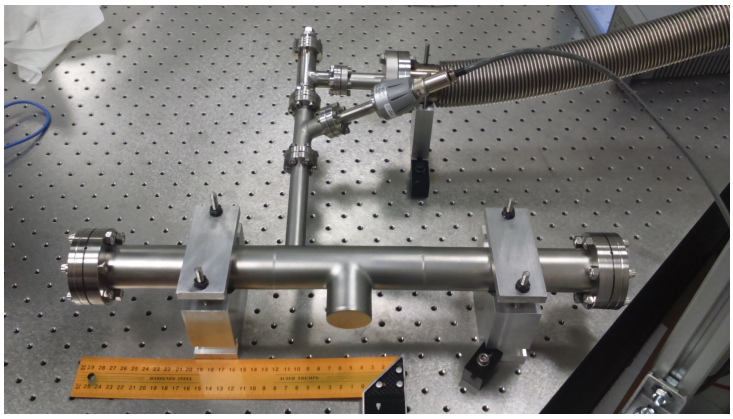

Figure 3.8: Spectroscopy vacuum cell. In photo it is visible the long flexible tube which connects the cell to the pre-pumping system.

The custom spectroscopy cell that I designed[6] is shown in Fig. 3.8. It is composed by a SS tube, ended on both sides with CF40 uncoated standard Kodial viewports[7]. A reservoir is welded to the main body of the cell and contains the Li sample; an additional CF16 flanged arm protruding upwards connects a pressure measuring gauge[8] and an all-metal angle valve. The reservoir is heated up by a Mibend metal heating ring.

In order to fill the Li into the reservoir avoiding the rapid oxidation of the sample, I inflated the cell with a continuous flux of Ar. The overpressure

[6]Manufactured by the company Mori Meccanica.

[7]Borosilicate glass. The viewports are not installed at the Brewster angle.

[8]Pirani capacitance diaphragm gauge, from Varian Technologies. It is a rough pressure gauge able to measure from ambient pressure to $10^{-4}\ mBar$.

of Ar reduces the interaction of Li with air, allowing to safely brake the glass vial containing the solid Li and to fast insert the Li into the reservoir. After this step I quickly connected the system both to a leak-valve and to a pre-pumping system by means of a tee vacuum junction. The leak-valve[9] serves to introduce a controlled amount of Ar within the cell. I activated the pre-pumps and removed all residual air within the cell, reaching the pressure of $\sim 10^{-7}$mBar; afterwards I slowly released Ar inside, without overloading the pumps, and let the Li evaporate within the cell. With a preliminary optical setup, I monitored the quality of the signal as a function of the Ar pressure and of the reservoir temperature. The optimal signal was recorded at an Ar pressure of $\sim 10^{-1}$mBar, and at a reservoir temperature of $\sim$200°.
The Ar pressure reduces the collisional broadening of the spectroscopy line by hindering Li-Li collision events. Furthermore, it reduces interactions between the Li atoms and the cold inner surfaces of the cell, thus avoiding both a loss of lithium due to condensation and the coating of the viewports. The viewports are heated up at $\sim$80° by Miband heaters to further reduce the coating process.

3.3 Chromium laser system

Our 425 nm laser setup is based on the scheme illustrated in Fig. 3.9. The blue 425nm light is generated from a 850nm laser source by means of a home-made frequency doubling stage. The breadboard dedicated to the source setup also hosts the frequency locking system.

Since we wanted our setup to be exploitable for manipulating both the bosonic and the fermionic Cr isotopes. To this end, the main source beam is immediately split into a cooling light plus the two repumper lights R1 and R2. The repumpers frequencies are set by a system of double pass AOMs which can be eventually disabled when working with the bosonic isotope.
The cooling and repumper beams are then recombined onto a PBS, and from here on follow the same path. Here, the light is split into transverse cooling (TC), MOT and ZS beams. The lights are brought to the vacuum table by means of PM fibers.
The absorption imaging light is collected from the TC beam directly on the vacuum table.

[9] Agilent Technologies.

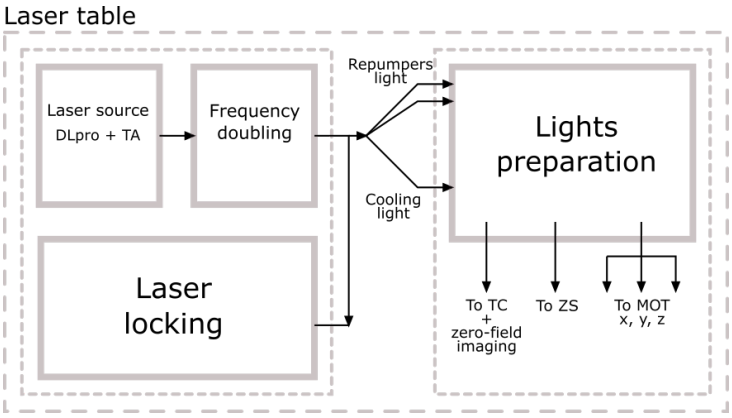

Figure 3.9: Block scheme of our 425 nm laser light optical setup.

A more detailed description of each building block of the Cr optical setup is discussed here in the following.

3.3.1 Blue laser source and lights preparation

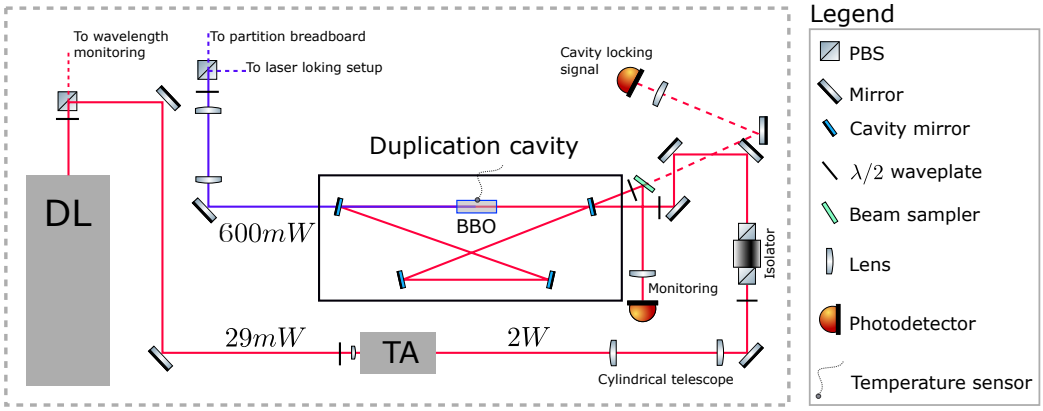

Figure 3.10: Master source setup for 425 nm laser light.

The main source of blue light in the experiment is provided by a home-made optical setup. As shown in Fig. 3.10, this is composed by a master diode laser at 850 nm, a TA system, and a frequency doubling cavity, both home-made.
The master source is a commercial Toptica DL yielding an output power of

$\sim 35\,mW$. A first PBS selects $28.5mW$ to be injected into the TA system. The remaining optical power is exploited for frequency monitoring through a wavemeter.
The TA system is composed by a TA chip, fixed a home-made Cu support that is housed within an Al case. A half-inch collimator lens is placed at the TA input. Typically, the TA is operated at $4.6\,A$ at a constant temperature[10] of $\sim 30°$, and it yields an output power of $\sim 2\,W$. The outgoing beam is strongly astigmatic, with a fast divergence on the horizontal plane. A Schäfter-Kirchhoff collimator, installed at the TA support output, collimates the beam on the horizontal axis. A cylindrical telescope, the first lens of which is hold within a fine-tuning (x, y) kinetic holder, collimates the vertical axis and adjusts the beam aspect ratio to about 1. A $> 38\,dB$ isolator[11] is placed after the cylindrical telescope to protect the TA from backward reflections.
The beam is then directly injected into the cavity. The relative distance between the cavity input and TA output has turned out to be crucial for an optimal cavity mode matching: this is due to the strong mismatch of the amplified beam with respect to a TEM00 mode, and to its rapid evolution in space. A previously adopted solution included a high-power PM fiber that filtered the TA output beam. Nonetheless, the same matching problem was there affecting the fiber coupling efficiency, and the total power loss turned out to be less advantageous than the direct injection of the beam into the cavity.
The cavity has a bow-tie configuration, where the infrared running wave propagates within a BBO (barium borate) crystal and it undergoes a second harmonic generation process. This yield a $425\,nm$ output beam with an overall typical conversion efficiency of 40%, corresponding to $\sim 600\,mW$ of blue light power.
The cavity is locked with a Pound-Drever-Hall (PDH) technique, by applying a $25\,MHz$ modulation to the laser master current. The feedback signal is sent to the voltage-control of a piezoelectric crystal installed behind one of the cavity mirror holders.
The overall Cr laser source was designed and implemented in parallel to my work within the laboratory. Despite some modification to the design added so far, I refer to the works [95, 96] for a thorough description of the doubling

[10] Thorlabs, laser-diode/temperature controller ITC4005.
[11] Linos, Fi-850-5LPVC.

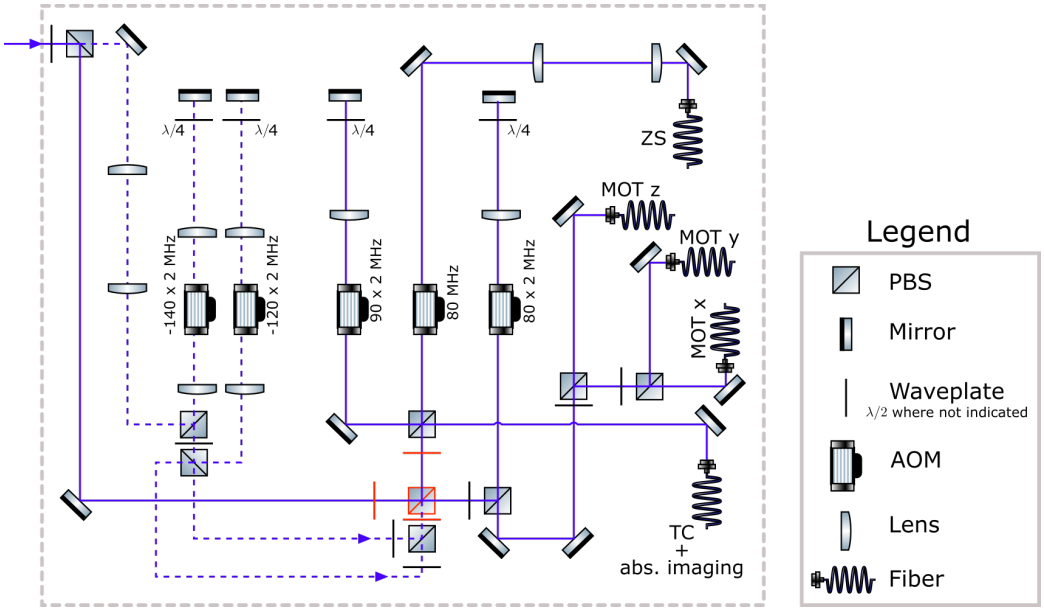

Figure 3.11: Optical scheme exploited for ^{52}Cr and ^{53}Cr laser cooling. The R1 and R2 repumper paths are indicated by dashed lines.

cavity and of the TA setup.

The cavity output beam is directly sent to an adjacent breadboard, where it is split into TC, MOT and ZS lights as shown in Fig. 3.11.
The repumpers beam path is indicated by dashed lines and consists of two double pass AOMs in a cascade configuration: the first $-140 \times 2\,MHz$ frequency shift sets the frequency of the R1 repumper; a portion of the obtained light undergoes an additional shift of $-120 \times 2\,MHz$ to reach the frequency of the R2 transition. This method avoids the need of high operating frequency AOMs, and it minimizes power losses.
The two repumper plus cooling lights recombine on the PBS indicated in red in Fig. 3.11. The waveplates system also indicated in red is set in a 50-50 power partition configuration. In this way, the three lights maintain the same relative power ratio all over the following paths and feature the same polarization.
TC and MOT lights frequencies are set by a double pass AOM, while the ZS light frequency is set by a single pass AOM. The original beam waist at the setup input is such to guarantee a good diffraction efficiency for a 80 MHz AOM (TC, MOT, ZS). Further beam shaping is needed on the repumpers

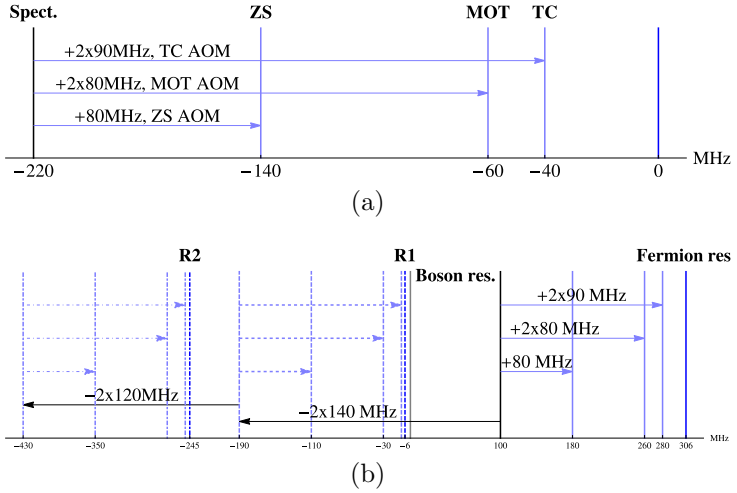

Figure 3.12: Schematic view of the frequency detunings for ^{52}Cr (a) and ^{53}Cr (b). Laser locking frequencies differ for the two isotopes (black lines). Arrows show the AOM frequency shifts exploited to prepare ZS, TC and MOT lights.

path, where the exploited AOMs are 110 MHz- and 100 MHz-centered (R1 and R2, respectively).

The overall frequency shifts schemes implemented for ^{52}Cr and ^{53}Cr are sketched in Fig. 3.12(a) and 3.12(b), respectively: cooling frequencies are indicated by solid lines, while R1 and the R2 repumper frequencies are indicated by dashed and dot-dashed lines, respectively. The locking point of the laser light (black solid lines) depends on the isotope. Two independent AOMs are indeed used within the locking setup exploited for ^{52}Cr and ^{53}Cr, as further detailed in the next section.

3.3.2 Blue light laser locking

The locking system of the blue light (Fig. 3.13) is very similar to the one applied to the Li laser system: also in this case we make use of an MTS scheme, where an EOM generates a 12.5 MHz modulation frequency on the pump light. Also in this case the error signal elaborated by a DigiLock 110 by Toptica.
The frequency locking point of the laser light with respect to the spectroscopy signal is set by tuning the frequency of the AOM placed along the common path of the pump and probe beams. We apply two different AOM schemes

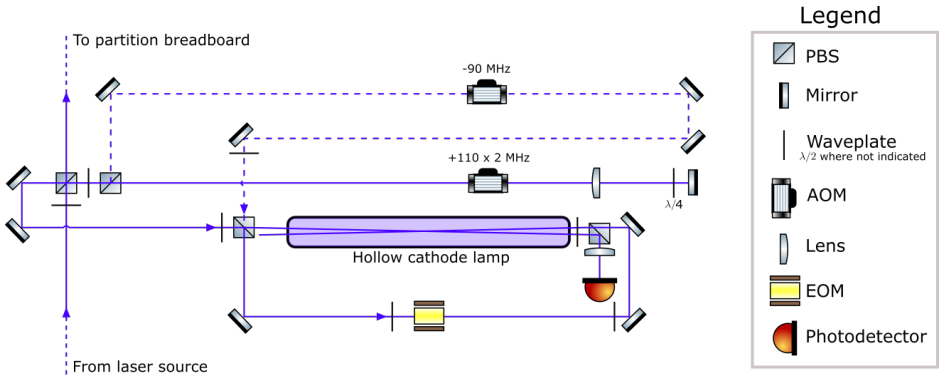

Figure 3.13: Blue laser light locking scheme. The single pass AOM exploited for the fermion is indicated by a dashed line.

for the boson and the fermion: the boson locking point is set $-2 \times 95\, MHz$ away from the boson atomic resonance; a single-pass AOM sets instead the fermion locking point at $+90\, MHz$ from the same reference (see again Fig. 3.12(a) and (b)).

Owing to the very high temperature required by Cr to sublimate, it is not possible to exploit in this case a home/madespectroscopy cell based on a heated reservoir. We use instead a commertial hollow cathode lamp (HCL)[12]. The lamp is shown in Fig. 3.14: it consists of a vacuum tight glass cell, where a feedthrough enables the supply of a system composed by a central cathode and two lateral anodes; cathode and anodes are placed in line and have a ring shape to enable the axial propagation of the laser light. The cathode is coated with a thick Cr layer, while the glass is filled with Ar. When a voltage is applied to the poles, the Ar get ionized, and the heavy ions accelerate towards the cathode, where they impact releasing Cr atoms and ions from the coating. A Cr plasma is thus formed around the cathode, with a density and distribution which depend on the applied voltage. In our case, we work at an intermediate voltage corresponding to $\sim 15\, mA$. A fraction of the plasma is composed by Cr atoms in their ground state that allow a $425 nm$ spectroscopy signal lo be detected through the standard MTS method. The signal is quite weak, and it requires an active filter stage at the input of the DigiLock electronics for a good locking stability.

[12]Madatec.

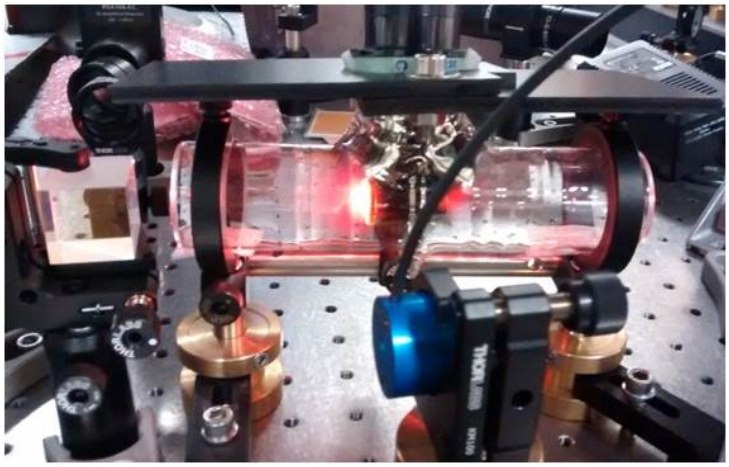

Figure 3.14: Hollow cathode lamp.

3.3.3 Red repumpers locking system

As illustrated in Sec. 3.1, we make use of two red laser lights to address the repumper transitions $|D_3\rangle \rightarrow |P_3\rangle$ and $|D_4\rangle \rightarrow |P_3\rangle$. These additional lights are provided by two DL Pro Toptica lasers operating at $654\,nm$ and $663\,nm$, respectively. To frequency lock the lasers, we first tested an FMT scheme on the hollow cathode lamp. Unfortunately, due to the very wide spectrum of populated high energy atomic and ionic states, we could not observe any spectroscopy signal within this spectral region.
As an alternative, we decided to lock the two lights on the Li spectroscopy reference by means of a transverse cavity scheme. The method relies on the locking of a primary cavity mode to a frequency reference, and the locking of the laser frequencies f_i to secondary cavity modes at a distance which is a multiple of the cavity free spectral range. The relative proximity of the Li spectroscopy reference to the two red repumpers frequencies on the order of $1\,THz$ scale, justifies the use of a standard (non-ULE) resonator as our transfer cavity.

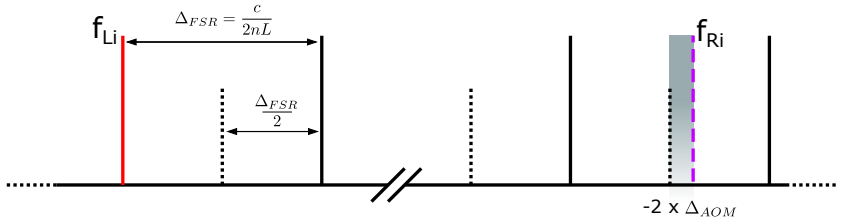

Figure 3.15: Confocal transfer cavity scheme. One odd cavity mode (red line) is locked to the reference frequency; the repumper f_{Ri} (dashed line) is locked to a secondary cavity mode. The mismatch between f_{Ri} and next cavity mode is compensated by a double pass AOM. Odd (even) modes are indicated by solid (dotted) lines.

We exploit a single transfer cavity to lock both 654 nm and 663 nm lights. The cavity is a commercial Fabry-Pérot (FP) resonator[13] of length $L = 5\ cm$, with free spectral range $\Delta_{FSR}/2 = c/4nL \simeq 1.5\,GHz$, being n the medium refractive index. The resonator features a resonance full-width-half-maximum (FWHM) of 6.5(6) MHz, corresponding to a cavity finesse of 230(20). The cavity structure is realized in Invar, a Fe-Ni alloy with very low thermal expansion coefficient $\alpha \simeq 10^{-6}\ K^{-1}$.
The cavity is in confocal configuration, for which all modes with same parity are degenerate. The Li reference frequency is locked to the odd mode laying close to the zero offset voltage settings for the cavity piezoelectric crystal; the f_{654} and f_{663} resonance frequencies are then experimentally found close to two even cavity resonances, as sketched in Fig. 3.15. For each laser, we compensate for the relatively small frequency mismatch between f_i and the selected mode with a double pass AOM. The relative radio-frequency shifts correspond to $-2 \times 210(3)\ MHz$ and $-2 \times 216(2)\ MHz$ for the 663 nm and 654 nm laser lights respectively.

The cavity modes stability is mainly affected by thermal induced deformations of the cavity optical elements. A shift of the Li reference locking position is indeed observed on a daily timescale. Such a drift corresponds to fractions of the cavity free spectral range, and it is easily compensated by tuning the piezo offset voltage. The quality of the locking stability of the red repumpers is quantified in a jitter of $\sim 0.6 MHz$ on the short timescale. This value is comparable with the spectral linewidth of the DL laser light, suggesting this as the main limiting factor to the locking stability.

Fig. 3.16 shows the detailed locking optical setup for the red repumpers. The cavity is locked via a PDH scheme to a pickup beam from the D2 Li

[13] Thorlabs, model SA200.

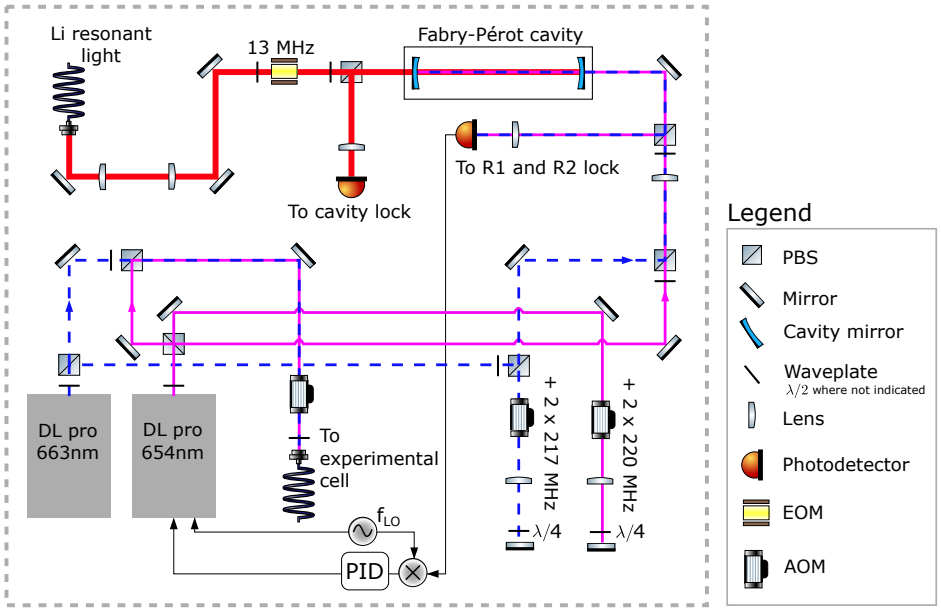

Figure 3.16: Transfer cavity based locking scheme for 654 nm and 663 nm repumper laser lights.

laser ($\sim 1\,mW$) brought to the breadboard by a PM fiber. An EOM introduces a 12.5 MHz modulation on the Li light; a photodetector monitors the reflection from the FB, and sends the beat signal to a Digilock module which process the error signal.
The repumpers locking beams ($\sim 1\,mW$) are collected at the output of both laser sources and injected into the FB from the opposite direction. To generate the error signals[14] we modulate the lasers current at the frequencies f_{LO}^{654} and f_{LO}^{663}. We experimentally adjusted the two frequencies at 9.6 and 4.1MHz respectively in order to record the beat signal of both retro-reflected lights on the same photodetector without cross interferences. Two PID locking loops[15] correct the grating piezo voltage.

[14]Mini-Circuit mixer, model ZAD-6+.
[15]Stanford Research Systems, model SIM960 Analog PID Controller.

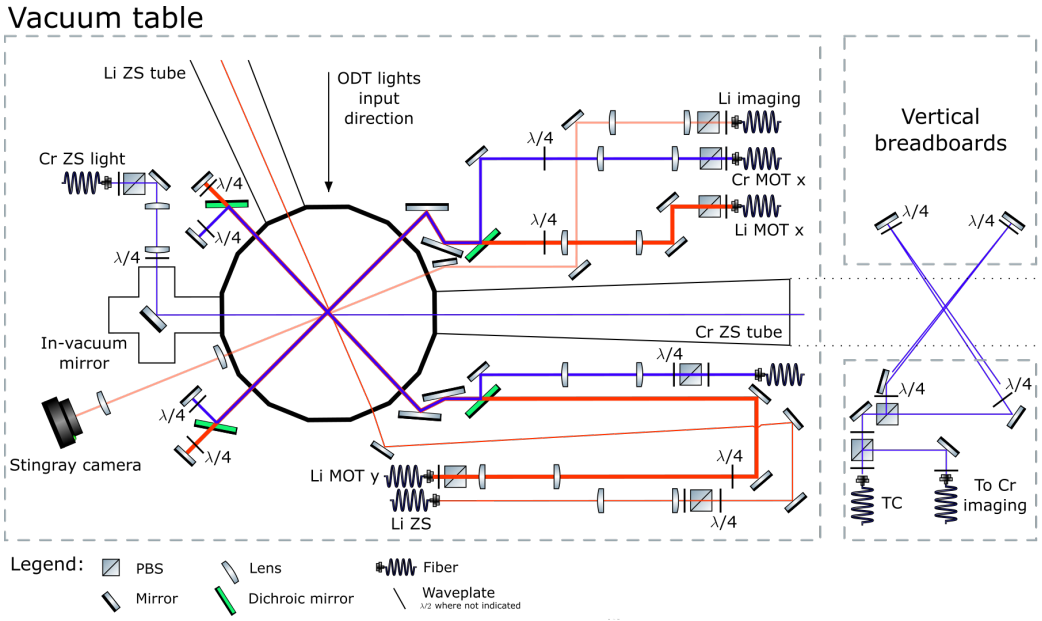

Figure 3.17: Optical setup implemented around the experimental cell for simultaneous loading of Cr and Li MOTs. Cr (Li) beam paths are indicated in blue (red). The vertical MOT beams and the Cr imaging beam are not reported for sake of simplicity. The Li absorption imaging (light red) path is also shown.

3.4 MOT and imaging optical setup

As already anticipated in Sec. 3.2 and Sec. 3.3, all Cr and Li ZS, MOT and absorption imaging lights are brought onto the vacuum table from the dedicated laser table by means of optical fibers. Here they are properly shaped and aligned on the experimental cell as exemplified in Fig. 3.17. Our MOT beams are composed by three retro-reflected independent beams for both atomic species. In order to simultaneously address the fine tuning of the two species MOT positions, while minimizing at the same time the optical setup, we make use of dichroic mirrors to overlap the Li and Cr MOT laser beams both along the forward and backward paths. This solution also optimizes the polarization ellipticity of the retro-reflected beams by making use of monochromatic waveplates, acting separately on the Cr and Li lights, see Fig. 3.17. All optics have a $2\,in$ size.
The MOT vertical path is not reported in figure for sake of simplicity. It is implemented on a $20 \times 45\,cm$ breadboards held by an Al frame above the

experimental cell. Here the output of both the $425\,nm$ and $671\,nm$ fibers are recombined by a dichroic mirror, and then shined onto the big re-entrant top window glass with a single off-plain oriented mirror. On the backward path we make use of a single $1\,in$ mirror plus a broad wavelength waveplate.
Our Li MOT fiber collimators[16] yield an output beam waist of $\sim 1\,mm$, a 1:6 telescope magnifies the beams on all three axes. The beam power imbalance is $\sim 50-50$ on the horizontal plane, with $\sim 30\,mW$ of cooling and $\sim 20\,mW$ of repumper light on each axis. Along the vertical axis we exploit $\sim 15\,mW$ for each frequency.
The Cr MOT fibers collimators[17] yield instead a $\sim 2.6mm$ beam waist, which is magnified by a 1:2 telescope on each axis. The in-plane beams have a total power of $\sim 4\,mW$, while the vertical beam has a power of $\sim 6\,mW$.

Fig. 3.17 also shows the Li and Cr ZS laser beam paths; the Li ZS beam waist is magnified up to $\sim 5\,mm$ by a 1:3 telescope, which is slightly uncollimated in order to focus the beam on the oven nozzle. The cooling and repumper intensity ratio is $3:2$ here also, while the maximum total power is set by the waveplate plus cube system at the fiber output and its optimal value depends on the MOT gradient, as it will be discussed in Ch. 4.
The Cr ZS beam is magnified and collimated by a 1:2 telescope, yielding again a beam waist of $\sim 5\,mm$. The beam power is here $\sim 100\,mW$.

Two breadboards vertically placed at the sides of the Cr oven chamber host the TC setup. A fiber brings the light on one of the two breadboards, where it is split in two paths and shined on the two 90° windows of the cross already described in Sec. 2.1.1. The beams are then retro-reflected on the opposite side.

Finally, Fig. 3.17 shows also the absorption imaging path (light red) that we use to image our Li clouds. The light is collimated on a Stingray camera after a 2:1 demagnification. The beam powers exploited here are $\sim 2\,mW$, with a waist of $\sim 2\,cm$ on the cloud. The same Stingray camera is also used for in-situ fluorescence imaging.
The Cr absorption imaging setup is instead implemented on the top breadboard together with the MOT z axis beam: the light is picked up from the TC main beam on the vertical breadboard and sent to the top breadboard via a fiber. The light is then collimated on an Andor camera placed at the bottom of the experimental chamber, positioned on the vacuum table.

[16] Schäfter-Kirchhoff, 60CF-4-M11-33.
[17] Schäfter-Kirchhoff, 60CF-4-M20-.

3.5 Optical dipole trap for Cr and Li atoms

Besides the optical system described in the previous sections, required for the laser cooling of the two species, our apparatus is also equipped with a high power optical dipole trap, which will serve to collect the two clouds delivered by the double-species MOT, and to implement the successive evaporative and sympathetic cooling stages. Indeed, our strategy to reach simultaneous quantum degeneracy of the Cr-Li mixture relies on an all-optical approach which turned out being very successful already, both for homonuclear Li spin mixtures [93, 97, 98], as well as for these latter in combination with another alkali species, in particular the ^{40}K isotope [99, 100]. In the specific case of our Li-Cr mixture, we indeed plan to exploit the easy to handle ^{6}Li to cool down to degeneracy the fermionic ^{53}Cr by means of sympathetic cooling. To this end, the ODT potential must be such to guarantee a large overlap of the Li and Cr samples, necessary condition for an efficient thermalization. A good mode matching of the two species density distributions is also desirable in view of a flexible experimental investigation of the mixture, under a full control of the relative population imbalance. Finally and very importantly, the efficiency of the sympathetic cooling process requires the resulting trapping potential to be deeper for the Cr atoms than for the Li ones. To this end, as discussed in the following, we designed and implemented a bichromatic optical trap.

3.5.1 Optical dipole trap main designing features

In order to define the suitable ODT design, we first estimated the dipole potential experienced by Li and Cr atoms in their hyperfine ground state in the presence of 1070 nm light, for which high power, relatively inexpensive laser sources are available. For an atom in the electronic state $|n, J, m_J\rangle$, the dipole potential is generally defined by

$$U_{n,m_J}(\mathbf{r}) = -3\pi c^2 I(\mathbf{r}) \sum_i \frac{sign(\omega_{n\to i}\Gamma_{n,m_{J_n}\to i,m_{J_i}})}{\omega^2_{n\to i}(\omega^2_{n\to i} - \omega^2_L)} \tag{3.1}$$

where $\hbar\omega_{n\to i}$ is the energy (positive or negative) associated with the addressed transition, and $\hbar\Gamma_{n,m_{J_n}\to i,m_{J_i}}$ the relative coupling strength. The latter depends on the ground state multiplicity and on the excited sublevel m_{J_i}-dependent Clebsh-Gordan coefficient. $\hbar\omega_L$ stems for the laser photon energy, and $I(\mathbf{r})$ for the laser intensity at the atom position. A full derivation of Eq. (3.1) can be found in Ref. [4, 101].

Accounting for the whole rather complex level structure of Cr atoms, we obtained that 1070 nm light yields a trap about 2.5 times deeper for Li than for Cr atoms. For this reason, we decided to realize our ODT employing a combination of two different laser sources, at 1070 nm and 532 nm, respectively. Indeed, the latter wavelength is anti-trapping for Li while strongly confining Cr atoms. As a result, upon superimposing the two beams and by properly setting their relative intensities, we can controllably adjust the trapping potentials of the two species. In particular, we opted for a design of our bichromatic trap in which the two beams feature the same beam waist w_0 on the atomic clouds. Although the final dimension of the Gaussian beams will be optimized by monitoring the capture efficiency of the atomic samples, initially we designed our optical setup such to guarantee for the two laser sources a focused beam waist value which is a good compromise between two distinct effects: astigmatism on the one side, and axial confinement on the other.

Astigmatism has the detrimental effect of reducing both the radial and axial effective atoms confinement. Although being controllable to some extent by carefully shaping and aligning the optical path, astigmatism is difficult to eliminate especially when high-power beam waists of less than $\sim 25\mu$m are considered. The impact of such an undesired effect can be strongly reduced by increasing the beam Rayleigh length $z_R = \pi w_0^2/\lambda$, i.e. w_0. Increasing w_0 has also the advantage of enlarging the trapping volume, which scales as $\sim w_0^2 z_R \sim w_0^4/\lambda$.

On the other hand, too large w_0 values must be avoided, as they can easily lead to too shallow ODT potentials: this can be straightforwardly understood recalling that the peak intensity of a Gaussian beam $I_0 = 2P_0/\pi w_0^2$, setting the trap depth U_0, scales linearly with the laser power P_0 and quadratically with $1/w_0$. As such, for a given maximum power delivered by the laser source, the choice of the beam waist sets a limit to the maximum initial temperature $T_i = U_0/k_B$ of the atoms that can be trapped by the ODT.

Additionally, the choice of w_0 sets also the radial and axial ODT frequencies. Approximating the Gaussian profile to a harmonic potential, it is easy to

verify that both radial and axial trap frequencies scale as $\omega_{i=z,\perp} \propto 1/w_0^2$.

Based on these considerations, we designed our optical setup to produce for both laser beams a waist of $w_0 \sim 45\,\mu m$, a value quite typical for ODTs employed both for the cooling of Li [102] and Cr [4] species. From such a beam size, combined with the maximum powers of $300W$ and $55W$ delivered by our infrared (IR) and green laser sources, respectively, we expect an overall trap depth for both species up to 1.5 μK, a value sufficiently large to guarantee an efficient storage of both Li and Cr clouds delivered by the MOT and optical molasses around 100-200 μK temperatures.

During the construction of the optical trapping setup, we also devised a simple solution to minimize the so-called thermal lensing effect. This phenomenon arises from the fact that both the substrate and coating of any optical element composing a generic setup unavoidably absorb part of the incident light, with the non-uniform intensity profile of the impinging beam acting as an inhomogeneous heat source for the material. Due to the consequent local induced deformation of its optical properties, the illuminated element acts like a lens [103,104], rendering the beam waist position (hence its actual dimension on the atoms) a time- and an intensity-dependent quantity. Such an undesired effect, rather common within high power ODT setups, is especially detrimental in the case of our bichromatic trap. Indeed, since thermal lensing effects significantly vary with the laser wavelength, they may result in an uncontrolled variation of the potential landscape experienced by Li and Cr atoms during the capture and subsequent evaporative cooling stages, significantly reducing the overall efficiency.
For the detailed characterization of thermal lensing effects on our ODT setup, and the description of the experimental strategy enabling us to cancel them out, I refer the reader to our recent paper Ref. [5], which I append as Appendix C to the thesis.

As a final remark, I also mention that while designing the ODT setup we also considered the possible issues associated with the different gravitational sag experienced by the two species. This effect cannot be neglected, as it may lead to a strong reduction of the spatial overlap of the Li and Cr clouds, especially when approaching ultralow temperatures (i.e. low trap depths). To overcome this problem, we already designed, tested and installed on the main chamber an additional pair of magnetic field coils, collinear with the Feshbach ones, that allow to controllably tune a weak magnetic gradient up to a few G/cm along the gravity direction. Owing to the different magnetic moment and mass of the two species (see again Tab. 3.2 and 3.4 in Sec. 3.1),

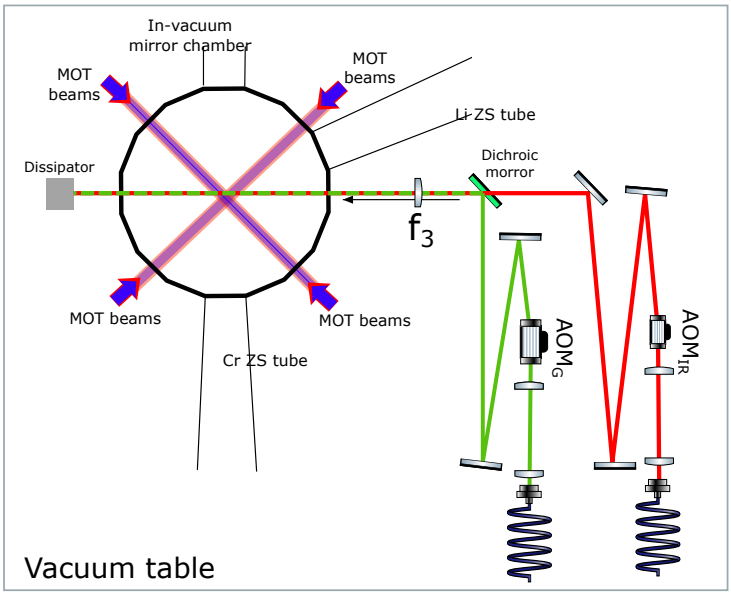

Figure 3.18: ODT optical setup. For each of the two laser beams, the optical setup is solely composed by three lenses, one AOM and reflective optics. The IR and green laser paths are indicated with red and green lines, respectively.

the resulting magnetic force will affect differently the two species, enabling to minimize their relative sag in the ODT. Pinpointing the optimum gradient to obtain the best overlap will be done in the future by monitoring the cloud barycenters, as a function of the supplied current.

3.5.2 Bichromatic ODT optical setup

In this subsection I summarize the optical setup we built to realize the bichromatic ODT. As anticipated, more details and motivation for the specific choices made in designing the apparatus can be found in Appendix C of this thesis. In light of the fact that any substrate unavoidably introduces some degree of thermal phase aberrations, our ODT setup employs as few optical elements as possible to adjust the beam powers and waists on the atomic clouds: its design (see sketch in Fig. 3.18) is solely composed by three lenses, one AOM and reflective optics, for each of the two exploited laser sources. The $1070\,nm$ light is provided by a YLR-300 multimode fiber laser module by IPG Photonics, delivering up to $300\,W$ output power, with an output beam

waist of $2.21(1)\,mm$ with negligible ellipticity. The $532\,nm$ source is instead a single-mode CW fiber laser (GLR-50, again by IGP Photonics), delivering a maximum of $55\,W$ with an output beam waist of $\sim 500\,\mu m$, again with negligible ellipticity.
A telescope de-magnifies both the IR and the green beam waists down to $550\,\mu m$ and $250\,\mu m$ respectively, in order to match the optimum size that maximizes the AOM diffraction efficiency.
The insertion of AOMs along the two beam paths allows to finely tune and stabilize the laser powers within the experimental routine by controlling the radio-frequency amplitudes. In addition, it also allows to enlarge the effective ODT trapping volume under a modulation of the AOM radio-frequency, which periodically displaces the ODT spot position in the focal plane: if the modulation is faster than the ODT radial trapping frequencies, the atoms will experience an effective trapping volume of larger dimension.

The first-order diffracted beams are recombined onto a dichroic mirror before hitting the last common lens f_3. The distance between the two AOMs and the last lens, of nominal focal length $f_3 = 250\,mm$, is carefully adjusted such that the two waists match here the required dimensions in order to create a common focus onto the atomic cloud with beam waist of $45\mu m$.

All lenses employed in our design are one inch UV fused silica elements with anti-reflection V-coating at $1064/532\,nm$. Although not featuring the same performances of Suprasil substrates, these represent a cheap and convenient option for high power applications, due to a very small refractive index temperature dependence $dn/dT = 12 \times 10^{-6}\,K^{-1}$ [105], and a low thermal expansion coefficient $\alpha = 0.5 \times 10^{-6}\,K^{-1}$ [106]. The CF 40 window of the vacuum chamber is made by a $3.3\,mm$ thick quartz substrate with custom anti-reflection coating. Finally, the $\mathrm{AOM_{IR}}$ is realized by a $31\,mm$ thick *TeO2* crystal[18], with a transverse area of $2.5 \times 1.75\,mm^2$. The $\mathrm{AOM_G}$ is realized with a crystal specifically meant for high power applications[19]. Relative to cheaper options available on the market and considered initially in our setup, such an AOM features substantially higher damage thresholds at 532 nm, and most importantly we found that it does not yield to significant thermal lensing effects for our typical working conditions.

[18] 3110-191 by Gooch&Housego
[19] 3080-294 by Gooch&Housego.

Chapter 4

Realization of a cold lithium-chromium mixture

I present in this chapter the first experimental results attained with the apparatus that I designed and implemented during my PhD activity. These results consist in the individual and simultaneous realization of magneto-optically trapped clouds of fermionic ^{6}Li atoms and bosonic ^{52}Cr atoms.
The chapter is structured as it follows. Sec. 4.1 presents our magneto-optically trapped clouds of ^{6}Li atoms, and the first experimental implementation of gray-molasses cooling routines operating on the D1 atomic transition. Our magnetically-trapped clouds of ^{52}Cr atoms are instead presented in Sec. 4.2. Here, I also report on the characterization of the spectroscopic lines associated with the $|D_3\rangle \rightarrow |P_3\rangle$ and $|D_4\rangle \rightarrow |P_3\rangle$ atomic repumper transitions. By addressing these transitions, we were able to investigate magnetically trapped clouds of Cr atoms occupying $|D_3\rangle$ and $|D_4\rangle$ metastable states. Finally, I present in Sec. 4.3 the first experimental realization of double-species MOTs of Cr and Li atoms, achieved during the very last months of my PhD activity.

4.1 Cold clouds of ^{6}Li atoms

I provide in this section an overview of the main features characterizing our magneto-optically trapped clouds of ^{6}Li atoms, discussing the iterative optimization work performed in order to maximize the MOT loading efficiency. The overall loading and cooling experimental routine, operating on the D2

atomic transition, is also discussed. The temperature featured by the Li atomic cloud at the end of the loading routine is further reduced by means of gray-molasses cooling techniques, operating on the D1 atomic transition: the present section also reports on the first experimental implementation of D1 cooling routines on our experimental apparatus.

4.1.1 Magneto-optically trapped clouds of ^{6}Li atoms

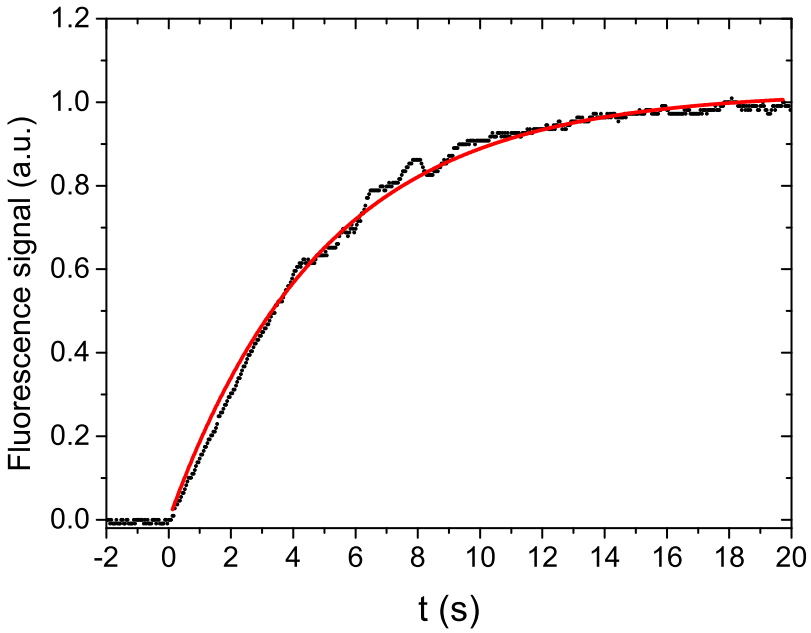

Figure 4.1: Fluorescence signal recorded on a photodetector during the loading of the Li MOT. The signal was fitted with a one-body losses loading curve (red solid line), yielding a $1/e$ loading time constant $\tau_L = 4.96(3)\,s$. Loading settings: MOT current, $35\,A$ ($17.7\,G/cm$); MOT beams power, $25\,mW$ and $17\,mW$ within the horizontal and vertical axes respectively; MOT beams detuning, $\sim -5\Gamma$; ZS current, $2\,A$; ZS beam power, $20\,mW$; ZS light detuning, $\sim -24\Gamma$.

Fig. 4.1 shows a typical example of fluorescence signal recorded on a photodetector during the loading of our Li MOT. The saturated atom number, extracted from a Gaussian fit of an *in-situ* fluorescence image of the atomic cloud within the vertical plane, corresponds to $N_\infty = 1.9(6) \times 10^{10}$. The $1/e^2$ radius of the cloud are $2.504(6)\ mm$ and $2.920(14)\ mm$ on the vertical and horizontal direction, respectively, yielding a peak density of

$n = 5.0(1.5) \times 10^{11}\ cm^{-3}$.
The observed behavior is well reproduced by a single exponential curve of the kind $N(t) = N_\infty(1 - e^{-t/\tau_L})$, which is the solution of the rate equation

$$\dot{N}(t) = +L - \frac{1}{\tau_L}N(t) \tag{4.1}$$

for a dynamics featuring a constant loading rate L and single particle losses. Under these assumptions, $N_\infty = L/\tau_L$. A fit of the signal in Fig. 4.1 (red solid line) yield a loading time constant $\tau_L = 4.96(3)\ s$, corresponding to a loading rate $L = 4 \times 10^9\ s^{-1}$.
Absorption imaging results yield a factor 50 smaller value of collected atom number, corresponding to optimum values of $N \sim 4 \times 10^8$, and peak densities of $n \sim 10^{10}\ cm^{-3}$. Such a big discrepancy is ascribed to two facts: on the one hand, the calibration of the fluorescence imaging is difficult, owing to its strong dependence upon illumination time, and beam power and detunings. On the other hand, the absorption imaging in the presence of the MOT field may underestimate significantly the atom number.

The iterative optimization work of the loading experimental settings, which allowed to attain the optimum values presented above, is discussed here in the following.

As explained in chapter 2, the radial magnetic field profiles generated by the MOT and ZS coils are designed to smoothly merge at the edge of the experimental chamber, yielding a continuously decreasing field profile. The optimum merging configuration was theoretically predicted for a MOT current of 37 A and a ZS current of 2 A, for the specific case of a quadrupole gradient of 20 G/cm. In order to test the validity of this prediction, and to determine the optimum settings configuration at each quadrupole gradient of interest, we investigated the MOT collection efficiency as a function of the MOT and ZS coils current. Figure 4.2 shows typical examples of curves that we recorded to this end. In particular, Fig. 4.2(a) shows the behavior of collected atom number (red points) and peak density (black circles) as a function of the MOT gradient at the fixed ZS current of 2 A. For each data-point, the detuning of both cooling and repumper laser lights was adjusted in order to maximize the loading rate, see as an example Fig. 4.3. In agreement with the designing settings, the atom number saturates around a gradient of 17.7 G/cm, corresponding to a MOT current of 35 A. The peak density instead keeps increasing as the gradient shrinks the cloud. In a spec-

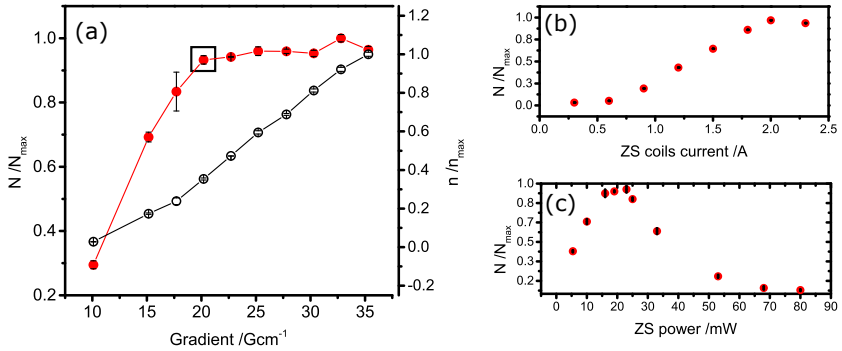

Figure 4.2: The ZS and MOT field profile merging was optimized through an iterative investigation of the MOT collection efficiency as a function of MOT and ZS coils current. (a): Collected atom number after 10 s loading (red dots) and relative peak density (black circles) as a function of the MOT gradient, at the fixed ZS coils current of 2 A. (b): Collected atom number after 10 s loading at a MOT gradient of 17.7 G/cm (corresponding to square symbol in (a)) as a function of the ZS coils current. (c): Atom number as a function of total ZS beam power, for the optimum conditions of MOT gradient and ZS current of 17.7 G/cm and 2 A, respectively.

ular way, we could check that the maximum MOT atom number in presence of a gradient of 17.7 G/cm was obtained with a ZS current around 2 A, see Fig 4.2(b).

The MOT loading efficiency was further monitored as a function of the ZS beam power, for each magnetic field gradient. Fig. 4.2(c) shows as an example the MOT atom number as a function of the ZS light power, again for a MOT and ZS coils current of 35 A and 2 A, respectively. Under these conditions, we obtained a clear maximum at relatively low laser powers, around 20 mW. This value comprises both cooling and repumper laser powers, with a 50-50 relative ratio. The fast decrease of the collected atom number at higher laser intensities can be ascribed to the perturbation induced on the MOT cloud by the ZS beam light. This conclusion is further supported by the direct observation of a spatial displacement of the MOT cloud out of the quadrupole position, of the order of few mm, in presence of the ZS light. The displacement is clearly enhanced at increased ZS beam intensities, eventually leading to the complete fade-out of the cloud. This detrimental effect, observed at all the investigated MOT gradients up to $\sim 30\, G/cm$, is partially mitigated by aligning the ZS beam close to the edge of the MOT capture volume, and by further detune the ZS light with respect to the predicted optimal value of $-18\,\Gamma$, see Sec. 2.2 in Ch. 2. The optimum ZS detuning

is found to fall within the range $-26\,\Gamma$ and $-19\,\Gamma$ for all MOT gradients between $\sim 20\,G/cm$ and $\sim 30\,G/cm$. The data shown in Fig. 4.2 were recorded at a ZS detuning of $-24\,\Gamma$.

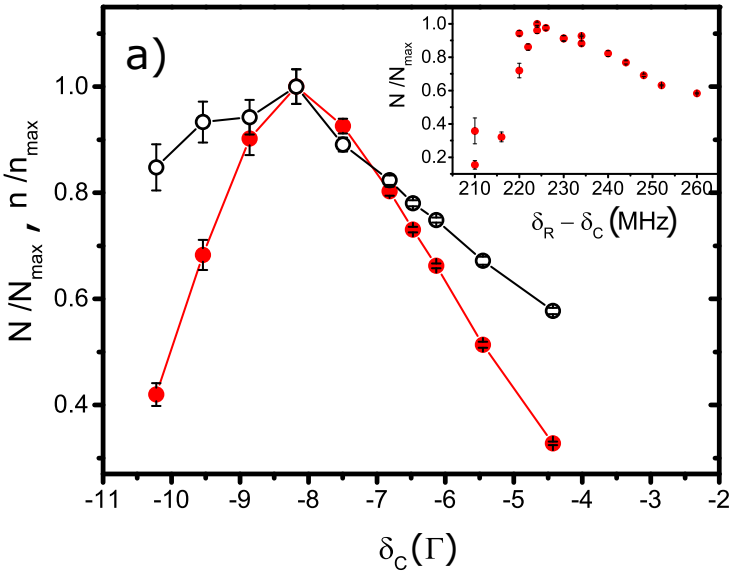

Figure 4.3: MOT atom number (red dots) and the peak density (black circles) as a function of the MOT beams detuning, at a MOT gradient of $27.8\,G/cm$, recorded after $10\,s$ loading. Here, the ZS current and beam power were $2.5\,A$ and of $35\,mW$, respectively.

Finally, I report in Fig. 4.3 a typical curve obtained by investigating the MOT atom number (red dots) and the peak density (black circles) as a function of the MOT cooling light detuning δ_C with a $10\,s$ loading time. The MOT gradient was here $27.8\,G/cm$, corresponding to a MOT coils current of $55\,A$; the ZS coils current and laser power were optimized to $2.5\,A$ and $40\,mW$, respectively. The repumper and cooling relative detuning was here $\delta_R - \delta_C = 230\,MHz$. The data indicates a clear maximum for both atoms number and peak density around $\delta_C = -8\,\Gamma$. The inset shows the behavior of the MOT atom number as a function of the relative detuning $\delta_R - \delta_C$, with δ_C fixed to the optimum value of $-8\,\Gamma$. In agreement with the hyper-fine energy splitting within the D2 manifold of the Li atom, see again Fig. 3.2, the optimum loading efficiency is found at a relative shift of $\delta_R - \delta_C = 225\,MHz$, corresponding to $\delta_R = -9.6\,\Gamma$.

The Li atomic cloud, obtained after the iterative optimization presented

so far, is characterized by relatively high temperatures of the order of $3\,mK$. In order to reduce this value, our loading routine proceeds with a two-step compressed MOT (CMOT) stage as exemplified by Fig. 4.4. After a typical loading time of $7\,s$, we cool and compress the MOT by decreasing the laser beam intensity of both cooling and repumper lights to less than the 90% and 20% of their initial value, respectively, while simultaneously decreasing the frequency detuning of both. The cloud is kept under these conditions for $100\,ms$. This stage enables to decrease the temperature of the cloud down to about $T = 800\mu K$ with no atom losses. At this point we operate the second CMOT stage by further reducing the laser light intensities to a few percents of the initial value, while simultaneously setting the detunings down to $\sim -2\Gamma$. At the end of this second step, we obtain typical cloud temperatures of about $T = 500\mu K$ with atom losses below the 20%.

During the first CMOT stage, we transfer the atomic cloud from the quadrupole field created by the MOT coils to the one created by the Feshbach coils in Anti-Helmholtz configuration. To this end, we ramp up the Feshbach coils current in $\sim 80\,ms$, while simultaneously decreasing to zero the MOT coils current, see upper diagram in Fig. 4.4. Owing to their smaller inductance, the quadrupole field of the Feshbach coils can be effectively switched off in much smaller timescales, of the order of hundreds of μs for all coil currents up to $55\,A$ (corresponding to $\sim 30\,G/cm$).

4.1.2 D1 gray-optical molasses on Li atomic clouds

Laser cooling theory predicts that the minimum temperature achievable in a MOT is set by to the Doppler limit, $T_D = \hbar\Gamma/2k_B$, being Γ the linewidth of the cooling transition. For the Li atom, the Doppler limit corresponds to $T_D = 140\,\mu K$.

For most of alkali atoms, sub-Doppler temperatures below T_D can be generally achieved with Sisyphus cooling in optical molasses. For Li atoms, however, the unresolved hyper-fine structure associated to the excited $P_{3/2}$ state impedes an efficient operation of Sisyphus cooling techniques on the D2 atomic transition, see again Fig. 3.2.

Nonetheless, temperatures below T_D can be achieved in Li atomic clouds through gray-molasses cooling operating on the D1 ($|S_{1/2}\rangle \rightarrow |P_{1/2}\rangle$) atomic transition. This technique, first successfully applied to the fermionic ^{6}Li isotope in 2014 [93], relies on the simultaneous action of Sisyphus cooling mechanisms and of velocity selective coherent population trapping (VSCPT)

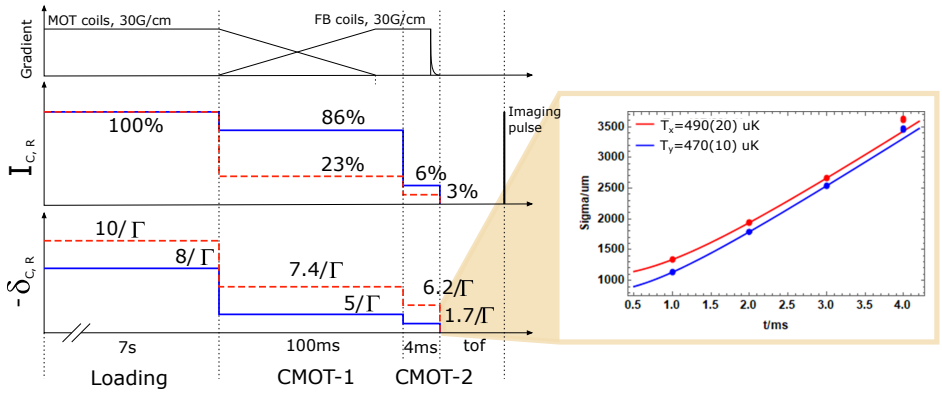

Figure 4.4: Sketch of MOT and CMOT loading experimental routine. The drop of cooling and repumper laser light intensities ($I_{C;R}$) and detunings ($\delta_{C;R}$) during the two CMOT stages is indicated. After a typical loading time of 7 s, the Li cloud is transferred from the MOT quadrupole into the Feshbach coils quadrupole (upper diagram) within a 80 ms coils currents ramp. The figure also reports an example of time-of-flight expansion measurement, taken at the end of the loading routine. The cloud size was fitted with the ballistic scaling low $\sigma_i = \sigma_{0i}\sqrt{1 + t^2 k_B T/(m\sigma_{0i}^2)}$ [107], independently for the horizontal (σ_x) and vertical (σ_y) direction, yielding an average temperature of 480(20)μK..

mechanisms [108, 109]. Sisyphus cooling is achieved by addressing the ($|F = 3/2\rangle \rightarrow |F' = 3/2\rangle$) cooling transition within the D1 manifold, with a positive frequency detuning $\delta_C > 0$. The VSCPT mechanism arises when an additional laser light simultaneously addresses the same excited state, within the ($|F = 1/2\rangle \rightarrow |F' = 3/2\rangle$) repumping transition, with a frequency detuning δ_R that approaches the Raman condition $\delta_C - \delta_R = 0$ [110], see Fig. 4.5.
D1 gray-molasses cooling is nowadays a well established technique. For a more detailed theoretical overview of the gray-molasses cooling mechanism I refer to the works in Ref. [111].

Fig. 4.6 shows the very first experimental results relative to the implementation of D1 gray molasses routines on our atomic Li cloud. These results where obtained operating a 1 ms D1 gray-molasses stage, 0.4 ms after the switch off of the quadrupole field. The initial cloud temperature was $T \sim 500\mu K$, obtained at the end of the CMOT D2 cooling routine presented in the previous section. The cooling light intensity during the D1 stage was $I_C = 2.75 I_{sat}$, while the repumper laser light was $I_R = 0.045 I_C$, along all the three MOT beams.
The final temperature of the cloud is reported in the figure (red dots) as a function of the Raman detuning $\delta = \delta_C - \delta_R$, for $\delta_C = +8\Gamma$. The data show

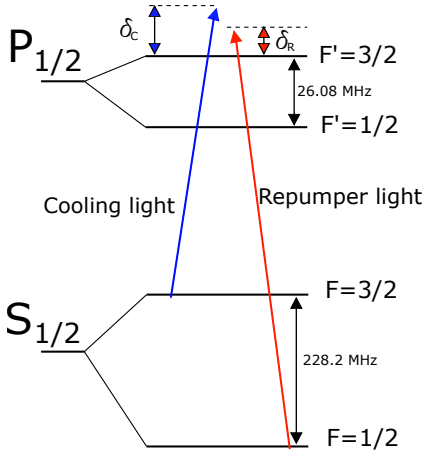

Figure 4.5: Sketch of the atomic structure on the ^{6}Li D1 manifold. The detunings of cooling and repumper lights are indicated with δ_C and δ_R, respectively. The Raman condition is fulfilled at $\delta = \delta_C - \delta_R = 0$.

an asymmetric Fano profile, which is the clear signature of the emergence of a quantum interference effect. The minimum temperature is reached very close to the Raman condition, at $\delta = -0.25\Gamma$. The plot also shows the fraction N/N_0 of atoms captured by the gray-molasses (blue dots), imaged after $1\,ms$ of time of flight. As expected, the maximum of N/N_0 is found close to the minimum temperature condition, on the negative side of the Raman detuning. In correspondence of the minimum temperature, the atomic fraction after the D1 cooling stage is around 70%, consistently with what reported in Ref. [93].

Fig. 4.7 shows the minimum temperature obtained on our Li cloud after $1\,ms$ D1 cooling stage as a function of the absolute detuning δ_C, under the same conditions of initial cloud temperature and laser light intensities as in Fig. 4.6. As shown within the insect, minimum temperatures below $75\,\mu K$ are consistently found for $\delta_c > 1.5\Gamma$. The inset shows as an example the time-of-flight evolution of the Li cloud size for $\delta_c = 2.2\Gamma$, yielding a temperature of $72(1)\,\mu K$.

Previously reported results on fermionic Li clouds [93] attest the possibility to reach a factor 2 smaller minimum temperatures, of the order of $40\,\mu K$. We attribute the non-optimum efficiency of our D1 cooling stage presented in Fig. 4.6 to the presence of residual magnetic fields and to a non-negligible fraction of incoherent laser light within the MOT laser beams

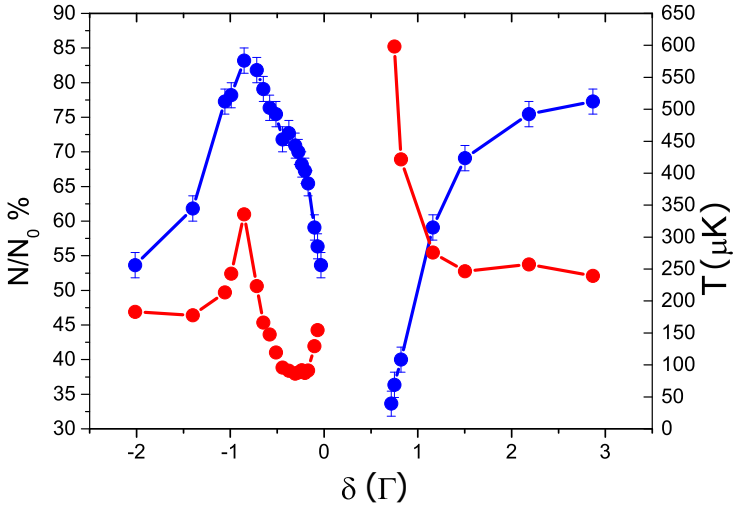

Figure 4.6: Cloud temperature (red dots) and atom number (blue dots) observed at the end of a $1ms$ D1 gray-molasses stage, applied after the two-steps compressed-MOT routine exemplified in Fig. 4.4. The cloud temperature was obtained by fitting the time-of-flight evolution of the cloud size with a ballistic scaling low [107]. The results are reported as a function of the relative detuning $\delta = \delta_C - \delta_R$, with $\delta_C = +8\Gamma$.

during the D1 cooling stage. This spurious light derives from the tapered-amplifier output fluorescence, which we observed to be partially coupled to the optical fibers of the MOT beams, see again Sec. 3.2.1 for an overview of the optical setup. Further improvement might be attained by increasing the relative frequency coherence of cooling and repumper laser lights, defined by the associated AOM radio-frequency settings. Indeed, very recently we could finally reach temperatures as low as $42(2)\ \mu K$ (not shown) in the optimum Raman configuration, by reducing the switch-off time of the quadrupole field and by optimizing the fiber coupling to drastically reduce fluorescence of the tapered amplifiers impinging on the atomic cloud.

4.2 Cold clouds of ^{52}Cr atoms

In this section I present the first characterization of our newly achieved magneto-optically trapped clouds of bosonic ^{52}Cr atoms, and discuss the iterative optimization work that we operated in order to maximize the MOT capture efficiency. The MOT loading and cooling experimental routines, operating on the $|S_3\rangle \rightarrow |P_4\rangle$ atomic transition, are also presented.

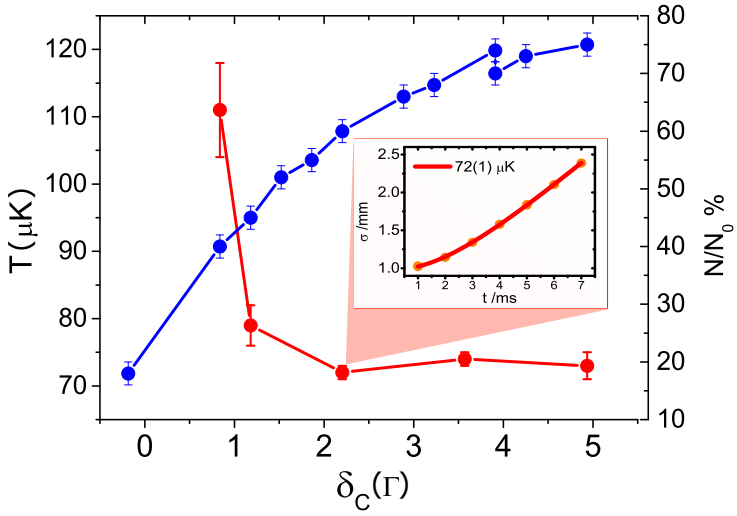

Figure 4.7: Cloud temperature (red dots) and atom number (blue dots) observed at the end of a $1\,ms$ D1 gray-molasses stage. The cloud temperature was obtained by fitting the time-of-flight evolution of the cloud size with a ballistic scaling low [107]. The results are reported as a function of the absolute detuning δ_C, with $\delta_C - \delta_R = -0.25\Gamma$.

Furthermore, I will report here on the experimental characterization of the spectral lines associated with the inter-combination repumper transitions $|D_3\rangle \rightarrow |P_3\rangle$ $(653.973\,nm)$ and $|D_4\rangle \rightarrow |P_3\rangle$ $(663.973\,nm)$, as well as on the first experimental investigation on magnetically trapped clouds of metastable D state atoms achieved within our experimental apparatus.

4.2.1 Magneto-optically trapped clouds of ^{52}Cr atoms

Fig. 4.8 shows a typical example of loading curve featured by our ^{52}Cr MOT clouds. Typical values of the saturated atom number correspond to $N \simeq 7.4 \times 10^6$, and are extracted from $1\,ms$ time-of-flight absorption images of the atomic cloud within the horizontal plane, see Sec. 3.4 for the imaging optical setup. As for the Li MOT case discussed in the previous section, a single-exponential curve is employed to fit the observed loading fluorescence signal, yielding a loading time constant $\tau_L = 0.13(1)\,s$, corresponding to a loading rate $L_D = 5.7 \times 10^7\,s^{-1}$.

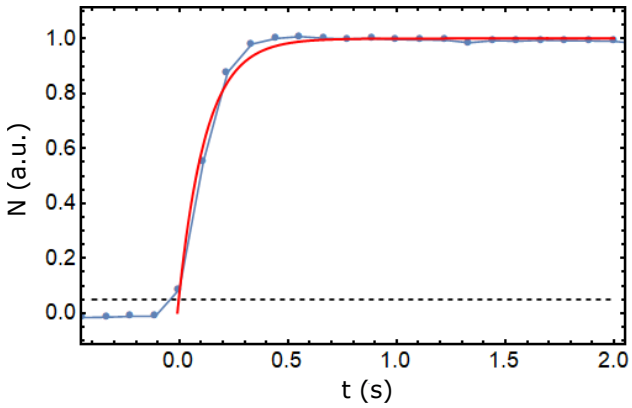

Figure 4.8: Cr MOT fluorescence signal as a function of loading time, recorded with a Thorlabs CCD camera. The curve is obtained as an average over many loading cycles recorded under the same experimental conditions. For each considered loading curve, the reference time $t = 0$ was defined by the trigger level set here to $\sim 5\%$ of the maximum observed fluorescence signal. The averaged signal was fitted with a single-exponential curve, yielding a $1/e$ time constant $\tau_L = 0.13(1)\ s$. Loading settings: MOT current, $55\,A$ ($27.8\,G/cm$); MOT beams power, $4mW$ and $2mW$ along the horizontal and vertical directions respectively; ZS current, power and laser detuning, $14\,A$, $96\,mW$, $\delta = -18.5\Gamma$, respectively; TC total beam power, $23\,mW$.

As discussed in relation to our MOT clouds of Li atoms, the optimum loading efficiency of the Cr MOT is attained with a proper combination of MOT and ZS coils currents, that optimizes the smooth connection between the two relative magnetic field profiles. Fig. 4.9 shows typical examples of datasets that we recorded in order to optimize the overall configuration of currents and light detunings, by monitoring within an iterative approach the atom number collected within the MOT after a fixed loading time of $7\ s$. In particular, the 2D plot of Fig. 4.9(a) shows the mutual dependence of the atom number on the MOT gradient and laser light detuning at a constant ZS coils current of $13\,A$. The dataset indicates that the largest atom numbers, above the 80% of the maximum recorded value, are attained for a MOT field gradient comprised between 15 and $21\,G/cm$ (corresponding to a MOT current of $\sim$ 30-38 A) with a MOT laser light detuning comprehended between -3 and -4Γ, respectively. Fig. 4.9(b) shows instead the loaded atom number under two different MOT gradients, of $16\,G/cm$ and $20\,G/cm$, respectively, as a function of the ZS coils current: although rather noisy, the measurements reveal an optimum loading efficiency for higher ZS coils currents, of the order of $15\,A$, for both investigated field gradients.

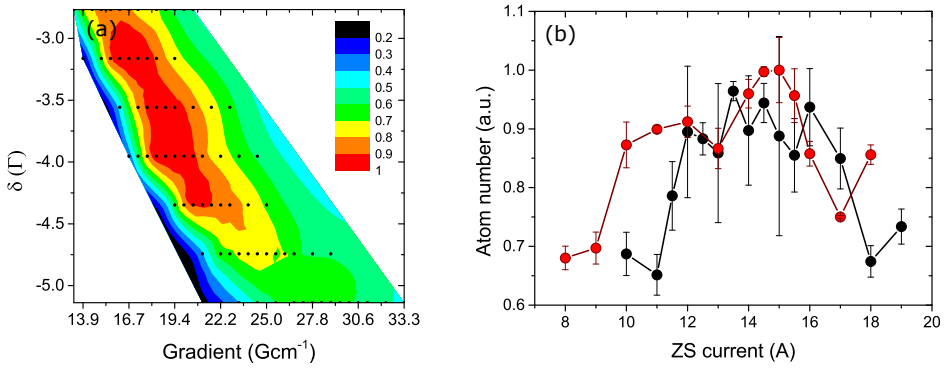

Figure 4.9: (a): Atom number as a function of MOT gradient and laser light detuning δ at a constant ZS coils current of $13\,A$. (b): Loaded atom number for two different MOT gradients of $16\,G/cm$ (red dots) and $20\,G/cm$ (black dots), as a function of the ZS coils current. Loading settings: ZS power, $\sim 100\,mW$, ZS laser detuning $\delta = -18.5\Gamma$; TC total beam power, $\sim 23\,mW$.

This result, relative to the Li case, is in poorer agreement with the optimum current settings predicted during the designing work, which correspond to a ZS coils current of $\sim 18\,A$ for a MOT gradient of $20\,G/cm$. The discrepancy can be ascribed to the perturbation induced by the ZS axial field on the MOT quadrupole position, causing its progressive displacement from the MOT beams inter-crossing region as the ZS current is increased. This hypothesis is supported by the observation of a strong dependence of the Cr MOT position and loading efficiency on the Li ZS coils current.

The Cr MOT loading efficiency was further investigated as a function of the ZS beam power. Fig. 4.10(a) shows the collected atom number as a function of loading time for different ZS beam powers P_{ZS}. The full saturation of the collected atom number is still not observed at the maximum power allowed by our optical setup, $P_{ZS} \simeq 100\,mW$. The loading data-sets were fitted with a single-exponential curve, yielding the $1/e$ time constants reported in Fig. 4.10(b) as a function of the ZS beams power. The observed behavior is rather constant within the experimental uncertainties, with an average value of $\tau_L \sim 0.12\,s$. This is consistent with the fact that the typical timescale for the exponential growth of the MOT signal is set by the single particle loss term.

With the same method as in Fig. 4.10, we investigated the total collected

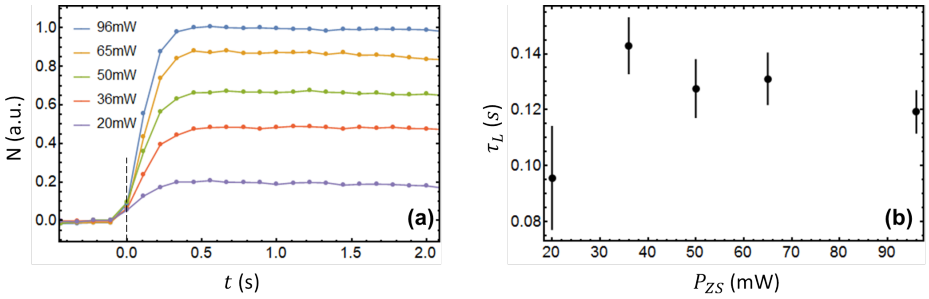

Figure 4.10: (a): Fluorescence signal as a function of the loading time for different ZS beam power, recorded on a Thorlabs CCD camera. The curves are obtained as an average over many loading cycles recorded under the same experimental conditions. For each considered ZS power, the reference time $t = 0$ was defined by the trigger level set here to $\sim 5\%$ of the maximum observed fluorescence signal. (b): Loading time constant τ_L, extracted by fitting data-sets in (a) with a single-exponential curve, as a function of the beam power. Loading settings: MOT current, $55\,A$ ($27.8\,G/cm$); ZS current, $14\,A$; ZS laser detuning, $\delta = -24\Gamma$; TC total beam power, $23\,mW$.

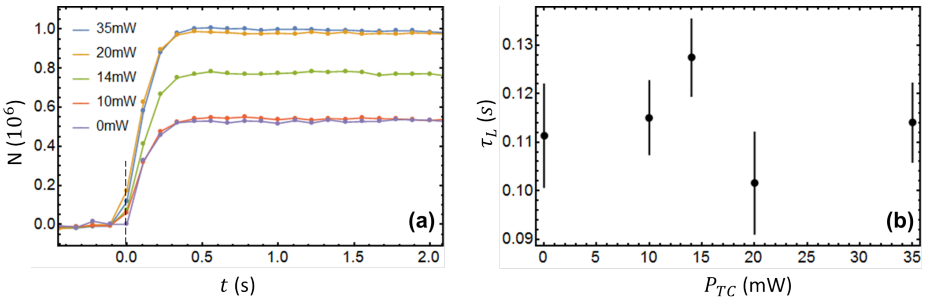

Figure 4.11: (a): Fluorescence signal as a function of the loading time for different TC beams total power, recorded on a Thorlabs CCD camera. Curves obtained as in Fig. 4.10. (b): Loading time constant, extracted by fitting data-sets in (a) with a single-exponential curve, as a function of the beams total power. Loading settings: MOT current, $55\,A$ ($27.8\,G/cm$); ZS current, $14\,A$; ZS beam power, $\sim 100\,mW$; ZS laser detuning, $\delta = -24\Gamma$.

atom number as a function of the transverse cooling laser power P_{TC}. Fig. 4.11(a) and (b) show respectively the loading curves and the relative $1/e$ time constants obtained for different total TC laser powers. We observe an increment of the collected atom number for $P_{TC} > 10 mW$, and its saturation at $P_{TC} = 20\, mW$. The $1/e$ loading time constant, instead, features again a constant behavior within the experimental uncertainties around an average value of $\tau_L \sim 0.12\, s$.

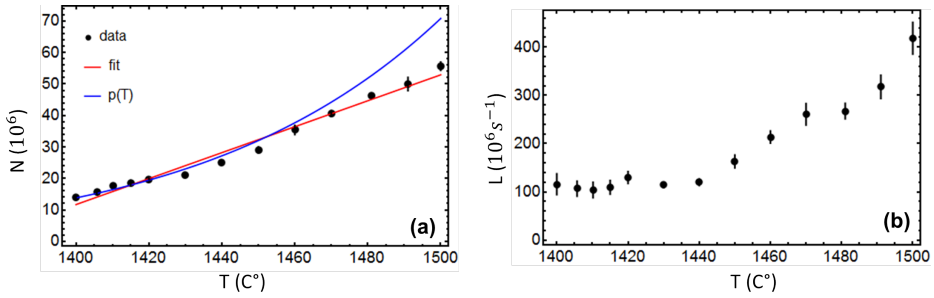

Figure 4.12: (a): Total collected atom number (dots) as a function of the oven temperature after a loading time of $7s$. A linear fit (red solid line) yields a slope of $0.41(1)\times 10^6/C^o$. The dataset was compared with the saturated vapor pressure behavior $P(T)$ (blue solid line) rescaled to the atom number observed at $T = 1400\, C^o$. The cloud was imaged after that the metastable D states atoms collected within the quadrupole were repumped back into the cooling cycle, by addressing the $|D_i\rangle \rightarrow |P_3\rangle$ repumper transitions with a $30\, ms$ flash of red repumpers laser lights. (b): Loading rate (dots) as a function of the oven temperature.

As a last remark on the investigation of our Cr MOT loading efficiency as a function of the operation settings, I report in Fig. 4.12(a) the trapped atom number after $7\, s$ loading as a function of the Cr oven temperatures, varied between $1400\, C^o$ and $1500\, C^o$. Here, the data account for the atom number collected both within the MOT and the quadrupole gradient. To this end, the cloud was imaged after that the magnetically trapped D state atoms were repumped back into the cooling cycle, by addressing the $|D_4\rangle \rightarrow |P_3\rangle$ and $|D_3\rangle \rightarrow |P_3\rangle$ atomic transitions with a $30\, ms$ flash of 663 and $654\, nm$ repumper laser lights, see next subsection for further detail on this procedure. The data, well matching a linear relation (solid red curve), are compared with the behavior expected on the basis of the temperature dependence of Cr vapor pressure (blue solid line), see Eq. (2.1), rescaled to the atom number attained at an oven temperature of $1400\, C^o$. The discrepancy observed at

large temperatures can be ascribed to the progressive deviation from the purely effusive regime of the Cr atoms emission dynamics.

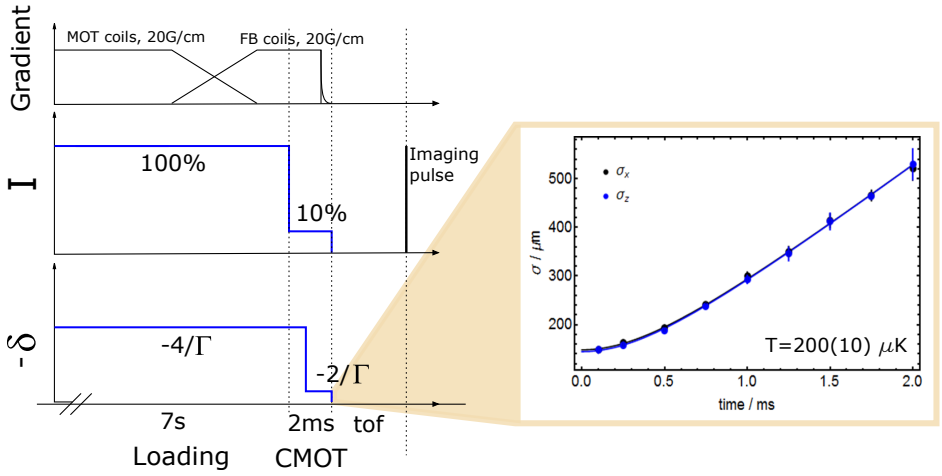

Figure 4.13: Sketch of our loading experimental routine. The drop of laser light intensity and detuning during the CMOT stage is indicated. As in the case of Li atom cloud, we transfer the Cr cloud from the MOT quadrupole into the Feshbach coils quadrupole during the loading time (upper diagram). The figure reports an example of time-of-flight expansion measurement of the cloud size within the imaged plane (dots). The curve was fitted with a ballistic scaling low $\sigma_i = \sigma_{0i}\sqrt{1 + t^2 k_B T/(m\sigma_{0i}^2)}$ [107] independently for both waits σ_x, σ_y, yielding an average temperature of $200(10)\mu K$.

In conclusion of this section, I exemplify in Fig. 4.13 the experimental routine exploited to load our Cr MOT. As for the Li case discussed in Sec. 4.1.1, the routine includes a CMOT stage at the end of the loading time. Here, the MOT beams power is decreased to 10% of the initial value, while the detuning is brought from $-4\,\Gamma$ to $-2\,\Gamma$. The CMOT stage lasts in this case for $2\,ms$, at the end of which the Cr cloud features a temperature of $T = 200\,\mu K$, see the time-of-flight expansion measurement reported in figure. The cloud features here a $1/e^2$ average waist of $\simeq 300\,\mu m$, yielding a maximum peak density of $n \simeq 1.3 \times 10^{11}\,cm^{-3}$.

4.2.2 Addressing Cr metastable D states with $663\,nm$ and $654\,nm$ resonant light

As explained in Sec. 3.1, the Cr MOT atoms can radiatively decay from the electronically excited $|P_4\rangle$ state into the $|D_3\rangle$ and $|D_4\rangle$ metastable states,

which can in turn be trapped within the quadrupole gradient thanks to their high magnetic moment. The trapped D state atoms can be repumped back into the cooling cycle by addressing the inter-combination repumper transitions $|D_3\rangle \rightarrow |P_3\rangle$ (653.973 nm) and $|D_4\rangle \rightarrow |P_3\rangle$ (663.973 nm), respectively [4].

Within our experimental setup, these additional laser lights are frequency locked to the Li atomic reference through a transfer Fabry-Pérot cavity. The frequency mismatch between the repumper transitions and the selected cavity modes is compensated via a double-pass AOM for both laser lights, see again figures 3.15 and 3.16. The exact location of each of the two repumper spectral lines has been experimentally retrieved as it follows. After a loading time of 7 s, the Cr MOT cloud was illuminated with a 30 ms long repumper laser pulse, and afterwards imaged with 425 nm laser light. The recorded atom number was monitored as a function of the double-pass AOM frequency. When the laser frequency became resonant with the repumper transition, the fraction of Cr atoms trapped within the high-field-seekers Zeeman sublevels of the addressed D state could be repumped back into the $|S_3\rangle \rightarrow |P_4\rangle$ cooling cycle, resulting into a strong increase of the 425 nm imaging signal. Fig. 4.14(a) and (b) show the experimental results obtained for 654 and 663 nm laser lights, respectively. The resonance feature, reported for three different laser powers, is fitted with a Lorentzian profile, yielding a frequency uncertainty of few MHz on the peak location for both lines. The peak location, monitored on a daily timescale, does not show a significant time dependence, featuring maximum drifts of the order of 10 MHz for both spectroscopic lines. This result confirms the good stability of our transfer cavity-based locking scheme.

We observe a saturation of the recorded atom number at a laser power of 15 mW (2 mW) for the 654 nm (663 nm) laser light, corresponding to a laser intensity of $2.4\,mW/mm^2$ ($0.3\,mW/mm^2$). The power-broadened signal features here a very large FWHM of the order of 100 MHz for both spectroscopic lines. In the limit of low power, the lines maintain a large FWHM of the order of 30 MHz and 50 MHz, for the 654 and 663 nm transition, respectively.

The duration of the red repumpers light flash was experimentally optimized by monitoring the behavior of the maximum observed atom number after 7 s loading, see Fig. 4.15. As observed, the optimum repumping efficiency is attained for a pulse duration between ~ 15 and $\sim 30\,ms$.

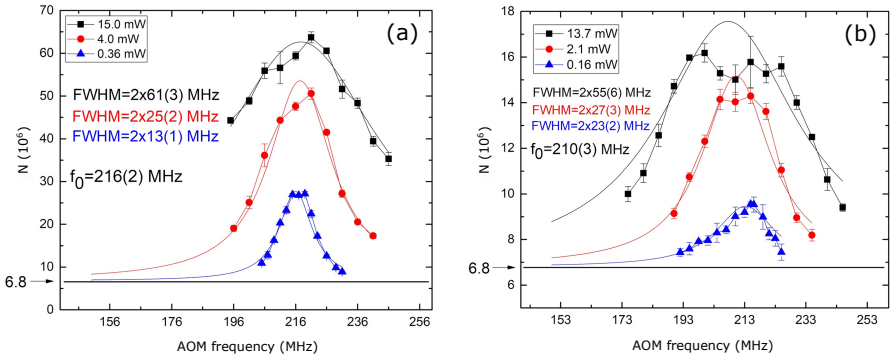

Figure 4.14: $425nm$ laser light absorption-imaging signal obtained after illuminating the Cr clouds with $654\,nm$ (a) and $663\,nm$ (b) repumper lights. The atom number is reported as a function of the frequency value of the laser-locking system double-pass AOM, see Sec. 3.3.3. The measurement is repeated for three different values of red repumper laser power, for both spectroscopic lines. We experimentally observe a saturation of the peak signal for $15\,mW$ (a) and $2\,mW$ (b). The data were fitted with a lorentzian lineshape (solid lines).

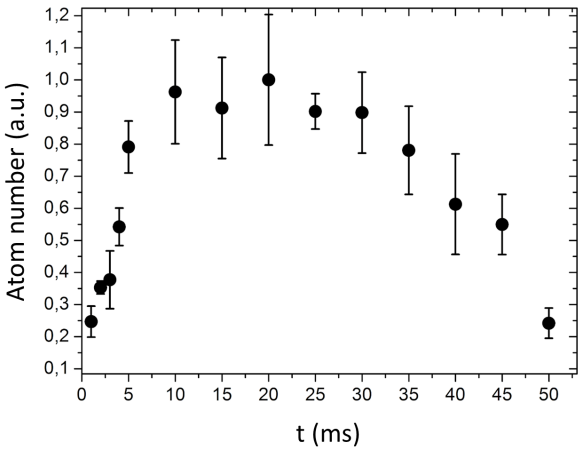

Figure 4.15: (a): $425\,nm$ laser light absorption-imaging signal as a function of the red repumpers laser pulse duration. The cloud was here simultaneously illuminated with both repumper laser lights. The maximum observed atom number at $14\,s$ corresponded here to $N_{max} = 7.5 \times 10^7$

Under the optimum conditions of intensity and duration of the repumpers laser pulse retrieved so far, we characterized the atom number relative to the magnetically trapped clouds of $|D_3\rangle$ and $|D_4\rangle$ metastable state atoms after a fixed loading time of 7 s. The results are summarized in Fig. 4.16(a). As expected from the relative branching ratio of $\sim 25\%$ and $\sim 75\%$, associated to the decay of Cr MOT atoms into the $|D_3\rangle$ and $|D_4\rangle$ states, respectively, we observe that the largest fraction of atoms trapped in the quadrupole occupies the high-field-seeker sublevels of the metastable $|D_4\rangle$ state, see relative peak heights in Fig. 4.16(a). The total atom number recorded by simultaneously addressing the two repumper transitions, also reported in the figure, is in excellent agreement with the sum of the contributions individually retrieved for the two metastable states.

The behavior of the total atom number collected within MOT plus quadrupole gradient as a function of the loading time is reported in Fig. 4.16(b) (black dots). While the MOT contribution to the total observed atom number saturates within hundreds of ms, see again Fig. 4.8, the timescale featured by the loading of the quadrupole trap extends to a few seconds. The maximum observed atom number at 14 s corresponded here to $N_{max} = 7.5 \times 10^7$.
The rate equation describing the trend in Fig. 4.16(b) can be retrieved as the sum of the following contributions:

$$\dot{N}_D(t) = +\alpha\Gamma_{M\to D}N_M(t) - \Gamma_D N_D(t) \tag{4.2a}$$

$$\dot{N}_M(t) = +L - (\Gamma_{M\to D} + \Gamma_M)N_M(t) \tag{4.2b}$$

being $N_D(t)$ and $N_M(t)$ the number of atoms collected within the quadrupole and in the MOT, respectively. $\Gamma_{M\to D}$ represents the decay rate featured by the Cr MOT atoms towards the D metastable states. Γ_M accounts for the remaining single particle losses mechanisms affecting the Cr MOT. Being $\tau_L \simeq 0.13\,s$ the loading time constant featured by the Cr MOT, it must be $(\Gamma_{M\to D} + \Gamma_M)^{-1} \simeq 0.13\,s$. Γ_D stems instead for the single particle decay rate associated to the D states trapped clouds. Finally, $\alpha < 1$ accounts for the collection efficiency of the quadrupole trap.
From Eq. (4.2) one straightforwardly derives

$$N_D^\infty = N_{max} - N_M^\infty = \frac{\alpha\Gamma_{M\to D}N_M^\infty}{\Gamma_D} \tag{4.3}$$

for the saturated atom number collected within the quadrupole, being $N_{max} = 7.5 \times 10^7$ and $N_M^\infty = 7.4 \times 10^6$ the saturated atom numbers observed within

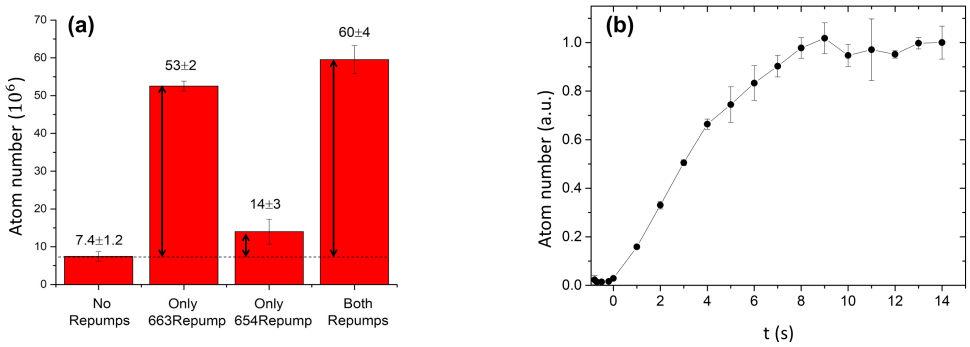

Figure 4.16: (a): Atom number observed after 7 s loading. The arrow indicate the quadrupole contribution to the total observed atom number. (b): 425 nm laser light absorption-imaging signal as a function of the loading time (black dots). The cloud was here simultaneously illuminated with both repumper laser lights.

the overall cloud and within the MOT, respectively. As I will show here in the following, both magnetically trapped clouds of $|D_3\rangle$ and $|D_4\rangle$ metastable states feature a lifetime of the order of 10 s, corresponding to a decay rate $\Gamma_D \sim 0.1\ s^{-1}$. Introducing these values in Eq. 4.3, one obtains $\alpha\Gamma_{M\to D} \simeq 0.9\ s^{-1}$.
Despite their simplicity, the arguments reported above allow to derive a lower bound for the decay rate $\Gamma_{M\to D}$, corresponding to the ideal case in which all atoms occupying the 7 high-field-seeker sublevels of the metastable $|D_3\rangle$ and $|D_4\rangle$ states are captured by the quadrupole gradient. Assuming a uniform distribution of the atoms among the 16 Zeeman sublevels, it must then be $\alpha = 7/16$, yielding $\Gamma_{M\to D} \simeq 2\ s^{-1}$. Despite its low accuracy, this result leads to very interesting observations. In particular, it implies that the decay rate associated with the de-excitation mechanism of $|P_4\rangle$ atoms into the D states, and the decay rate Γ_M, associated with pure Cr MOT losses, are of the same order of magnitude. Indeed, one finds $\Gamma_M = \tau_L^{-1} - \Gamma_{M\to D} \sim 5.7\ s^{-1}$.

As anticipated above, we also characterized the lifetime individually featured by the $|D_3\rangle$ and $|D_4\rangle$ atomic clouds. To this end, we proceed as follows. After a MOT loading of 7 s, the Cr oven shutter was closed, and the Cr ZS magnetic field and laser beam were simultaneously switched off. For each decay time, the cloud was illuminated with 654 nm (663 nm) laser light, and afterwards imaged with 425 nm laser light. During the whole routine, the

atoms were selectively collected within the $|D_4\rangle$ ($|D_3\rangle$) atomic state, by continuously addressing the repumper transition $|D_3\rangle \rightarrow |P_3\rangle$ ($|D_4\rangle \rightarrow |P_3\rangle$). The obtained experimental results are summarized in Fig. 4.17.
After a fast discharge within $t < 0.5\,s$, corresponding to the decay dynamics featured by the MOT atomic cloud, the data are well reproduced by a single-exponential decay curve for both $|D_4\rangle$ (blue circles) and $|D_3\rangle$ (green circles) trapped states, yielding a $1/e$ time constant of $\tau_4 = 16(2)\,s$ and $\tau_3 = 6.3(8)\,s$, respectively.
The data also show a relatively decreased total atom number selectively collected within both D state clouds, with respect to the previously retrieved results, see again Fig. 4.15(a). We attribute this effect to non-negligible light-assisted atomic losses induced on $|D_4\rangle$ ($|D_3\rangle$) quadrupole states by the presence of $654\,nm$ ($663\,nm$) laser light during the whole experimental routine.

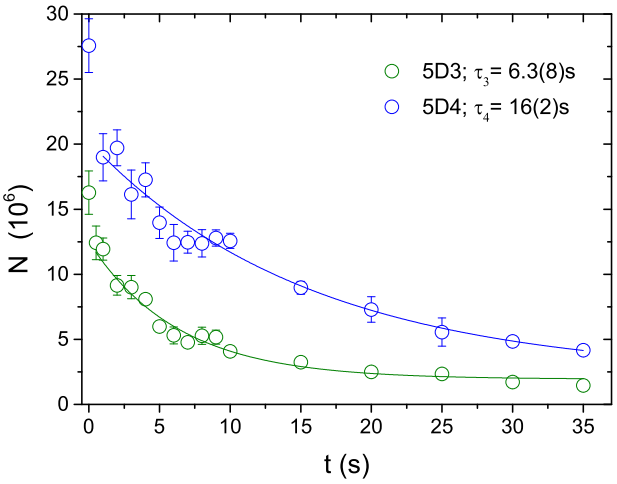

Figure 4.17: Quadrupole cloud atom number as a function of decay time. The quadrupole atoms were selectively collected within the $|D_3\rangle$ (green circle) or $|D_4\rangle$ (blue circles) state by continuously addressing the repumper transition $|D_4\rangle \rightarrow |P_3\rangle$ or $|D_3\rangle \rightarrow |P_3\rangle$, respectively, during the experimental routine. The $425\,nm$ laser light was here also left on during the whole routine, although the Cr MOT cloud contribution to the recorded atom number is decaying within $t < 0.5$, as expected.

4.3 Simultaneous loading of ^{6}Li and ^{52}Cr MOT clouds

Within the very last months of my PhD activity, we were able to perform the first experimental investigation of double-species trapped clouds of ^{6}Li and ^{52}Cr atoms.
In view of the implementation of an experimental routine enabling to simultaneously load the two species within the optical dipole trap, we characterized the lifetimes featured by the coexisting Cr and Li clouds. Our optical setup allows to independently tune in a controlled way the Cr and Li MOT beams alignment, such to reduce the spatial overlap of the two MOT clouds during the loading routine, and consequently suppress eventual inter-species inelastic processes. The clouds can be combined again on top of the quadrupole position during the final CMOT stage once the two ZS fields and lights are turned off, allowing for an optimum simultaneous loading within the ODT. For this reason, our investigation mainly focused on the decay dynamics featured by the Cr metastable D states atoms, which represent about 90% of the whole Cr population trapped within the quadrupole gradient, in presence of Li clouds. Very importantly, these preliminary measurements revealed a sizable but not fundamental perturbation induced by the Li cloud on both loading efficiency and lifetime featured by the Cr sample.
In order to characterize the lifetime featured by the magnetically trapped Cr D state atoms in presence of Li, we proceeded as it follows. We simultaneously loaded the Li and Cr MOT for $7s$. After that, the Li and Cr ZS currents and laser beams were switched off. The Cr oven shutter was also closed. Cr atoms were selectively collected within the $|D_3\rangle$ ($|D_4\rangle$) metastable state by continuously addressing the $|D_4\rangle \rightarrow |P_3\rangle$ ($|D_3\rangle \rightarrow |P_3\rangle$) atomic transition with the $663\,nm$ ($654\,nm$) repumper during the whole experimental routine. We finally illuminated the cloud with a $30\ ms$ pulse of $654\ nm$ ($663\ nm$) laser light right before taking the absorption image. The single species decay curves were recorded by simultaneously imaging the Li and Cr clouds at different decay times.
The experimental results are reported in Fig. 4.18. Green and blue dots in the left panel indicate the atom number collected within the $|D_3\rangle$ and $|D_4\rangle$ metastable states, respectively, as a function of time, in presence of Li MOT atoms. To allow for a direct comparison, the equivalent results in absence of Li atoms (green and blue circles) are also shown.

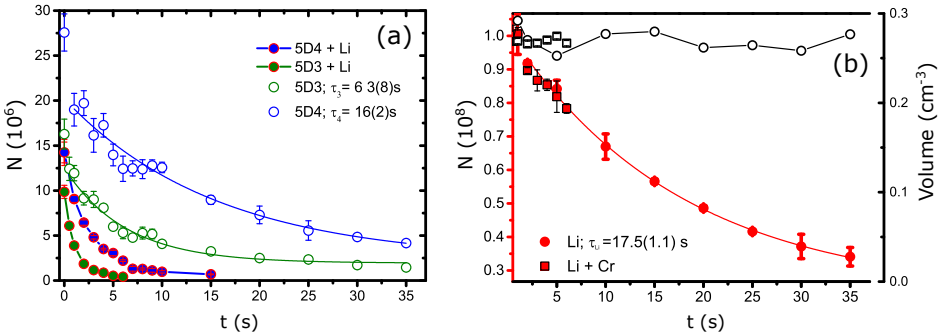

Figure 4.18: (a): Quadrupole cloud atom number as a function of decay time, in presence (dots) and absence (circles) of Li MOT clouds. The quadrupole atoms were selectively collected within the $|D_3\rangle$ (green symbols) or $|D_4\rangle$ (blue symbols) state with the same experimental routine as in Fig. 4.17. (b): Li MOT atom number (red symbols) and cloud waist (white symbols) in absence (dots) and presence (squares) of Cr clouds. No CMOT stage was operated on the Li MOT cloud in this experiment.

By looking at the initial time $t = 0$ one can notice how the presence of Li atoms reduces by about a factor 2 the Cr atom number collected within the quadrupole, for both $|D_3\rangle$ and $|D_4\rangle$ metastable states. Additionally, the quadrupole lifetimes are also sizably reduced.
The behavior of the Li MOT atom number as a function of decay time is reported in Fig. 4.18(a). Here, the data are fully consistent with the results obtained in absence of Cr (red circles). The size of the Li MOT cloud is also monitored (white squares), and it features a constant behavior, again fully consistent with the results obtained in absence of Cr (white circles). Under these considerations, the time-evolution of the D states Cr atom number can be described, within a good approximation, by the following relation:

$$\dot{N}_{Di}(t) = -\beta_{Di} N_{Li}(t) N_{Di}(t) - \frac{1}{\tau_i} N_{Di}(t) \tag{4.4}$$

Here $N_{Li}(t) = N_0 \exp(-t/\tau_{Li})$ describes the evolution of the Li atom number. The $1/e$ decay constant was extracted from an exponential fit of the Li decay curve, yielding $\tau_{Li} = 17.5\ s$ (solid red line in of Fig. 4.18(b)). τ_i is the decay time featured by the quadrupole clouds in absence of lithium, already discussed in Sec. 4.2.2. β_{Di} stems here for the inter-species two-body losses rate parameter.
The much longer timescales characterizing the decay of D state atoms in absence of Li MOTs directly imply that $\tau_i \gg (\beta N_{Li})^{-1}$. Then, the second

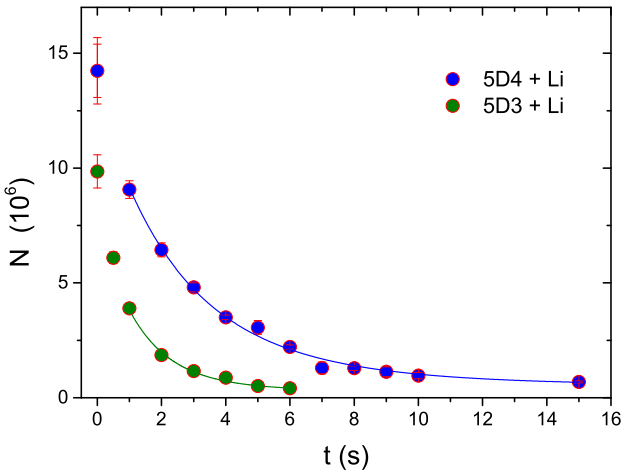

Figure 4.19: $|D_3\rangle$ (green symbols) or $|D_4\rangle$ (blue symbols) quadrupole clouds atom number as a function of decay time, in presence of Li MOT clouds. The data were fit with relation (4.5) (solid lines).

term in Eq. (4.4) can be neglected, resulting in a time evolution of the kind:

$$N_{Di}(t) = N_{Di,0} e^{(N_0 \beta_{Di} \tau_{Li} (e^{(-t/\tau_{Li})} - 1))} \tag{4.5}$$

Fig. 4.19 shows the results obtained by fitting the quadrupole decay curves with Eq. (4.5). As already discussed for the experimental results retrieved in Sec. 4.2.2, the Cr atom number at $t < 0.5s$ accounts for both the contribution from those atoms confined in the MOT and within the quadrupole field. For this reason, the fit was only extended to data-points at $t \geq 1\,s$. The values of β_{Di}, extracted from the fit, where rescaled to the (constant) volume featured by the Li MOT cloud, obtaining $\beta_{D3} = 1.4(4) \times 10^{-10} cm^3 s^{-1}$ and $\beta_{D4} = 7(2) \times 10^{-11} cm^3 s^{-1}$ for the $|D_3\rangle$ and $|D_4\rangle$ metastable states, respectively.

Although allowing for a phenomenological derivation of the inter-species two-body losses rate parameters featured by the Cr quadrupole clouds in presence of Li MOT atoms, our analysis does not suffice to determine the specific mechanisms leading to the observed quadrupole losses. This is due to the poor resolution affecting the measurement of the Li MOT atom number during the decay time, which impedes the characterization of eventual MOT losses induced by the Cr cloud. Indeed, the experimental uncertainties on the Li MOT atom number, of the order of 10%, result to be comparable with

the small atom number observed for the Cr quadrupole cloud ($\leq 10^7$).

As a conclusion of this last section, I remark how the experimental results reported above demonstrate the possibility to simultaneously produce cold Cr and Li samples within our experimental apparatus. In spite of a less efficient accumulation of D-state Cr atoms in the magnetic quadrupole of the MOT, the presence of a $\sim 10^8$ Li atom MOT does not prevent the loading of chromium samples comprising up to $\sim 2.5 \times 10^7$ atoms at about 200 μK within a few second experimental cycle. This appears as an extremely promising starting point for the loading of the mixture in the ODT, and for the successive evaporative and sympathetic cooling steps.
Achieved these very satisfying results with our newly produced dual species clouds of Li and ^{52}Cr atoms, we are currently focusing our work on the achievement of MOT clouds of fermionic ^{53}Cr atoms. In particular, we operated spectroscopic measurements both on the Cr atomic beam effused from the oven and on the spectroscopic HC-lamp, which allowed us to successfully lock our master laser to the fermionic atomic reference. Moreover, we are currently implementing an optical pumping scheme operating at the transverse cooling stage of our experimental setup, in order to maximize the flux of fermionic Cr atoms captured by the Zeeman slower. We are very confident that this optimization work will allow us to attain our first magneto-optically trapped clouds of ^{53}Cr within the very next weeks.

Chapter 5

Coherent and dissipative Josephson dynamics in ^{6}Li superfluids

I present here the work that I conducted in parallel with my main PhD activity, described in the previous chapters, on the experimental investigation of the Josephson dynamics [112,113] of ^{6}Li superfluids through a thin barrier across the BEC-BCS crossover [15, 16]. The work is a natural extension of my Master thesis activity, which was carried out in the laboratory of Dr. G. Roati at LENS, and contributed to the work published in Ref. [114].
I will present and analyze experimental results for the maximum Josephson coherent current within a wide range of barrier heights, and characterize the onset of dissipative flow as soon as the critical current is exceeded. I will show how the dissipative mechanisms do not hinder the Josephson dynamics, which is fully recovered at longer times. I will also show the existence of a further upper threshold, above which the system completely loses its coherence and does not recover Josephson oscillations.
The chapter is structured as follows: Sec. 5.1 generally introduces the Josephson effect within a tunneling Hamiltonian description, as well as the key results of the theoretical works published in Ref. [115]. Sec. 5.2 presents the experimental platform and its characterization within the small oscillations Josephson regime. Sec. 5.3 is dedicated to the extraction of the maximum coherent current, and it shows the comparison with the theoretical results in Ref. [115] and with numerical simulations within the BEC regime. The simulations where brought on by our collaborator K. Xhani, from the group

of Prof. N. Proukakis in Newcastle, and are discussed in Ref. [6].

5.1 The Josephson effect

The Josephson effect (JE) is a many-body quantum phenomenon which unveils the gauge symmetry breaking associated to the order parameter of a macroscopically occupied state, the condensate phase. In particular it directly links a measurable quantity, a current of particles through a weak link, to the phase difference $\phi = \phi_L - \phi_R$ between two (left and right) superfluid states separated by the link.
Within a first order approximation the current-phase relation (CPR) in a Josephson junction (JJ) reads:

$$I(\phi) = I_c \sin(\phi) \tag{5.1}$$

with maximum current I_c, and a ground state energy corresponding to the equilibrium configuration $\phi = 0$.

The oscillating behavior (5.1) was first predicted within the frame of fermionic systems in 1962 by B. D. Josephson for a superconductor junction [112], where a constant voltage drop between two superconductors is expected to generate an oscillating current; the effect was then experimentally observed few months later by P. W. Anderson and J. M. Rowell [116]. For two linked bosonic phases instead, the JE was first observed twenty years later by O. Avenel and E. Varoquaux [117] in superfluid ^{4}He [118–121].
Within the last several years, the experimental advances in the field of ultracold atomic gases has triggered a large interest in JJs of weakly interacting BECs, both experimentally [122–129] and theoretically [130–135]. In these works the junction is typically composed by two superfluids separated by a potential barrier with a thickness which is large or comparable with the superfluid healing length; the theoretical description of the system is based on the Gross-Pitaevskii equations (GPEs), where interparticle interactions are taken into account by a mean-field term $\propto a \cdot n(\mathbf{r}, \mathbf{t})$, being a the scattering length and $n(\mathbf{r}, \mathbf{t})$ the spatial and time dependent superfluid density [14].
Less advanced is instead the experimental investigation of JE in ultracold fermionic superfluids [19, 114, 136–144]. These systems are potentially very appealing, as they allow to experimentally encompass the physics of BEC superfluid and BCS superconducting junctions via the interaction tunability offered by the Feshbach resonance phenomenon, crossing over the interesting

regime of unitary Fermi gases.
The description of the JJ dynamics throughout the BEC-BCS crossover typically relies on the analysis of numerical simulations based on the time-dependent Bogoliubov-de Genne (BdG) equations. The BdG mean-field equations are the equivalent of the Schroedinger equation for two-component fermionic wavefuntions with arbitrarily large interparticle attraction in presence of a superconducting energy gap. They enable also to generalize the standard mean-field BCS approach for superconducting junctions to the case of spatially inhomogeneous trapped systems [139, 145].

Independent BdG calculations exist in literature both for the tunneling regime where the potential barrier $V_0 \gg \mu$, being μ the superfluid chemical potential [19], and in the hydrodynamic regime where instead $V_0 \ll \mu$, in which the barrier can be envisioned as a small obstacle for the superfluid flow [138]. These two limiting cases have been treated for a bosonic JJ by a microscopic approach in Ref. [136] and by a mean-field approach in Ref. [146]. Yet, a unified picture connecting the $V_0 > \mu$ and $V_0 < \mu$ regimes throughout all interaction regimes of the BEC-BCS crossover is still lacking. Nonetheless, the recently published work [115] shows that the smooth connection between the tunneling and the low barrier limit, up to $V_0/\mu < 1$, can be quantitatively captured by taking into account second order contributions in the JJ current amplitude within a very intuitive analytic approach, which appears to hold both within the BEC and the BCS limit. A discussion of the Josephson dynamics within an second order Hamiltonian description, as well as of the key results from Ref. [115] is presented here in the following.

In order to capture the effects of second order contributions to the JJ dynamics, it is instructive to first look at the idealized case in which only the first order current (5.1) is considered. Within this frame the relative phase ϕ and the relative population $z = (N_L - N_R)/2$ behave like canonically conjugate variables [113]. Generally, for small oscillations, the system Hamiltonian can be approximated to the sum of two energy terms: the Josephson energy $E_J(\phi) = -E_J \cos\phi$ and the charging energy $E_C z^2/2$, resembling the kinetic and potential energy of a pendulum, respectively. The first term favors the coherent flow of particles through the junction, and it yields the non-dissipative current:

$$\hbar I(\phi) = -\hbar \dot{z} = \frac{\partial H}{\partial \phi} = \frac{\partial E_J(\phi)}{\partial \phi} \tag{5.2}$$

The second term represents instead the energy cost associated with a population imbalance; being $E_C = \frac{\partial \mu_{loc}}{\partial N_L}$ one has:

$$\dot{\phi} = \frac{\partial H}{\partial \hbar z} = -\frac{\Delta\mu}{\hbar} \tag{5.3}$$

Consequently, for a fixed total particle number N (as in trapped gases experiments) both z and ϕ undergo harmonic oscillations, out of phase by $\pi/2$, at a plasma frequency ω_p given by:

$$\omega_p = \frac{1}{\hbar}\sqrt{E_C E_J} \tag{5.4}$$

Consistently with the limit of small oscillations, the time variation of the left and right superfluids properties with the number of transferred particles is negligible, and E_J and E_C can be assumed constant (two-mode approximation [130, 133]).
The dynamics can be triggered both by setting the initial conditions $\phi_0 = 0$, $z_0 \neq 0$, or $\phi_0 \neq 0$, $z_0 = 0$. In the first case, corresponding to the experimental procedure treated in this work, it can be found a maximum initial imbalance z_0 that the system can convert into a coherent flow of particles. This is straightforwardly derived by the periodic expression for $|E_J(\phi)|$, which is bounded by the condition $|cos(\phi)| = 1$. Namely, once the initial excitation exceeds a critical value, the system won't be able to fully convert the charging energy into kinetic (Josephson) energy. The system enters in this case the so called macroscopic quantum self-trapping (MQST) state, first considered in [130]. Here the current flow is halted with $z(t) \sim z_0$, since energy conservation requires that a finite charging energy is maintained across the junction, in absence of any dissipation mechanism.

In light of the forthcoming discussion of the experimental data, it is useful to consider how second order contributions to the CPR modify the scenario above described. To this end, it is instructive to recall the analytic results derived in Ref [137], where the following CPR is considered:

$$I(\phi) = I_c(\sin(\phi) + g\sin(2\phi)) \tag{5.5}$$

where I_c and g are assumed constant. The term of amplitude $I_1 = |gI_c|$ is a second harmonic, as it should be in a time reversal invariant situation, where the Josephson energy must remain periodic in ϕ (see again Eq. (5.2)).

The relation Eq. (5.5) generally models the JJs for which, in absence of any superfluid current, the phase drop across the link is $0 < \phi < \pi$. Experimental examples are found in d-wave superconductors or JJs with ferromagnetic barriers (ϕ-junctions) [137, 147]. For the case of a bosonic JJ, Eq. (5.5) reproduces the trend obtained by treating the tunneling Hamiltonian as a perturbation, and evaluating the coherent current up to second order terms. The Josephson energy can be redefined such to fulfill Eq. (5.2):

$$E_J(\phi) = \frac{\hbar I_c}{2}\big\{1 - \cos(\phi) + \frac{g}{2}(1 - \cos(2\phi))\big\} \tag{5.6}$$

I will restrict here the attention to small and negative second order amplitudes, with $-0.5 < g < 0$. For these values, a global minimum within the range $-\pi < \phi < \pi$ is found for $E_J(0) = 0$; the maximum system excitation that can be fully converted in kinetic energy thus corresponds to the global maximum $E_J(\pi) = \hbar I_c$. The trend $E_J(\phi)$ and the maximum allowed excitation energy are sketched in Fig. 5.1(a) for the case $g = -0.4$ as an example. The one to one correspondence of the maximum excitation energy with the maximum first order coherent current, as found in the first order Hamiltonian description, is not a general property of the system and is modified at larger values of $|g|$. A detailed discussion of the stable and metastable configurations corresponding to the global and local minima of $E_J(\phi)$ depending on g is found in Ref. [137].
The effect of the second order contribution emerges instead at any g in the expression for the maximum coherent current sustained by the system; it is in fact:

$$I_{Max} = I_c \frac{1}{32|g|}(\sqrt{1 + 32g^2} + 3)^{3/2}(\sqrt{1 + 32g^2} - 1)^{1/2} \tag{5.7}$$

It is worth noticing that it is always $I_{Max} > I_c$, regardless the sign of g (see Fig. 5.1(b)).

Aside for causing a modification of the CPR and an increase of the coherent current allowed through the junction, the presence of second order effects in bosonic JJs also introduce dissipative currents. For initial excitation energies exceeding the Josephson energy gap set by Eq. (5.6), the MQST effect expected at the first order in the tunneling Hamiltonian is eliminated at the second order level by dissipation mechanisms associated with non-coherent current contributions. The theoretical work reported in Ref. [136] models the Josephson current within a perturbative approach up to second order terms

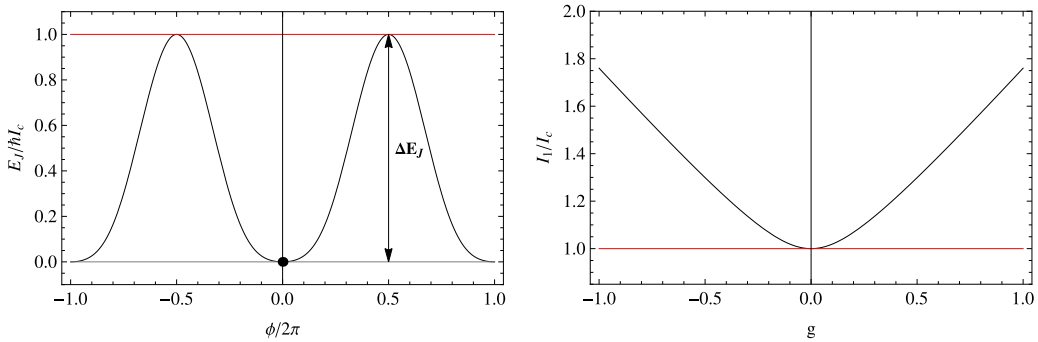

Figure 5.1: (a): Josephson energy as a function of the relative phase, for $g = -0.4$ (solid black) and $g = 0$ (dashed gray). The maximum kinetic energy associated to the maximum coherent current is indicated in figure. (b): Trend of I_{Max} renormalized to I_c, as a function of g.

in the tunneling amplitude probability for weakly interacting Bose gases in the limit $V_0 \ll \mu$. The CPR Eq. (5.5) is then modified according to:

$$I(\phi) = I_c \sin(\phi) - I_1 \sin(2\phi) + I_2(\Delta\mu)\cos(2\phi) + I_N(\Delta\mu) \qquad (5.8)$$

Together with the expected coherent contributions, the model predicts two dissipative terms: one depends only on the chemical potential difference $\Delta\mu$, the other one features also a sinusoidal dependence on ϕ.
It is relevant to notice that the second order contributions here derived for bosonic particles are in perfect analogy with the ones derived in literature for superconducting fermion pairs within the frame of the standard homogeneous BCS theory (see for example Ref. [148], Ch. 2). Nonetheless, one should remark that the origin of the various terms in the BEC and BCS cases arise from different michroscopic tunneling processes. In superconductors, where the JE is associated with tunneling of pairs, the first order term vanishes, and the dynamics is mainly driven by the second order coherent term.
The current amplitudes I_c, I_1, $I_2(\Delta\mu)$ and $I_N(\Delta\mu)$ are explicitly calculated in Ref. [136] for a homogeneous box system in a parallelepiped box bisected by a square barrier of width d in the limit $\Delta\mu << \mu$. The authors showed that under these conditions I_c and I_1 are constant in $\Delta\mu$ (and thus in $z(t)$), as it should. In a consistent way, the dissipative contributions I_2 and I_N have ohmic character $\propto \Delta\mu$.
The dissipative contributions destabilize the MQST regime, yielding an irreversible decay of the population imbalance, followed, eventually, by a restor-

ing of Josephson dynamics, once the initial excess charging energy has been dissipated.

Recently, the authors of Ref. [115] pointed out that the perturbative results by [136] can be recast in terms of the single-particle transmission coefficient $\sqrt{T}$ associated to the square barrier. The following relations for the current densities are then obtained:

$$\hbar j_c = 2\xi n_c \mu \frac{\sqrt{T(V_0,\mu)}}{4} \tag{5.9a}$$

$$\hbar j_1 = 2\xi n_c \mu \big(\frac{\sqrt{T(V_0,\mu)}}{4}\big)^2 \tag{5.9b}$$

$$\hbar j_2 = \hbar j_N = 2\sqrt{2}\xi n_c \Delta\mu \big(\frac{\sqrt{T(V_0,\mu)}}{4}\big)^2 \tag{5.9c}$$

In the limit $V_0/\mu \ll 1$, $\sqrt{T(V_0,\mu)} = 4\frac{e^{-k_\mu d}}{k_\mu \xi}$, where $\hbar k_\mu = \sqrt{2M(V_0-\mu)}$, M is the mass of one boson, $\xi = \hbar/\sqrt{2M\mu}$ and n_c is the superfluid condensed density.

The simple analytic structure of the relations Eq. (5.9) is quite striking: in particular, it suggests that the Josephson current corresponds to the flow of all and only the condensed bosonic particles laying at the energy μ and transmitted through the barrier as they where non interacting. Moreover, Eq. (5.9) imply that both coherent and dissipative currents may be evaluated for any junction and reservoirs geometry solely based on the knowledge of bulk properties of the superfluid state (condensed fraction and chemical potential), and of the single particle transmission coefficient, with no need to account for complicated microscopic dynamics occurring near the barrier region.

Notably, the authors remark that such a structure quantitatively holds not only in the BEC limit but also throughout the crossover, up to the BCS limit. This is justified by the analogy of relation (5.9a) with the celebrated Ambegaokar-Baratoff formula for the major contribution to the coherent current of superconducting fermions across a thin and strong barrier, derived within the frame of BCS theory. Indeed, at least at the mean-field level, the Ambegaokar-Baratoff formula can be recast as [139]

$$j_{BCS} \sim \xi_F n_{cF} \mu_F T_F(\mu_F, V_{0F}) \tag{5.10}$$

where T_F is the transmission coefficient for a fermion laying at the chemical potential μ_F.

Under these considerations, the authors naturally obtain an intuitive explanation to the trend of the maximum Josephson current as a function of the interparticle interaction in BEC-BCS crossover Fermi gases, where both experimental observations [114] and BdG calculations [19,138] show an enhancement in correspondence of the unitary limit. Previous studies ascribed such a non-monotonic behavior to the competition of fermionic and bosonic excitation branches: pair-breaking on the BCS and sound on the BEC regime, respectively. According with the extension to Eq. 5.9 throughout the BEC-BCS crossover, the authors of [115] provided an alternative explanation: this non-monotonic trend derives from the competition of the condensed fraction density n_c and the factor $\mu\sqrt{T(\mu, V_0)}$. Indeed, by increasing the interaction strength starting from the BEC limit, n_c remains roughly constant ($n_c \sim n_{tot}$), while the chemical potential and the transmission coefficient monotonically increase, causing a heightened I_c. When starting from the BCS limit and approaching the crossover region, the trend is reversed, with the energy and tunneling probability of particles featuring a weak dependence upon the interaction strength ($\mu \sim E_F$), whereas n_c exponentially grows with the interaction.

The authors of Ref. [115] validate their results on the BEC limit by extending relations (5.9) to the case of the inhomogeneous trapped gas bisected by a Gaussian barrier, and comparing the obtained trends both with the published data of Ref. [144] and with the unpublished data that I present and analyze in the present chapter.
As I will show in Sec. **??**, the agreement between the analytical results and the experimental data, as well as GPE numerical calculations, remains good in a wide range of barrier heights, down to $V_0/\mu < 1$, despite Eq. (5.9) have been initially derived from a second order perturbation theory in the tunneling limit.

5.2 Experimental platform and system dynamics within the small excitation regime

The experimental studies discussed here and in the forthcoming section have been carried out in the Lithium lab led by Dr. G. Roati at LENS. While I refer to [82, 93, 114, 144] for a detailed description of the apparatus, here I only recall the experimental conditions we employed to investigate Josephson

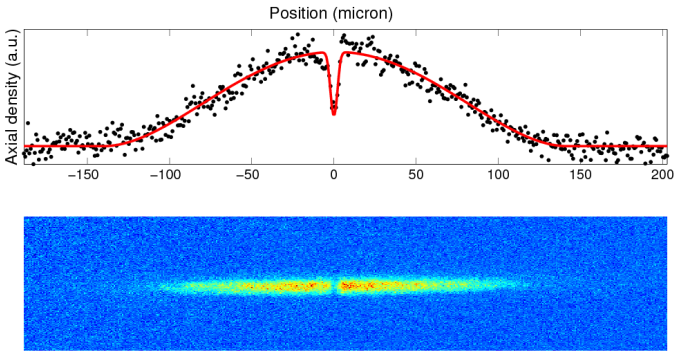

Figure 5.2: Density profile of the bisected atomic cloud (above) and an example of absorption image (below). Data taken within the BEC side of the Feshbach resonance.

dynamics with a fermionic superfluid of ultracold ^{6}Li atoms throughout the BEC-BCS crossover.

Our Josephson junction is realized by a superfluid cloud of typically $N \sim 10^5$ ^{6}Li atom pairs, held in a cigar-shaped crossed optical dipole trap, bisected along the axial direction into two symmetric reservoirs by a thin optical barrier. The harmonic potential is characterized by an axial (radial) trap frequency of about $\nu_x \sim 15 Hz$ ($\nu_\perp = \nu_y = \nu_z \sim 170\, Hz$), whereas the barrier is realized by a strongly anisotropic Gaussian beam at $532\, nm$, blue detuned with respect to the main optical transition of lithium (see Fig. 5.2), propagating along the vertical (z) direction and featuring $1/e^2$ beam waists of $w_x = 2.0(0.2)\ \mu m$ and $w_y = 840(30)\ \mu m$ along the x and y directions, respectively. The barrier height V_0 is generally obtained based on the knowledge of the beam waists and on the optical power set for the repulsive beam, although a different calibration method will be discussed at the end of the section.
The bosonic pairs are realized by lithium atoms into the two lowest Zeeman sublevels $|F = 1/2; m_F = \pm 1/2\rangle$, in the vicinity of the broad Feshbach resonance located at $832\, G$, which enables to tune the interaction strength and, correspondingly, the pair chemical potential.

The system dynamics is induced as it follows: by adjusting the AOM frequency of the laser beam that determines the axial confinement of our crossed trap, the barycenter of the superfluid cloud is initially displaced with respect to the barrier position, yielding at equilibrium a nonzero population

imbalance $z_0 = (N_L(t=0) - N_R(t=0))/N$ between the left (L) and right (R) reservoirs. A non-adiabatic switch of the trapping beam AOM frequency then moves the axial trap center back on the barrier position, initializing the dynamics which is investigated by recording the subsequent time evolution of $z(t) = (N_L(t) - N_R(t))/N$ (for further details, see supplementary material in Ref. [114]).

Quite generally, i.e. irrespective of the specific barrier height and interaction strength, the dynamics can be separated into three distinct regimes, see Fig. 5.3, which sensitively depend upon the initial z_0, hence the initial charging energy of the JJ. For small z_0 values, see e.g. Fig. 5.3(a), the system evolution is characterized by coherent, undamped sinusoidal oscillations, occurring at a plasma frequency $\omega_p \leq \omega_x$ which depends upon the specific barrier height and pair chemical potential, see Eq (5.4). As the initial imbalance is increased above a critical value z_c, the dynamics qualitatively changes, see Fig. 5.3(b), $z(t)$ exhibiting a rapid discharge, followed by the restoring of coherent oscillations characterized by the same plasma frequency obtained for $z_0 < z_c$, and amplitude of approximatively z_c. The initial decay of $z(t)$ in this regime marks the onset of a dissipative normal current ($I \propto dz/dt$), which results into an irreversible particle flow from the left reservoir (at higher initial chemical potential, i.e. "higher voltage") to the right one. Eventually, for $z_0 \gg z_c$ and for sufficiently large V_0 values, the dynamics becomes purely dissipative and no coherent oscillations are restored at any time, see Fig. 5.3(c).

Let us first focus on the properties of our junction under the condition of small initial imbalances $z_0 \sim 0.03$, and let us discuss the dynamics in the dissipationless regime. By fitting to an undamped sinusoidal function the time evolution of $z(t)$ as the one shown as an example in Fig. 5.4(a), I extracted the plasma frequency for different barrier heights and interactions strengths. The result of this characterization is summarized in Fig. 5.4(b): Here I show the experimentally determined ω_p, normalized to the bare axial trap frequency $\omega_x \equiv \omega_0$, as a function of the barrier height (in units of $\hbar\omega_0$), for interaction regimes spanning from the far BEC limit (yellow circles) to the BCS side (gray circles) of the crossover.

For each interaction strength, the trend of ω_p is qualitatively the same: for vanishing barrier heights, much lower than the boson chemical potential μ_B, $\omega_p \sim \omega_0$. As V_0 is increased, the plasma frequency becomes progressively slower, and it is strongly reduced as $V_0 > \mu_B$. This behavior, for any given

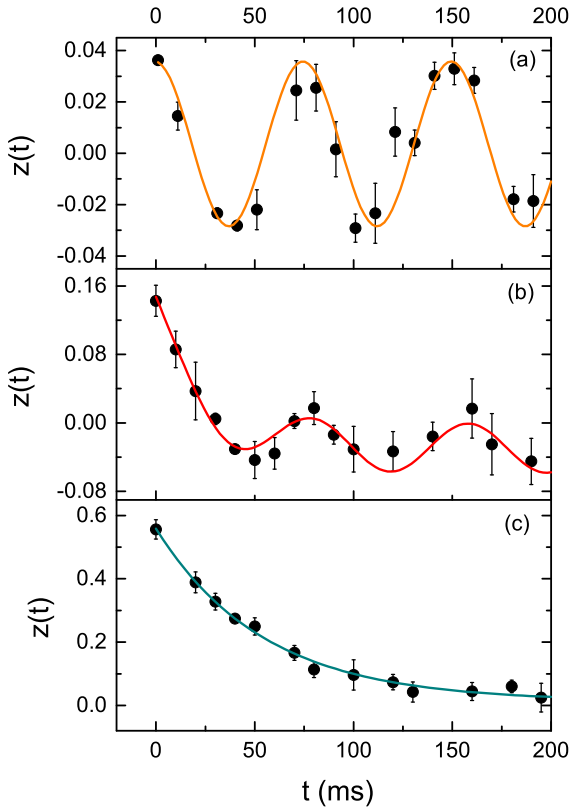

Figure 5.3: Examples of full oscillation dynamics following different initial imbalances. BEC regime, $-1/k_F a = -4.25$; $V_0/\mu \simeq 1$.

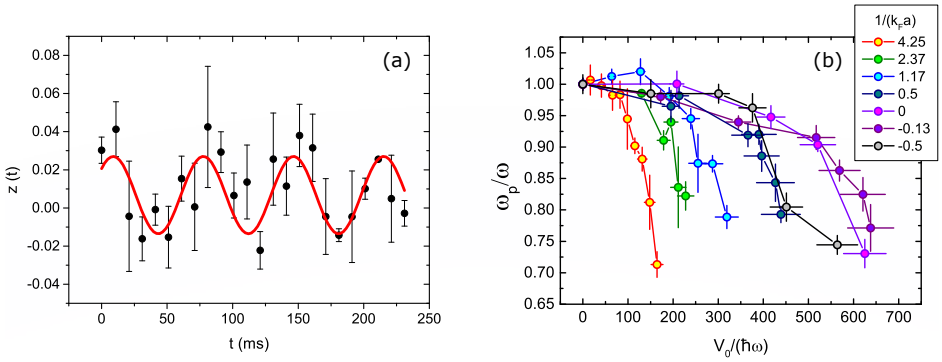

Figure 5.4: (a): $z(t)$ time evolution (black dots) and sinusoidal fit (red curve), yielding $\omega_p = 14.5(3)\ Hz$. Error bars corresponding to a statistics of 5-10 data per time. $V_0 \propto 5\ mW$, corresponding to $V_0 \sim \mu_0$, being μ_0 the peak chemical potential. Data taken in the BEC regime. (b): ω_p fro different interaction regimes as a function of the barrier height value renormalized to the bare trap frequency ω_0.

$k_F a$ value, can be qualitatively understood recalling that ω_p, in a two-mode approximation, depends on the Josephson coupling energy $E_J = \hbar I_c$, see Eq (5.4), which in turn sensitively depends on the single-particle transmission amplitude $\sqrt{T(\mu_B)}$ evaluated at the (local) boson chemical potential [114]. As the barrier height is increased, the transmission is progressively reduced, more strongly once all superfluid pairs of our trapped inhomogeneous sample enter the tunneling regime. Given that the chemical potential of the superfluid pairs sizably increases as one moves from the BEC to the BEC limit of the crossover, the tunneling regime is reached for molecular BECs for barrier heights $V_0/\hbar\omega_0$ much smaller than those required for unitary or BCS superfluids.

The plasma frequencies can be extracted by fitting the $z(t)$ dynamics up to a critical barrier height V_{0c}, beyond which the experimental data do not match anymore with a purely sinusoidal oscillation, the system entering the dissipative regime. Such a critical barrier height corresponds, for each interaction regime presented in Fig. 5.4(b), to the last point of the corresponding dataset, and it depends upon the initial imbalance z_0. Also this trend can be qualitatively understood in the two-mode approximation: the coherent flux, corresponding to the Josephson plasma oscillations, is prevented once the initial charging energy, set by the initial imbalance z_0, exceeds the Josephson energy $\hbar I_c$. At this point, the system cannot convert the whole capacitive energy stored initially in the junction into a coherent particle current, and

the superfluid dynamics is adjoined by the development of a dissipative, irreversible flow, see Fig. 5.3(b).

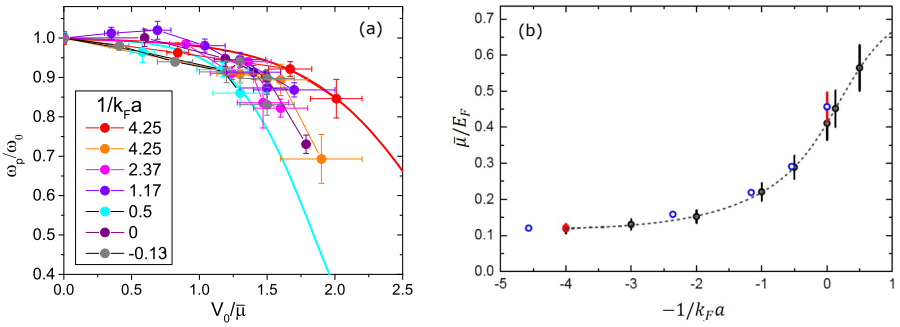

Figure 5.5: (a): $\omega_p(V_0/\bar{\mu})$ for different interaction strength regimes. The experimental results are consistent within a confidence region upper (lower) limited by the fit results represented as solid red (cyan) curves. (b): Trap averaged chemical potential $\bar{\mu}$ (gray circles) as a function of the interaction parameter, obtained from the critical barrier height V_{ex} at which the system starts to feature for large imbalances purely dissipative dynamics. Error bars account for the uncertainty in determining V_{ex} and in evaluating the Fermi energy E_F of the corresponding non interacting gas. Blue empty points: expected trend for $\bar{\mu}$ obtained for a $T = 0$ cloud at equilibrium based on the EFTM model of Ref. [114,144]. Red symbols: $\bar{\mu}$ for BEC and unitary points, evaluated with the analytic relations available in these regimes, with error bars accounting for the uncertainties in atom number and trap frequencies.

In order to get a better insight into such behavior of ω_p throughout the $k_F a - V_0$ space, it is convenient to look at the data by normalizing the barrier height to the trap averaged chemical potential of the pairs. This is shown in Fig. 5.5(a). In this case, all the different trends fall within a much smaller region of the graph, although not perfectly overlapping. Indeed, in this case the main impact on the ω_p/ω_0 behavior, connected with a monotonically increasing chemical potential when increasing $-1/k_F a$, is washed out. On the other hand, and besides the experimental uncertainty of our data, we cannot expect a perfect collapse of the datasets on a unique curve. This owes to two effects, connected with the functional form of the Josephson coupling energy E_J: first, even for a homogeneous sample the transmission amplitude is not perfectly constant for a fixed $V_0/\bar{\mu}$ ratio. Second, and very importantly, E_J depends upon the condensed density n_c, rather than on the superfluid one. Since this sizably varies through the interaction crossover even at $T = 0$, ω_p

is not univocally determined by the ratio $V_0/\bar{\mu}$ only. Rather, we expect that, for fixed $V_0/\bar{\mu}$ values, the plasma frequency in the BEC limit may exceed the one obtained in the unitarity and BCS regimes. This is confirmed, at least qualitatively, by closely inspecting the Fig. 5.5(a) data: plasma frequencies measured in the deep molecular BEC regime (see e.g. red circles) lay systematically higher than those obtained for strongly interacting superfluids (see cyan data) at the same $V_0/\bar{\mu}$ value. Additionally, one can also notice how, for the fixed $z_0 \sim 0.03$ set in our measurements, the critical barrier height V_c beyond which dissipative currents are observed is reached before for BCS superfluids than for molecular BECs. Also this can be understood by recalling that a constant z_0 corresponds to a higher charging energy when the interaction parameter $-1/k_F a$ is increased.

I conclude this section by briefly discussing an interesting method we devised to experimentally determine the (trap averaged) chemical potential of our system based on a qualitative variation of the system dynamics as the barrier height is varied. This serves both to calibrate the barrier height V_0 once the chemical potential of the system is known, e.g. in the BEC limit or at unitarity, or vice-versa to obtain $\bar{\mu}(k_F a)$ once the barrier height is calibrated at one interaction strength. The reliability of this protocol has been successfully tested by comparing our data with numerical simulations based on the EFTM model discussed in Refs. [114, 144].
The idea is inspired by noticing, in the experiment, that the purely dissipative dynamics reported in Fig. 5.3(c) cannot be reached, for any z_0 value, if the barrier is lower than a particular height V_{ex}. In that case, a damped oscillation, rather than a purely exponential decay, characterizes $z(t)$, irrespective of the interaction strength. From the inspection of such a peculiar trend through the EFTM model, quantitatively accurate both to describe the system evolution in the BEC regime up to $k_F a \sim 1$ and to evaluate the bulk superfluid properties at equilibrium up to unitarity, it turned out that $V_{ex} = \bar{\mu}$ within a very few percent uncertainty, and irrespectively of the specific choice of initial imbalance $z_0 \geq 0.3$. As such, we could experimentally determine the value V_{ex} for different interaction strengths employing a very simple protocol which does not need to record a full $z(t)$ dynamics, but it relies on the measure of $z(t)$ only after half and one axial trap period, $t_1 = \pi/\omega_0$ and $t_2 = 2\pi/\omega_0$, respectively. Indeed, the purely dissipative regime is characterized by $z(t_2) < z(t_1)$, see e.g. Fig. 5.3(c), whereas a damped oscillation always yields $z(t_2) > z(t_1)$. Hence, V_{ex} can be experimentally identified as

the barrier height value at which $z(t_2) - z(t_1)$ reverts its sign. The reliability of this method throughout the crossover is testified by the comparison of the experimental data of V_{ex} (gray filled circles) with the trap averaged chemical potential obtained for a cloud at equilibrium via the EFTM model (blue empty circles), see Fig. 5.5(b).

5.3 Critical initial excitation and onset of dissipative currents

In the previous section I focused on the regime of small initial excitations, $z_0 \sim 0.03$, and discussed the system dynamics throughout the interaction crossover in terms of the experimentally measured plasma frequency. In the following I present the characterization of our JJ in the regime of large excitations, where dissipative currents develop at the start of the dynamics, adjoining the coherent superflow. This survey enabled to obtain, as a function of the barrier height and of the interaction parameter, the critical values z_c which delimit the transition from coherent to dissipative regimes of our junction. Additionally, combining the extracted values of z_c and of the previously discussed ω_p allowed to extract the maximum current of the weak link in a simple way, described in the following. In particular, the data acquired in the BEC regime have represented the basis for the theory-experiment comparison subject of the study reported in Ref. [6], done in collaboration with the group of Prof. N. Proukakis. While I refer to Ref. [6, 144] for a detailed discussion about the strong link between vortex ring nucleation and development of dissipative currents in our setup, here I mainly focus on the experimental aspects of such a study, that have been part of my research activity within my PhD.

The most straightforward method to determine the critical imbalance z_c, beyond which dissipation arises in our junction for different V_0 and $k_F a$ values, would be represented by the measure of several $z(t)$ evolutions, as those shown in the previous section, see Fig. 5.3. In practice, however, this strategy is very time-consuming and not really necessary. A much more convenient way to characterize the system is in turn offered by a three-point measurement of $z(t)$, very much connected with the determination of $\bar{\mu}$ discussed at the end of the previous section. Rather than sampling the whole dynamics,

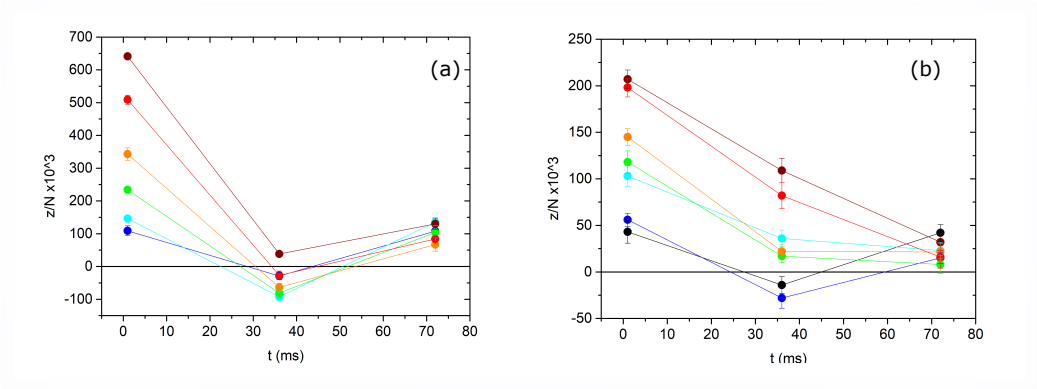

Figure 5.6: z recorded at $t = 0$, $T/2$ and T. Error bars corresponding to a statistics of 10-15 data per time. (a): $V_0 \sim 0.6\mu_0$ $(3\,mW)$. (b): $V_0 \sim \mu_0$ $(5\,mW)$. BEC regime.

we only recorded, for different barrier heights and interaction strength, $z(t_i)$ for $t_0 = 0$, $t_1 = \pi/\omega_0$ and $t_2 = 2\pi/\omega_0$. Fig. 5.6 shows examples of such measurements in the deep BEC regime for barrier heights $V_0 \sim 0.6\mu_0$ (Fig. 5.6(a)) and $V_0 \sim \mu_0$ (Fig. 5.6(b)), respectively.

Quite generally, see Fig. 5.3, the $z(t)$ dynamics can be approximated by the sum of three terms as it follows:

$$z(t) = z_c \cos(\omega_p t) + (z_0 - z_c)e^{-\Gamma t} + z_{off} \tag{5.11}$$

The first term accounts for the coherent Josephson dynamics, and ω_p stems for the plasma frequency that, for fixed barrier height, is largely independent from the specific z_0 value. The second term accounts for eventual dissipative currents, yielding an irreversible decay of the population imbalance only present if z_0 exceeds a critical value z_c. To a very good approximation, the normal flow can be described by an exponential decay with rate Γ. Finally, a nonzero z_{off} is introduced to account, eventually, for a small residual displacement of the axial trap barycenter, relative to the barrier position.
Based on such a trend, the quantities $z(0)$, $z_1 \equiv z(t_1)$ and $z_2 \equiv z(t_2)$ read, respectively:

$$\begin{aligned} z(0) &= z_0 + z_{off}; \\ z_1 &= z_0 e^{-\Gamma\pi/\omega_0} + z_c(\cos(\omega_p\pi/\omega_0) - e^{-\Gamma\pi/\omega_0}) + z_{off}; \\ z_2 &= z_0 e^{-\Gamma 2\pi/\omega_0} + z_c(\cos(\omega_p 2\pi/\omega_0) - e^{-\Gamma 2\pi/\omega_0}) + z_{off}; \end{aligned} \tag{5.12}$$

Obtaining a precise determination of Γ, ω_p and z_c from the three-point measure is clearly challenging with no additional external input. I therefore

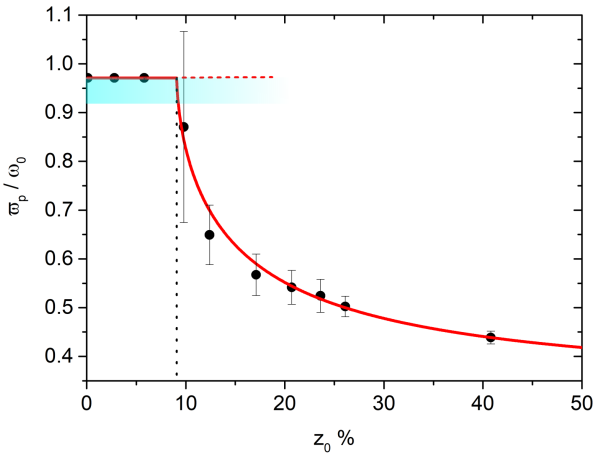

Figure 5.7: $\tilde{\omega}_p$ value as a function of the initial population imbalance z_0, for the case $V_0 \simeq 0.8\mu_0$. A fit (solid red) with relations (5.13) and (5.12) yields the interception point with the steady state result $\tilde{\omega}_p = \omega_p$ (dashed red) for small initial imbalances. The interception point corresponds to the critical value z_c (dotted black), beyond which dissipative currents emerge. The shaded region identifies the experimental confidence region for ω_p (lower fit curve in Fig. 5.5(b)).

proceeded to analyze the data by defining the following quantity from the experimental data:

$$\tilde{\omega}_p = \arccos\left(z_1/z_0\right) \cdot \omega_0/\pi \tag{5.13}$$

Irrespective of the specific interaction regime and barrier height, $\tilde{\omega}_p$ as a function of z_0 exhibits the peculiar trend shown in Fig. 5.7 for the case $V_0 \simeq 0.8\mu_0$ and $1/k_F a = 4.25$: for small excitations ($z_0 < z_c$), where dissipative currents are absent, $\tilde{\omega}_p$ does not vary with z_0, and it corresponds to the plasma frequency ω_p, discussed already in the previous section. In particular, the analysis presented in Fig. 5.5(a), obtained by tracking the full $z(t)$ evolution for small z_0 values, enables to identify a confidence interval for ω_p in the coherent regime, see shaded region in Fig. 5.7. As the imbalance is increased and a dissipative contribution is present (for $z_0 > z_c$), Eq. (5.13) yields by construction $\tilde{\omega}_p < \omega_p$. In this regime, the trend of the experimental $\tilde{\omega}_p$ can be nicely fitted (red solid curve) to Eq. (5.13), assuming z_1 to be given by Eq. 5.12. The intercept of the obtained fitting curve with the steady result $\tilde{\omega}_p = \omega_p$ allows then to identify the critical value z_c (and correspondingly Γ).

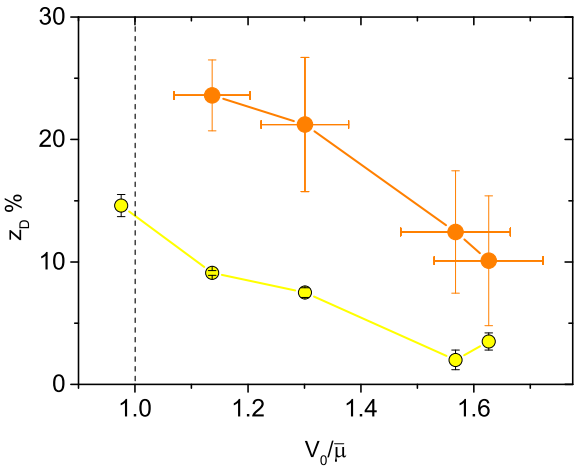

Figure 5.8: z_c (yellow dots) and z_{c2} (orange dots) as a function of the renormalized barrier height, at $1/k_F a = 4.25$. A dashed line indicates the condition $V_0 = \bar{m}u$, experimentally retrieved as explained in Sec. 5.2.

Additionally, as already mentioned when discussing the experimental determination of $\bar{\mu}$ via the study of the transmission dynamics at large excitations, for sufficiently high barriers a second critical imbalance z_{c2} exists, beyond which the superfluid junction undergoes a purely dissipative flow. Experimentally, this latter point can be identified via the three-point analysis by inspecting the trend of the following quantity:

$$\beta = \frac{z_2 - z_0}{z_1 - z_0} \tag{5.14}$$

It can be easily verified that, as long as the system features a coherent oscillation with $\omega_p \geq 0.75$ (see 5.5(a)), $\beta \leq 1$, whereas an overdamped flow yields $\beta > 1$. As such, also the second critical imbalance z_{c2} can be obtained via the three-point protocol, corresponding to the condition at which $\beta = 1$.
From this simple experimental protocol and data analysis I could therefore obtain the critical boundaries $z_c(V_0)$ and $z_{c2}(V_0)$ separating within the $V_0 - z_0$ plane the three regimes: coherent ($z_0 < z_c(V_0)$), coherent plus dissipative ($z_c(V_0) < z_0 < z_{c2}(V_0)$), and purely dissipative ($z_0 > z_{c2}(V_0)$).

Fig. 5.8 shows the outcome of such a characterization obtained for the deep BEC regime ($1/k_F a = +4.25$). Note that V_0 is here expressed in units

of the mean chemical potential $\bar{\mu}$. Focusing first on the trend of z_c (yellow dots), one can notice how for increasing barrier heights, the onset of dissipation is reached for smaller initial imbalances. This is consistent with the fact that the maximum Josephson current, proportional to the transmission amplitude, is strongly reduced as the $V_0/\bar{\mu}$ is increased: as such, a progressively smaller charging energy suffices to reach $\hbar I_c$ and trigger dissipative currents. In turn, z_{c2} (orange dots) is significantly larger than z_c for relatively weak barriers, and it approaches z_c only for $V_0/\bar{\mu}$ values significantly larger than one, although the experimental uncertainty is more sizable for the determination of this second boundary.
This trend imply that, although dissipative phenomena may be easily established upon increasing the initial charging energy stored across the junction, these do not completely wash out the relative phase relation between the two superfluid reservoirs over a large portion of the phase diagram. As detailed in Ref. [6] indeed, within the whole region comprised between z_c and z_{c2}, the irreversible flow is triggered by the propagation of vortex rings, nucleated within the barrier region via phase-slippage processes [113]. While these represent the microscopic channel through which the system can partially dissipate its excess initial charging energy, as soon as the population imbalance has dropped below z_c, undamped Josephson oscillations are reestablished, see Fig. 5.3(b). Only significantly higher excitations of the system induce a complete loss of coherence and a scrambling of the relative phase between the two reservoirs, preventing at any later time the possibility for a dissipationless flow across the weak link. The system dynamics in this latter regime still lacks a complete understanding, and it definitively deserves future investigations, both experimental and theoretical. In particular, although not discussed in this work, for $z_0 > z_{c2}$ we observed that the rate of vortex nucleation is strongly increased, possibly pointing to the development of a turbulent regime near the barrier region.

At unitarity, the experimentally determined phase boundaries z_c and z_{c2} in the $z_0 - V_0$ plane are presented in Fig. 5.9. Also in this case, the trends qualitatively resemble the ones discussed above for molecular BECs, z_{c2} greatly exceeding z_c and smoothly connecting to it only in the limit of very large barriers. Yet, some quantitative differences among the two interaction regimes are worth to be noticed: first, for fixed $V_0/\bar{\mu}$, the critical imbalance for the onset of dissipative currents is sizably reduced for crossover superfluids, relative to molecular BECs. This trend can be qualitatively understood by recalling that, for fixed barrier height-to-chemical potential ratio,

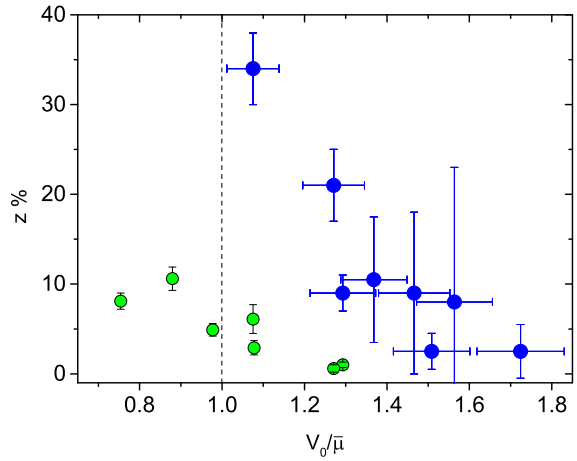

Figure 5.9: z_c (yellow dots) and z_{c2} (orange dots) as a function of the renormalized barrier height, at unitarity A dashed line indicates the condition $V_0 = \bar{m}u$, experimentally retrieved as explained in Sec. 5.2.

the maximum coherent current is mainly set by the condensate density, and not by the superfluid one, see Eq. (5.9a). This implies that for unitary superfluids, for which the condensate fraction is about $f_c \sim 0.5$ [149], the dissipative regime is reached for a lower charging energy (rescaled to the superfluid chemical potential). On the other hand, for fixed V_0 values, rather than fixed $V_0/\bar{\mu}$ ones, the unitary Fermi gas features a critical current substantially higher than the one of a weakly interacting BEC.
This quantitative difference is much less appreciable if we consider the second critical boundary z_{c2}: In this case, the two interaction regimes herein explored exhibit, within the experimental uncertainty, quite similar $z_{c2}(V_0/\bar{\mu})$ trends.

Finally, combining the experimentally extracted values of plasma frequency ω_p with the critical imbalance z_c I could also extract the critical current sustained by the junction. This was enabled by the analysis of numerical results, obtained through EFTM simulations carried in the BEC regime [6] by K. Xhani and N. Proukakis, which unveiled that the maximum coherent current can be excellently approximated, within a few percent

accuracy, by

$$I_{Max} = z_c \omega_p \frac{N}{2} \tag{5.15}$$

Given that in the BEC limit the numerical simulation is able to quantitatively reproduce the observed $z(t)$ dynamics both in the coherent and dissipative regimes, see insets of Fig. 5.10(a), and correspondingly to obtain critical boundaries $z_c(V_0)$ that match experimental data remarkably well (see main panel Fig. 5.10(a)), I applied Eq. 5.15 to obtain the experimental maximum Josephson current. The resulting trend is presented in Fig. 5.10(b), together with the result of the EFTM model for both zero and finite temperature samples. In both panels, the barrier height is normalized to the peak chemical potential which for $T > 0$ includes the thermal mean-field contribution [150], see supplementary material in Ref. [6].
From the analysis of the numerical results, it is interesting to mention that the $z_c(V_0)$ boundary was found to be robust up to temperatures $T \sim 0.3T_c$ upon keeping the *condensate* number equal to the T = 0 case in the simulation, see Fig 5.10(a)) [6].

As the maximum current is concerned, see Fig. 5.10(b), the I_{Max} constructed from the experimentally determined z_c and ω_p reveals excellent agreement with the EFTM result. In addition and quite remarkably, both numerical and experimental data are quantitatively reproduced by the analytic model introduced in the previous section 5.1, see again Eq. (5.9a) and (5.10), once the Gaussian barrier and the inhomogeneous density distribution are taken into account. In particular, such a simple analytic model appears able to reproduce I_{Max} quantitatively down to relatively low barrier heights, $V_0/\mu_0 \sim 0.7$, provided that second order contributions are explicitly considered.
Therefore, besides representing the testbed for the numerical study detailed in Ref. [6], the outcome of the experimental survey discussed in this work has also enabled to successfully benchmark the analytic theory of Ref. [136].

Finally, although the estimate of the maximum current based on z_c and ω_p has been tested to be valuable only in the BEC limit of the crossover via the EFTM simulation, in Fig. 5.11 I present the same analysis on CO data (red circles), together with the analytic prediction based on Ref. [115] including both first and second order contributions (red solid line). Dashed lines indicate the theoretical prediction when a $\pm 5\%$ uncertainty on the chemical potential is assumed. Interestingly, also in this case the agreement between

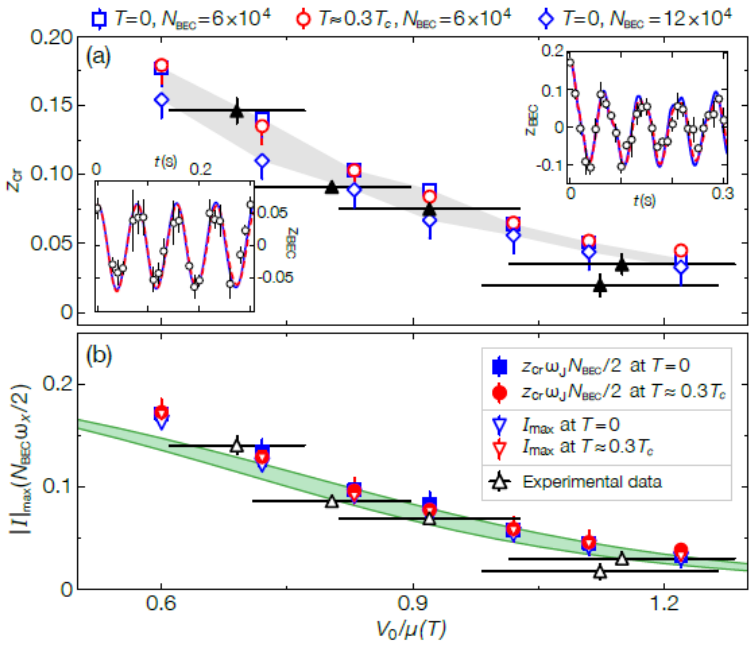

Figure 5.10: Comparison of experimental results with numerical GPE simulations. (a): critical population imbalance z_c from experimental results (black triangles), and simulation results for $T = 0$, $N = 6 \times 10^4$ (blue squares), $T = 0$, $N = 12 \times 10^4$ (blue diamonds), and $T = 0.3T_c$, $N = 6 \times 10^4$ (red circles). (b): maximum coherent current I_{Max} from experimental results (white triangles), and simulation results for $T = 0$ (blue triangles) and $T = 0.3T_c$ (red triangles). The approximated numerical results $I_{Max} = z_c\omega_p N/2$ are also shown in figure for $T = 0$ (blue squares) and $T = 0.3T_c$ (red circles). Vertical error bars account for the discreteness of the numerically-probed z_0 values for numerical results, to the fit uncertainties on z_c and ω_p for experimental results. V_0 on the abscissa is here rescaled to the $T = 0$ chemical potential μ; error bars on experimental data accounts for uncertainties on barrier width, laser power and particle number. Green shaded area: prediction of the analytical model proposed in Ref. [115] including second order contribution (green shaded area).

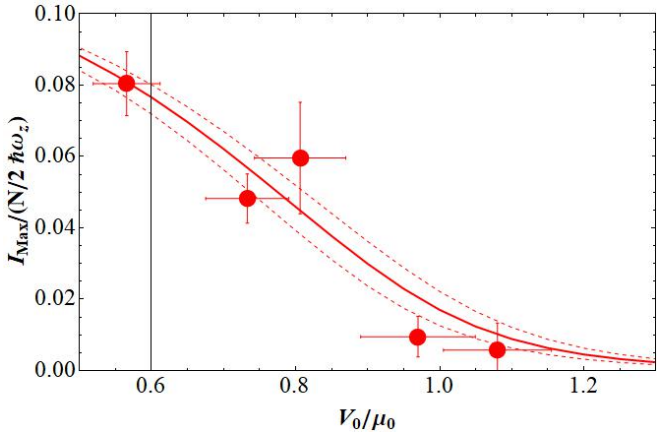

Figure 5.11: Maximum coherent current derived from the experimental values of z_c and ω_p, as from Eq. (5.15), compared to the analytical prediction based on Ref. [115] including both first and second order contributions (red solid line). The confidence region delimited by dashed lines accounts for $\mp 5\%$ uncertainty on the peak chemical. Here, a condensed fraction $f_c = 0.51$ was assumed, on the basis of the results in Ref. [149].

theoretical and experimental results suggests such an estimate of I_{Max} to hold. In particular, the theory appears to match the data within experimental uncertainty for a condensed fraction $f_c \sim 0.47(4)$. This value, significantly smaller than the mean field result (yielding about $f_c \sim 0.7$), appears in good agreement with the expectation from self-consistent T matrix calculations and Monte Carlo results [149]. Such a sizable reduction of the density of condensed pairs, relative to the strong attraction BEC regime, is responsible for the decrease in the observed I_{Max} for unitary Fermi gases, relative to molecular BECs, at fixed $V_0/\bar{\mu}$ values of the barrier height.

To conclude, in spite of the fact that more targeted and precise investigations of I_{Max} for crossover superfluids are desirable, the experimental results obtained in my thesis work already outline how the study of the Josephson effect represents a unique probe for the condensed fraction in strongly correlated superfluids, which in turn, towards the BCS limit of the crossover, is intimately linked to the superfluid gap, see e.g. [151, 152].

Conclusions and next future perspectives

In this thesis I have presented the realization of a new experimental apparatus aiming to produce a novel ultracold mixture of lithium and chromium fermionic atoms.
In particular, I have described in details the design of the overall vacuum system, and the assembly and bake-out procedures of its various components. I have also presented the design and realization of the overall coils setup installed onto the apparatus, which provides the magnetic field profiles exploited to cool and trap the atoms and, in the future, to tune the inter-atomic interactions through the Feshbach resonance phenomenon.
During my PhD activity, I also designed and implemented the optical setup exploited to laser cool ^{6}Li atoms, as well as both the bosonic ^{52}Cr and fermionic ^{53}Cr isotopes. The detailed description of the overall laser system is also reported in this thesis.
During the last year, we also designed and implemented a totally passive and inexpensive scheme for a high-power bichromatic optical dipole trap free of thermal-lensing effects. The performances of the resulting trapping beam are discussed in Ref. [5], reported in Appendix C.

The construction of the experimental apparatus is now complete, and we could recently test and optimize experimental routines to produce single and double species MOTs of fermionic ^{6}Li atoms and bosonic ^{52}Cr atoms.
I have provided in this thesis the characterization of our Li MOT loading efficiency as a function of the various experimental settings. The results of this characterization yield an optimum loading rates of about $4 \times 10^{9}\ s^{-1}$, and a final peak density on the order of $5 \times 10^{11}\ cm{-}3$. These results were obtained exploiting only the D2 laser light. Furthermore, I have shown the

first results attained through the implementation of a gray-molasses cooling stage operating on the D1 atomic transition, which allowed us to reach sub-Doppler temperatures within our Li atomic clouds.
This thesis also presents the optimization of the Cr MOT loading efficiency, which leads to optimum loading rates of about 6×10^7 atoms/s, and a final peak density of 1.3×10^{11} atoms/cm^3. The characterization probed the very fast saturation times (~ 130 ms) expected in Cr MOTs owing to a very high light-assisted collision rate, together with the decay processes into D metastable states, which drives the atoms out of the cooling transition. The Cr atoms occupying the high-field-seekers Zeeman levels of these metastable states are magnetically trapped by the quadrupole MOT field during the loading procedure. The characterization of the loading rates and decay times featured by these magnetically trapped clouds are also reported in my theis work.
Finally, I have discussed the first experimental investigation of dual species clouds of ^{6}Li and ^{52}Cr atoms. I have shown the characterization of the loading efficiencies and lifetimes featured by the magnetically trapped clouds of Cr atoms within D metastable states in presence of Li MOTs. The main outcome of this experimental study is the demonstration of the possibility to load and trap up to $\sim 3 \times 10^7$ Cr atoms in presence of Li MOT clouds. The outcome of our studies will be subject of a publication currently in preparation.

As part of my PhD activities, I also presented the analysis of unpublished data on ^{6}Li superfluid mixtures at the BEC-BCS crossover, which I carried on in parallel with the work described above. The measurements investigate the superfluid and dissipative currents across a thin optical barrier connecting two superfluid reservoirs. This study investigated different configurations of barrier heights and initial energy mismatch, enabling to extract the critical values of imbalance beyond which dissipative dynamics is observed. The related phase diagram was obtained both in the BEC and the crossover regimes. We collaborated with the theoretical team of Prof. N. Proukakis in Newcastle to provide a direct comparison of my experimental BEC results with numerical simulations, which is the subject of the work in Ref. [6]. Very interestingly, my results continuously connect the hydrodynamic regime at low barrier heights, where the superfluid flows in presence of a small obstacle, up to the tunneling regime, where the barrier height exceeds the chemical potential of the superfluid. The crossover from one

regime to the other can be described by accounting for second order effects on the Josephson dynamics, following the predictions of a theoretical model developed within a tunneling Hamiltonian formalism [136].

The work discussed in this thesis paves the way to interesting perspectives. As the Cr-Li mixture is concerned, we are currently attempting to create a ^{53}Cr MOT, optimizing an optical pumping scheme at the transverse cooling stage that should enable us to considerably increase the flux of fermionic chromium in the Zeeman slower. Once a ^{53}Cr MOT will be realized, we will characterize the collional stability of the Fermi-Fermi mixture in the cold regime, by following experimental protocols analogous to the ones detailed in this thesis for the ^{52}Cr-^{6}Li Bose-Fermi case. The outcome of this study will allow to devise the best strategy to produce a double species mixture ^{53}Cr-^{6}Li at few hundreds of μK. At this point, by optimizing the loading of the atomic clouds into our newly-created bichromatic potential, we will perform the first tests of evaporative and sympathetic cooling of the two isotopic combinations, following an all-optical approach that turned out being successful to reach quantum degeneracy both for the K-Li and the K-Dy cases [99,100,153–155]. Parallel to this, by following already well established strategies, such as loss spectroscopy and cross-thermalization measurements, we will proceed with a thorough investigation of Feshbach resonances, both inter- (Cr-Li) and intra- (Cr-Cr) species. In particular, the inter-species resonances are to date totally unknown for both isotopic mixtures. Therefore, the outcome of this study will enable to develop and optimize multi-channel calculations for this novel system, as well as to pinpoint the most favorable resonances to be employed for future few- and many-body surveys. To this end, the parallel investigation of intra-species resonances between spin-polarized ^{53}Cr atoms, presently known only via a mass-scaling procedure based on ^{52}Cr resonance data [156,157], will allow to identify those magnetic field regions in which Cr-Li interactions can be controllably tuned without simultaneously modifying the intra-species scattering properties via undesired Cr-Cr resonances.

Concerning the investigation of critical currents in lithium Fermi superfluids started within this thesis work, in the future it will be interesting to obtain more precise data for the maximum Josephson current throughout the crossover region, and for the normal state conductance associated with the dissipative currents. To this end, the implementation of tailored optical potentials via a digital micro-mirror device (DMD) combined with a high resolution imaging system appears as an appealing possibility: On

the one hand, this will naturally enable to investigate in the experiment the Josephson dynamics as a function of the barrier parameters and geometry. Furthermore, the DMD may also allow for the controlled imprinting of a relative phase across the weak link, which should enable to obtain, throughout the crossover region, a direct measurement of the current-phase relation of our junction. In turn, this will serve to benchmark current and future theories for the transport phenomena of crossover superfluids, and to extract precise information about elusive bulk properties of such systems, primarily of the condensate fraction. Finally, such studies, so far carried on three-dimensional balanced samples, could find very appealing extensions once low dimensional (2D or 1D) and asymmetric ($E_{F,\uparrow} \neq E_{F,\downarrow}$) were considered. In particular, it would be extremely interesting to implement such experimental protocols to the case of mass-imbalanced Fermi superfluids of Cr-Li pairs, the Josephson effect representing a sensitive probe for revealing exotic superfluid states [158, 159].

Appendix A

Design of Lithium Zeeman Slower

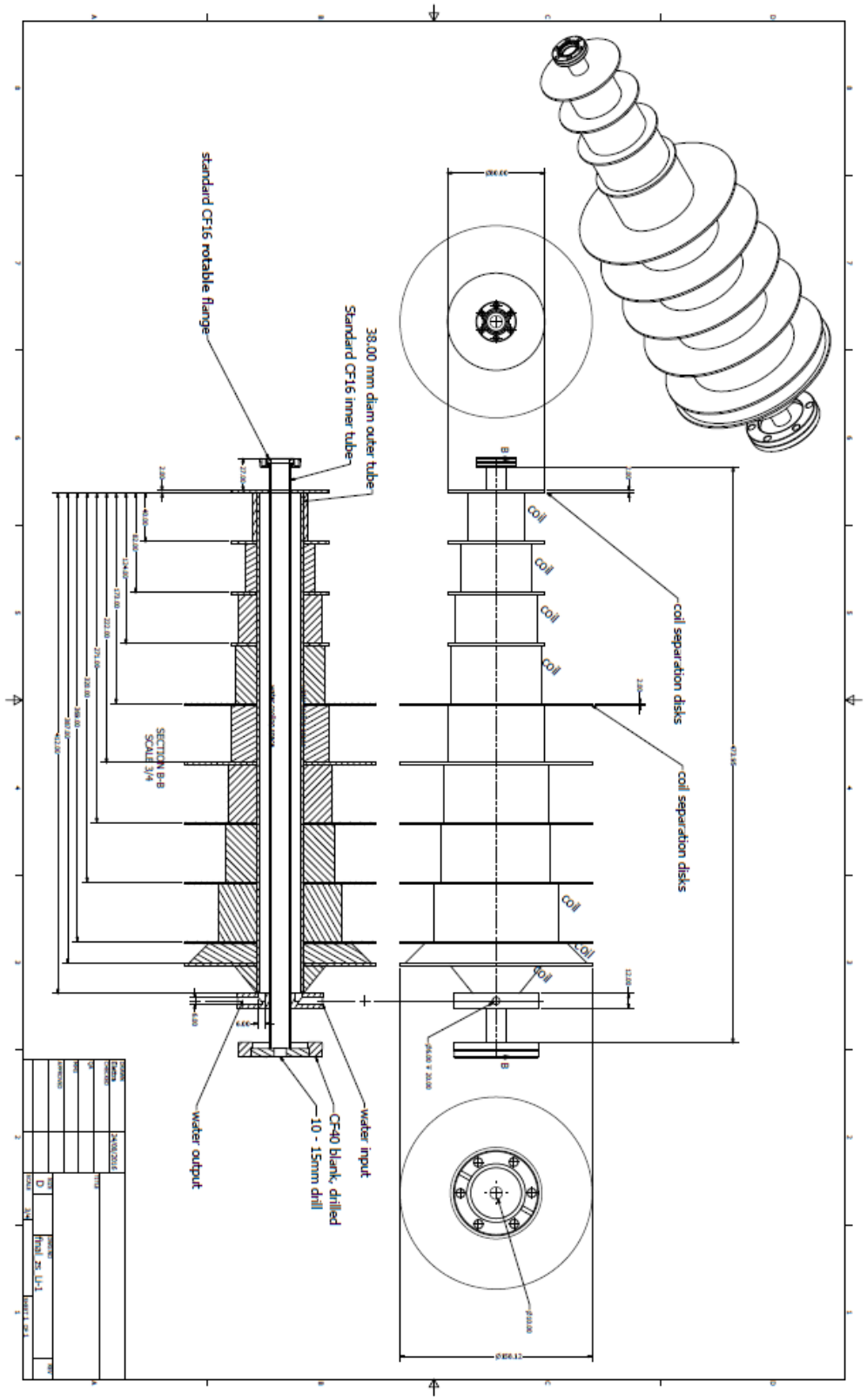

Figure A.1: Design of Lithium Zeeman Slower.

Appendix B

Design of water cooling case for Feshbach coils

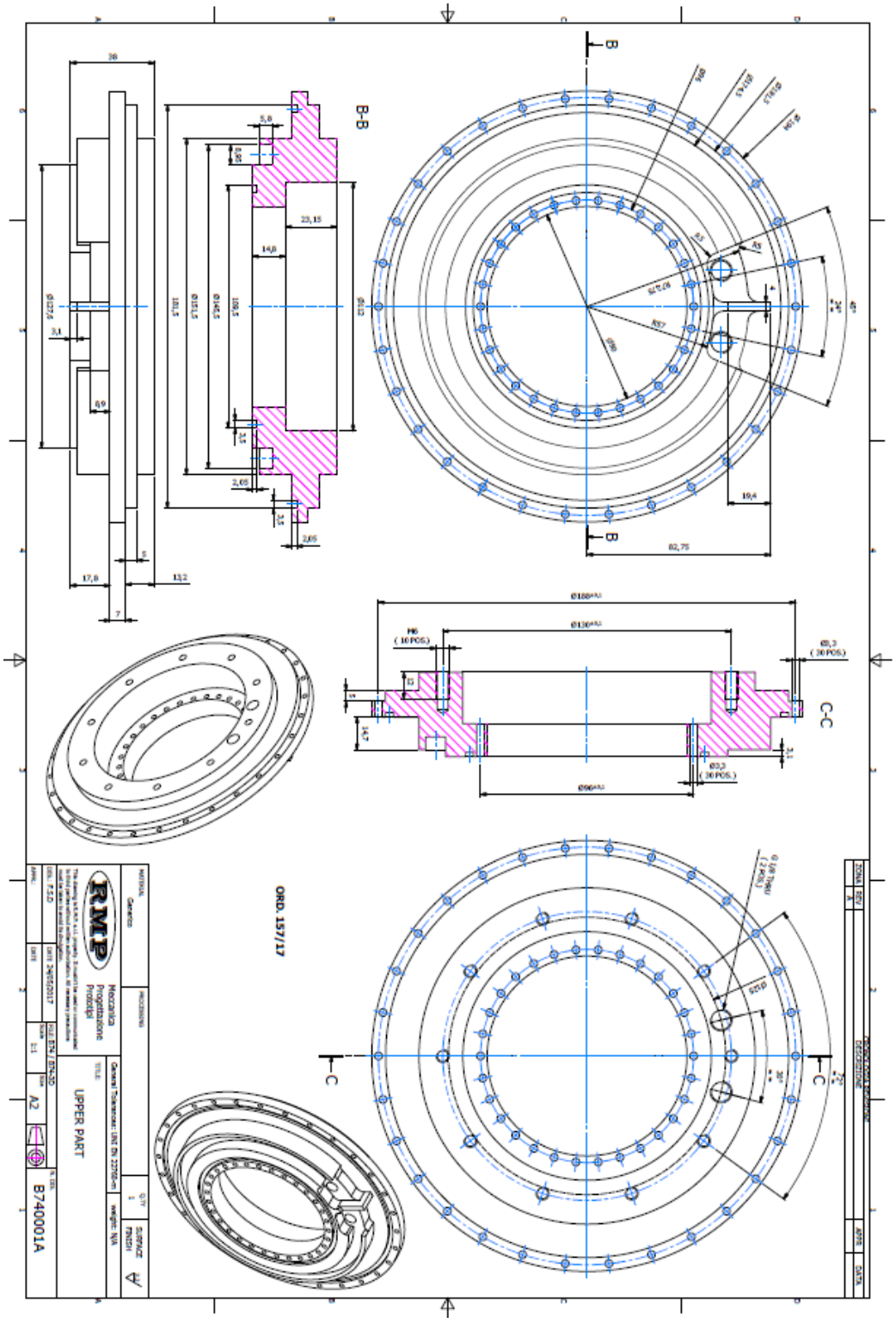

Figure B.1: Design of Feshbach water cooling case. Top part.

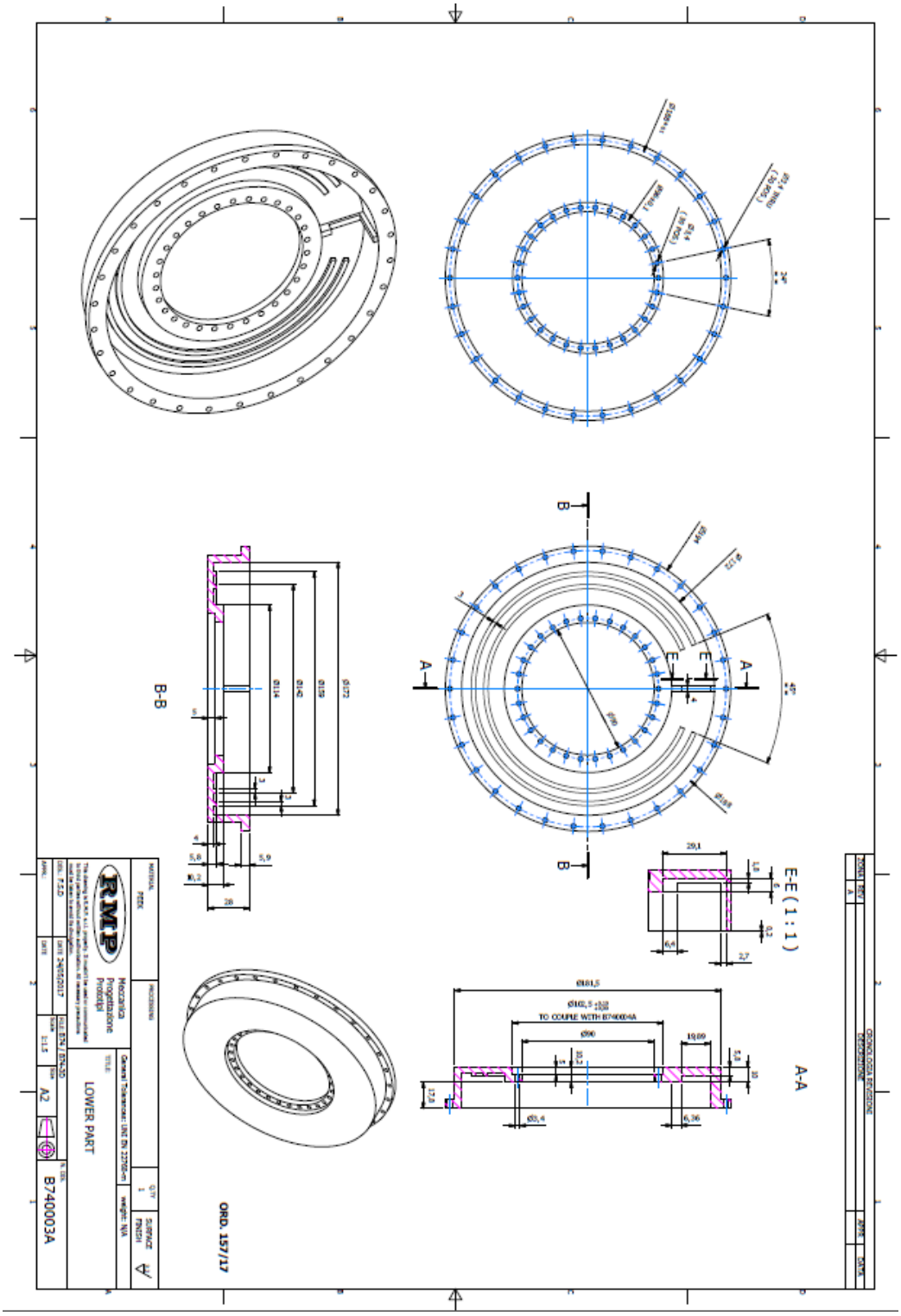

Figure B.2: Design of Feshbach water cooling case. Bottom part.

Appendix C

Realization of a high power optical trapping setup free from thermal lensing effects

Realization of a high power optical trapping setup free from thermal lensing effects

C. Simonelli,[1,2*] E. Neri,[1,2] A. Ciamei,[1,2] I. Goti,[2] M. Inguscio,[1,2] A. Trenkwalder,[1,2] and M. Zaccanti [1,2]

[1] *Istituto Nazionale di Ottica del Consiglio Nazionale delle Ricerche (INO-CNR), 50019 Sesto Fiorentino, Italy*
[2] *LENS and Dipartimento di Fisica e Astronomia, Università di Firenze, 50019 Sesto Fiorentino, Italy*
[*] *simonelli@lens.unifi.it*

Abstract: Transmission of high power laser beams through partially absorbing materials modifies the light propagation via a thermally-induced effect known as thermal lensing. This may cause changes in the beam waist position and degrade the beam quality. Here we characterize the effect of thermal lensing associated with the different elements typically employed in an optical trapping setup for cold atoms experiments. We find that the only relevant thermal lens is represented by the TeO_2 crystal of the acousto-optic modulator exploited to adjust the laser power on the atomic sample. We then devise a simple and totally passive scheme that enables to realize an inexpensive optical trapping apparatus essentially free from thermal lensing effects.

1. Introduction

The precise focusing of a high power laser beam on a target sample is highly relevant both for fundamental science and for a variety of industrial and medical applications: from the realization of optical tweezers [1] and traps [2] for atoms and molecules, to the exploitation of high power laser sources for cutting, welding, drilling and surface treatment of various materials, to laser-based surgery and ophtalmology. Quite generally, many applications require the optical power to be controllably tuned, e.g. to enable evaporative cooling of atomic gases in dipole traps, or to avoid undesired damage of the illuminated sample. In combination with a high level of optical power, this makes such applications of laser technology not immune from the so-called thermal lensing, or thermal blooming, effect [3–6]. Such a phenomenon arises from the fact that both the substrate and coating of any element composing an optical setup unavoidably absorb part of the incident light. As a consequence, the non-uniform intensity profile of the impinging beam acts as an inhomogeneous heat source for the optical material. Given that the index of refraction inherently features some temperature dependence, the illuminated optical component acts like a lens on the transmitted beam [3, 7], making both the size and the location of the beam waist time- and intensity-dependent quantities. Although thermal lensing effects can be in some cases mitigated by exploiting materials with low absorption coefficients at the laser wavelength of interest, any optical component has inherently an associated thermal lens [8], which may cause relevant modifications of the beam properties, especially for those instances where stable positioning of the waist is requested at the micro-scale.

In the context of cold gases experiments, high power optical dipole traps (ODT) are routinely employed to confine and manipulate samples of single atomic species or of binary mixtures that cannot be efficiently cooled within magnetic potentials. Celebrated examples are the case of lithium atoms, see e.g. Refs. [9–11], and of lithium-potassium mixtures [12, 13]: there, an all optical approach is extremely convenient, as it can be employed in combination with external magnetic fields that enable the controlled tuning of the interactions via the Feshbach resonance phenomenon [14]. On the other hand, laser sources, generally in the near infrared wavelength regime, delivering powers up to a few hundreds of Watts are unavoidably required to ensure a

large trapping volume and trap depths sufficiently high to confine laser-cooled atomic samples delivered by standard magneto-optical traps (or optical molasses) at few hundreds (tens) of μK. While thermal lensing does not prevent to reach high efficiencies in confining and manipulating single species within monochromatic traps, it may become a severe limitation in experiments where heteronuclear mixtures or bichromatic potentials are employed, see e.g. Refs. [13, 15–18]. In the former case, owing to the different polarizabilities of the two atomic species, thermal lensing may induce out-of-phase sloshing of the two clouds within the trap, hence reducing the efficiency of the evaporative and sympathetic cooling stages. In the latter case, in which the optical potential is realized by superimposing waists of laser beams at different wavelengths, thermal effects may result in an uncontrolled variation of the overall trapping landscape, given that absorption might strongly vary with the frequency of the laser source. As a consequence, devising schemes to limit, and possibly cancel, thermal lensing effects might significantly increase the performances of cold gases machines based on all-optical approaches.

In this paper we provide a simple and inexpensive strategy to realize a deep dipole trap immune from thermal lensing. This is based on a completely passive setup realized with a 300 Watt laser source at 1070 nm and standard optical elements. First, we characterize the power of the thermal lens associated with each optical component (lenses, windows, acousto-optic modulator) generally employed within an optical trapping setup. From such a study we conclude that: (i) fused silica lenses and windows with standard anti-reflection coating can be safely used up to powers of several hundreds of Watts, yielding little or no difference with respect to much more expensive elements, such as those based on $Suprasil^{®}$ substrates; (ii) the only significant thermal lens in the setup is provided by the TeO_2 crystal of the acousto-optic modulator (AOM), that represents a typical option to enable the active tuning and control of the laser power on the atomic sample. Second, we devise, implement and successfully test an optical scheme that allows to precisely cancel the effect of the AOM thermal lens, simply by adjusting the crystal position relative to a focus within the optical path. We anticipate that, although the present work is primarily targeted to the optical trapping of cold atomic clouds, our study might be straightforwardly extended to any other setup which requires to position the waist of high power lasers on a target sample with a few micron accuracy.

This article is organized as it follows: Section 2 provides a basic theoretical background to the thermal lensing phenomenon. Section 3 presents a characterization of the thermal lenses associated with the various optical elements employed within a typical optical trapping setup for cold atoms experiments. Finally, Section 4 describes the simple optical scheme we devised to get rid of thermal lensing effects, and the characterization of the resulting ODT beam.

2. Theoretical background

Since 1965, thermal lensing effects [3] and more generally thermally induced wavefront distortions in high-power laser systems have been extensively investigated [4–6]. As already anticipated, such a phenomenon originates from the local heating caused by the transmission of a laser beam inside an optical element, which acts as a partially absorptive medium. Owing to the temperature dependence of the refractive index of the medium, the optical path experienced by the beam is modified in connection with the spatially inhomogeneous temperature distribution within the optical component, which acts as a "thermal lens" for the beam propagation, see Fig. 1(a). Such a phenomenon encompasses a wide class of research fields and optical setups, spanning from high-energy laser physics to biological and material sciences. While thermal lensing may enable to devise various types of imaging techniques, such as the photo-thermal or thermal lens spectrometry employed for single-molecule detection of non-fluorescent compounds [19, 20], it is generally an undesired effect in all cases where optimal beam profile quality of high-power lasers is sought [21, 22].

Depending on the medium, thermal lensing can originate from different mechanisms, including

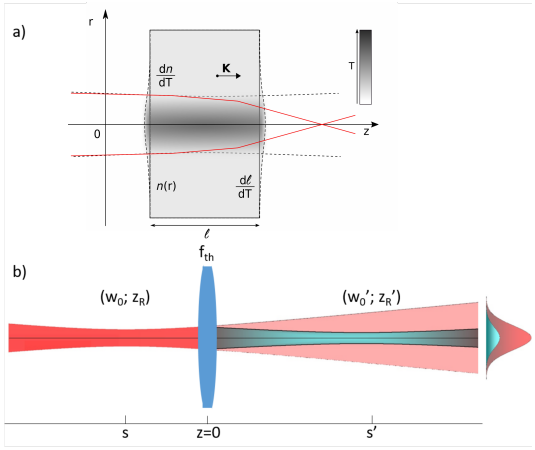

Fig. 1. **a)** Schematic visualization of thermal lensing of a Gaussian beam. Transmission of a laser beam through a partially absorbing medium of thickness ℓ, and characterized by an absorption coefficient b, locally heats up the material at a rate set by its thermal conductivity κ. The Gaussian profile of the beam induces a temperature gradient that changes the refractive index, and hence the beam path, according to the temperature dependence dn/dT of the substrate. Thermal expansion $d\ell/dT$ and strain dependence of the refractive index can further change the direction of wave propagation (**k**) in the medium, which acts as a thin, weak lens. **b)** Sketch of a thin lens f_{th} positioned along the path of a Gaussian beam. The propagation of the incoming beam, characterized by a waist w_0 (and Rayleigh length z_R) placed at a distance s from the lens, will be modified by f_{th}, that will create a new real (virtual) waist w_0' at a distance $s' > 0$ ($s' < 0$) from the lens, according to Eq. (2). The sign convention for the object (image) position follows the one of ray optics: $s > 0$ ($s' > 0$) indicates a position on the left (right) of the lens plane.

thermal expansion of the material, strain and temperature dependence of the refractive index. This makes an effective description of the thermal lens associated to a generic system highly non-trivial. However, for optical materials such as quartz, fused silica or BK7 glass, and even more so for high purity optics with high damage thresholds, thermal lensing effects can be ascribed to the sole temperature dependence of the refractive index, dn/dT. In that case, neglecting contributions associated both with the volume expansion and mechanical stress of the material [23], and with the coating film deposited on the substrate [7, 24], thermal lensing of an optical element is quantified in terms of a thermal focal length f_{th} that can be expressed for a Gaussian beam as [8]:

$$f_{th} = \frac{2\pi\kappa}{1.3b(dn/dT)\ell}\frac{w^2}{P} \equiv \frac{1}{m_0}\frac{w^2}{P} \tag{1}$$

Here P and w denote, respectively, the beam power and waist at the position of the optical component. κ represents the thermal conductivity of the material, b its absorption coefficient, dn/dT yields the temperature dependence of the refractive index, and ℓ the thickness of the medium. Namely, the optical element inducing thermal lensing can be considered as a thin lens whose focal length scales inversely with the incident intensity $I = 2P/(\pi w^2)$, with a proportionality constant m_0 that depends on the specific properties of the substrate. In particular, from Eq. (1) one can see that for a given light intensity impinging on an optical element, f_{th} will be larger, hence thermal lensing effects will be weaker, for those substrates that are thin, that feature low absorption and high thermal conductivity, with a refractive index weakly varying with temperature.

In order to gain an intuitive picture of thermal lensing effects within a generic setup, and to understand how they can be possibly cancelled out, it is useful to recall how a thin lens modifies the properties of an incident Gaussian beam [25]. Given an incoming beam featuring a waist (Rayleigh length) w_0 ($z_R = \pi w_0^2/\lambda$) at a distance s from a thin lens of focal length f_{th}, see sketch in Fig. 1(b), the focusing element will create a new waist w_1 at a distance s', according to the following relations:

$$s' = \frac{\frac{z_R^2}{f_{th}} - s(1 - \frac{s}{f_{th}})}{\frac{z_R^2}{f_{th}^2} + (1 - \frac{s}{f_{th}})^2} \tag{2a}$$

$$\frac{w_1}{w_0} = \frac{1}{\sqrt{(1 - s/f_{th})^2 + (z_R/f_{th})^2}} \tag{2b}$$

From these relations, then, one can immediately notice the following facts: First, for $f_{th} \to \pm\infty$ $s' = -s$ and $w_1 = w_0$, i.e. the beam will not be modified. Second, for any finite value of f_{th}, a new (real or virtual) beam waist will be created at a position that depends both upon the distance s of the lens from the first waist, and on the initial beam parameters. As a consequence, the radius of curvature of the incoming beam, $R_0(z) = (z + s)(1 + (\frac{z_R}{z+s})^2)$, will be modified according to $R(z) = (z - s')(1 + (\frac{z_R^{'}}{z-s'})^2)$ along the subsequent optical path. As a consequence, the far field intensity distribution of the beam will vary, enabling to quantify thermal lensing effects, for instance by measuring the change of the relative power transmitted through a slit placed behind the thermal lens, as a function of the incident power [6]. Alternatively, thermal lensing effects can be precisely characterized by coupling the beam to an optical cavity [8]: The presence of thermal lenses along the beam path will be reflected into a sizable change in the coupling efficiency to the different cavity eigenmodes. These or similar techniques allow to retrieve the values of f_{th} and m_0 associated with a given optical element, see Eq. (1), with no need to rely on a precise knowledge of the material properties.

Finally, in light of the forthcoming discussion in the next sections, it is useful to consider Eq. (2) in the special case $s = 0$, i.e. when the input beam waist lays on the plane of the thermal lens. In this case, the position and size of the new waist become, respectively:

$$s' = \frac{\frac{z_R^2}{f_{th}}}{1 + \frac{z_R^2}{f_{th}^2}} \tag{3a}$$

$$\frac{w_1}{w_0} = \frac{1}{\sqrt{1 + (\frac{z_R}{f_{th}})^2}} \tag{3b}$$

One can notice that, if $|f_{th}| \gg z_R$, by positioning the thermal lens in the beam focus the light propagation is modified only within a very small region behind the lens plane, while being unaffected at larger distances, since $s' \sim z_R^2/f_{th}$, and $w_1 \sim w_0$ up to corrections of the order of $(z_R/f_{th})^2$. Correspondingly, it is easy to check that the radius of curvature of the outgoing beam will coincide with the one of the incoming beam at all distances, aside for $O(z_R^2/|f_{th}|)$ corrections. Namely, whenever $|f_{th}| \gg z_R$, thermal lensing can be efficiently canceled by placing the substrate within a focus of the incoming beam, as one can infer from previous studies [6, 19, 26]. As it will be discussed more in detail in Section 4, this observation sets the basis for devising an optical trapping setup free from thermal effects.

3. Characterization of thermal lensing within a model setup

A prerequisite to minimize thermal lensing within a generic optical setup is to identify the main sources of such an effect by estimating the f_{th} associated with each optical element traversed by the laser beam. Since any material unavoidably introduces some degree of thermal phase aberrations, when designing a high-power optical setup it is in general desirable to minimize the number of components the laser beam has to pass through. For this reason, our optical dipole trap design employs as few optical elements as possible to adjust the beam power and waist on the atoms: Neglecting all reflective elements, our design (see sketch in Fig. 2(a) is solely composed by three lenses, one AOM and the quartz window of the vacuum chamber, within which the atomic clouds are produced.

The ODT light source is provided by a $YLR-300$ multimode fiber laser module by IPG Photonics delivering up to 300 W output power. The central emission wavelength is 1070 nm and the output beam is excellently fitted by a 2D Gaussian profile, characterized by a beam waist is of $w_0 = 2.21(1)$ mm with negligible ellipticity. Due to the clear aperture of the AOM of about $2.5 \times 1.75\,\mathrm{mm}^2$, two lenses are employed to de-magnify the beam waist down to about 550 μm. The first order diffracted beam of the AOM is then re-expanded in order to obtain a waist $w_3 \simeq 2200\,\mu$m on the last lens $f_3 = 250$ mm, employed to focus the beam down to a waist of about $w_{at} \simeq 45\,\mu$m on the atomic cloud after passing through the vacuum chamber window. All lenses employed in our design are one inch UV fused silica elements with anti-reflection V-coating at 1064/532 nm[1]. These represent a cheap, convenient option for high power applications, due to a very small $dn/dT \simeq 12 \cdot 10^{-6}\,\mathrm{K}^{-1}$ [27] and a low thermal expansion coefficient $\alpha \simeq 0.5 \cdot 10^{-6}\,\mathrm{K}^{-1}$ [28]. The $CF-40$ window of the vacuum chamber is instead made by a 3.3 mm thick quartz substrate with custom anti-reflection coating [2]. Finally, the AOM is realized by a 31 mm thick TeO_2 crystal [3].

3.1. Methods

As already discussed in the previous section, one method to measure the thermal lens of an optical element is to monitor the beam divergence behind it. This can be done by inspecting how the axial intensity profile of the outgoing beam

$$I(z, z_0) = I_0\left(\frac{w_0}{w(z)}\right)^2 = \frac{I_0}{1 + \left(\frac{z-z_0}{z_R}\right)^2} \tag{4}$$

depends upon the power impinging on the substrate. Here I_0, w_0 and z_0 denote the maximum intensity, the waist size and position, respectively, all affected by the specific thermal lens of the examined optical element. For the case of one single lens along the optical path, the axial intensity profile for a given power level can be measured by focusing the beam on a CCD camera, moved along the propagation axis through a translation stage. For each z position, the intensity $I(z)$ can be then obtained as the amplitude of the laser spot, extracted from a two-dimensional Gaussian fit. For the case of several elements, the generalized scheme depicted in Fig. 2(a) can be employed.

In spite of the conceptual simplicity of this method, we emphasize that special care must be taken to avoid systematic effects connected with the need to attenuate the beam intensity on the detector. While beam powers exceeding 100 W are needed to reveal sizable thermal aberrations induced by the optical elements composing our setup, already a few milliwatts saturate the CCD camera chip. This implies the need of a filtering stage, whose associated thermal lens can easily invalidate the whole measurement. To this end, we found that a filtering stage that limits

[1] UVFS YAG-ML lens by $Thorlabs$

[2] AR-coating 426 nm + 532 nm + 630 − 675 nm + 1064 nm/0° by *LaserOptik Garbsden*

[3] 3110 − 191 by *Gooch&Housego*

additional strong thermal aberrations can be realized by first sending the high power beam to a $BSF10-C$ coated beam sampler, from which a beam with power lower than 10 W is derived. After this point thermal effects are negligible, and a second attenuation stage can be safely obtained by letting the beam cross a high-reflection mirror before hitting the CCD sensor. Yet, the thermal lens of such attenuation stage remains significant when considered in combination with optical elements featuring very long f_{th}.

By employing such a simple setup we recorded, for various laser power levels and different combinations of optical elements, the corresponding axial intensity profiles which, fitted to the trend given by Eq. (4), provided the focus position, with an uncertainty essentially dominated by the intensity fluctuations of the spot on the CCD camera. Thermal lensing of the elements placed within the beam path was then quantified in terms of the shift Δz_{th} of the focus location z_0, relative to the one recorded under low power conditions. We underline that, owing to the minimum time resolution of our CCD camera, $\delta t = 50\,\mathrm{ms}$, we did not attempt a dynamical characterization of thermal lensing, and all the data reported in the following have been recorded in stationary conditions.

3.2. Results

First of all, we looked at the thermal lens associated with one single fused silica lens $f_1 = 200\mathrm{mm}$ placed in front of the laser output, at a distance $L_1 = 60(5)\,\mathrm{mm}$, much smaller than the Rayleigh length associated with the output waist $w_1 \simeq 2.2\,\mathrm{mm}$. By following the scheme previously described, we measured the shift Δz_{th} of the focus position, relative to the location of a low power ($P < 10\,\mathrm{W}$) beam. The resulting trend, recorded as a function of the incident power, is presented in Fig. 2(b) as yellow circles. As one can notice, thermal effects associated with f_1 together with the filtering stage cause only very small shifts of the focus position, Δz_{th} remaining below 80 μm up to the highest power of 280 W (intensity of about $3.7\,kW/cm^2$).

By following a similar procedure, we quantified the thermal lens generated by two lenses $f_1 = 200\,\mathrm{mm}$ and $f_2 = 50\,\mathrm{mm}$ in a de-magnifying 1 : 4 telescope configuration. The thermal effects of the telescope were monitored by measuring the shift of the focus produced by a third lens f_3, positioned within the low power region behind the beam sampler, hence yielding a negligible contribution to thermal aberrations, see sketch in Fig. 2(a). Due to the 4-fold de-magnification of the beam, $w_2 = w_1/4 \simeq 550\,\mu\mathrm{m}$, the second lens experienced a 16-fold increased intensity, relative to the one impinging on f_1. The resulting trend of Δz_{th} is shown in Fig. 2(b), for a second lens f_2 made of fused silica [4] (red diamonds) or *Suprasil*®3001 [5] (black triangles), respectively. In spite of the sizable increase of the intensity on the second lens of the telescope, in both cases thermal lensing causes only negligible shifts of the f_3 focus location, $\Delta z_{th} \lesssim 100\,\mu\mathrm{m}$. Given that the atom clouds initially loaded within the ODT feature sizes easily exceeding a few millimeters, all these variations are irrelevant for our purpose, and a quantitative analysis of these three data sets goes beyond the scope of the present work. Nonetheless, in relation with the $f_1 - f_2$ data, we remark how our simple method indeed enables to distinguish among the (weak) thermal lenses of the two different substrates, the *Suprasil*®lens clearly outperforming the fused silica one. Further, we stress that the single lens data set cannot be directly compared with the one taken with the telescope owing to the different setup. In particular, as it will be discussed in the following, the former characterization was affected by stronger spurious effects associated with thermal lensing due to the filtering stage.

As a next step, we characterized the thermal lens associated with the acousto-optic modulator which enables to control the beam power on the atomic sample. In particular, we considered a standard AOM [6] made by an AR-coated TeO_2 crystal that enables maximum diffraction

[4] LA4148-YAG-ML by *Thorlabs*
[5] AR/AR1070 PLCX-25.4/25.8 S3001 by *LaserComponents*
[6] 3110 – 191 by *Gooch&Housego*

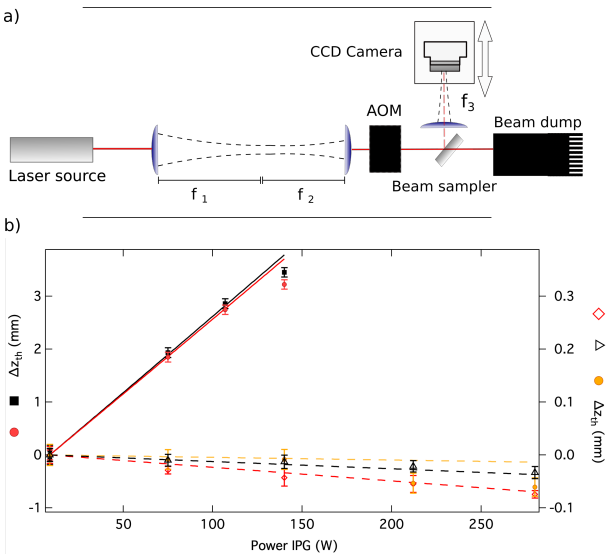

Fig. 2. Characterizing thermal lensing of different optical elements. **a)** Setup for thermal lensing measurements. Along the full path, the high power beam passes through two lenses and one AOM. A $BSF10-C$ coated beam sampler enables to create a low-power ($P < 10$ W) copy of the beam, which is further attenuated by transmission trough a high-reflection mirror (not shown). The resulting beam of a few mW is then focused by a third lens f_3 and sent to a CCD camera mounted on a translation stage (double arrow). The focus position is measured by recording the peak intensity of the Gaussian spot versus the camera position. **b)** Thermal shifts Δz_{th} as a function of the laser power recorded for different combinations of optical elements. Right axis: Δz_{th} due to the $f_1 - f_2$ telescope with $f_2 = 50$ mm in $Suprasil^{®}3001$ (black triangles) or in UV fused silica (red diamonds). The shift of the $f_1 = 200$ mm fused silica lens alone (yellow circles) has been tested directly by measuring its focus shift versus the beam power. For each data set, the dashed line is the corresponding shift calculated by Gaussian beam propagation analysis, assuming each element to represent an additional lens with f_{th} given by Eq. (1) and characterized by the corresponding m_0 value listed in Table 1. Left axis: Thermal shift of the optical setup with inclusion of the AOM crystal, with (black squares) or without (red circles) quartz window in the beam path. The AOM was placed at $d_{AOM,2} = 3(1)$ cm behind the second lens f_2, the last lens f_3 at $d_{3,AOM} = 58(2)$ cm, whereas the window (if present) was at $d_{win,3} = 12(1)$ cm after f_3. Solid lines (same color code) show the focus shift calculated by Gaussian beam propagation analysis, assuming the AOM thermal lens to be described by Eq. (1) with the m_0 value given in Table 1.

efficiencies around 85% for an input beam waist of 550 μm. To this end, we positioned the AOM a few cm after the $f_1 - f_2$ telescope, see sketch in Fig. 2(a), and applied the same protocol discussed above for the telescope characterization. The outcome of this study is presented in Fig. 2(b) as black squares. Despite our working conditions were far from the AOM damage threshold of 10 MW/cm^2 at 1070 nm, the TeO_2 crystal resulted to provide a shift of the focus location about two orders of magnitude larger than the ones observed with the lenses alone. Given that the observed focal shift appear to be only weakly modified by the presence of an additional quartz window behind the AOM, see red circles in Fig. 2(b), we conclude that the only sizable source of thermal lensing in such a model setup is represented by the TeO_2 crystal. Additionally, it is interesting to notice how the shift caused by the AOM is opposite to the one observed with the other elements, signaling a negative dn/dT of the TeO_2 substrate.

Our findings, despite not enabling an accurate, independent measure of the m_0 parameters

characterizing all elements of the setup, appear compatible with the values that can be found in literature [8, 27, 29, 30] for the different substrates. This was verified by comparing the experimental data with the outcome of simulations of Gaussian beam propagation, shown as dashed and solid lines in Fig. 2(b). Our analysis assumed each thermal lens to be describable as a thin lens positioned in correspondence of the associated physical substrate, and characterized by the m_0 values retrieved from previous studies, summarized in Table 1. In particular, the simulated Δz_{th} quantitatively match all experimental data sets, except for the case of one single fused silica lens, for which the measured shift (yellow circles) significantly exceeds the simulated one (yellow dashed line). We ascribe such a sizable mismatch, absent when considering two fused silica lenses in a telescope configuration (red diamonds), to the spurious contribution of the thermal lens associated with the filtering stage that, for the single lens measure, was illuminated by a tightly focused beam.

Optical element/substrate	$m_0(\mathrm{mW}^{-1})$	Reference
AOM/ TeO_2 crystal	$-1.13(7)\times10^{-10}$	[8]
Window/ Quartz	$-4.9(5)\times10^{-13}$ (o-axis) $-10.1(11)\times10^{-13}$ (e-axis)	[27]
Lenses/ UV fused silica	$4.1(8)\times10^{-12}$	[29]
Lenses/ *Suprasil*®	$10(1)\times10^{-14}$	[30]

Table 1. List of m_0 values characterizing the different sources of thermal lensing in our setup. The specified uncertainties combine the ones given in the corresponding references with the uncertainty in the determination of the specific substrate thicknesses.

Consistently with the trends presented in Fig. 2(b), one can notice from Table 1 how the focal length f_{th} associated with the TeO_2 substrate is negative and about 25 (200) times shorter than the one of fused silica (quartz) elements under the same intensity conditions. This confirms that the AOM crystal represents the major and only relevant source of thermal lensing within our ODT setup. Based on the results of [8] and on our measurements, the AOM is expected to feature $|f_{th}| \leq 10\,\mathrm{m}$ for the maximum power delivered by our source and with a 550 μm beam waist, whereas all other elements exhibit ten or hundred times longer thermal focal lengths. From a simple Gaussian beam propagation analysis, it is easy to verify that the f_{th} of a TeO_2 crystal, when placed behind a de-magnifying telescope as in typical optical trapping setups, may cause a few millimeters thermal shift of the focus of the last lens f_3. On the other hand, we remark that the contribution of other elements, irrelevant within the setup under consideration in the present study, could become important when illuminated with much higher intensities. We finally emphasize that special care must be taken in the alignment of the beam at the center of the AOM crystal and the other optical elements. This is essential to guarantee paraxial working conditions and to avoid, besides thermal shifts of the waist position, subject of the present study, thermal induced aberrations that easily lead to strong astigmatism, especially when few micron beam waists are considered.

4. Compensation of thermal lensing effects

As anticipated when discussing Eq. (2) and the special case described in Eq. (3), the impact of one thermal lens on a propagating beam can be minimized by positioning the thermal element within a focus along the optical path [6, 19]. In particular, this is possible whenever the thermal focal length greatly exceeds the Rayleigh length of the incoming beam, $|f_{th}| \gg z_R$, which is actually fulfilled by the typical trapping setups in cold atom experiments. Indeed, the f_{th}

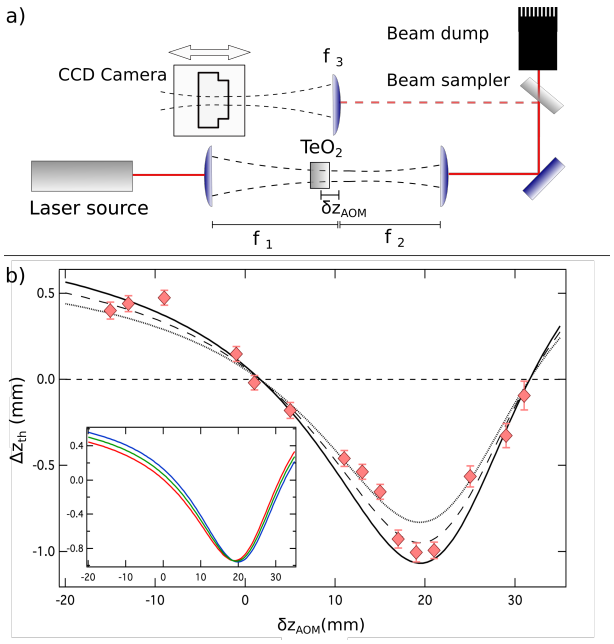

Fig. 3. Model setup to control thermal lensing effects. **a)** Schematic view of the optical scheme employed for the characterization of the AOM thermal lens, as a function of the crystal position. A TeO_2 crystal is placed at a variable distance δz_{AOM} from the focus within the $f_1 - f_2$ telescope as shown in the picture. For this measure, $f_1 = 300$ mm and $f_2 = 75$ mm. The f_3 lens is placed at $d_{3,2} = 47(2)$ cm from the second lens f_2, and the focus location is monitored for different levels of incident laser power through a CCD camera. **b)** Thermal-induced shift Δz_{th} of the f_3 focus position experimentally determined (red diamonds), as a function of the AOM distance from the f_1 focus. Δz_{th} is obtained by comparing high and low power data acquired at $P = 50(1)$ W and $P = 9.0(5)$ W, respectively. The shift predicted by the Gaussian beam propagation analysis is shown as black lines for $P = 55$ W (solid), $P = 50$ W (dashed) and $P = 45$ W (dotted). Inset: expected behavior of Δz_{th} for an incident power of 55 W for three different distances between second and third lens: $d_{3,2} = 47$ cm (green), $d_{3,2} = 50$ cm (blue) and $d_{3,2} = 44$ cm (red).

connected with the TeO_2 crystal of the setup is such that $|f_{th}|/z_R > 10$ for the highest intensities explored in this study. As a first step in the direction of eliminating the effect of the AOM thermal lens on the trapping beam, we characterized how the focus produced by f_3 on a CCD camera, see sketch in Fig. 3(a), shifts as a function of the position δz_{AOM} of a TeO_2 crystal relative to the focus of the $f_1 - f_2$ telescope, for two different values of the incident power (see details in Fig. 3 caption). Given that f_1 focuses the incident beam down to waists of about 45 μm, the power level was in this case kept below 60 W. Nonetheless, this corresponds to an intensity on the AOM crystal about 40 times higher than the one reached within standard operating conditions, yielding $f_{th} \sim 30$ cm. The acquired data are shown as red diamonds in Fig. 3(b), together with the simulated curves obtained from the analysis of Gaussian beam propagation. The simulation accounted for the three lenses of the setup, placed at fixed positions, and it included a thin lens f_{th} at the center of the AOM crystal, characterized by the m_0 parameter reported in Table 1. From Fig. 3(b) one can notice how a small variation of the TeO_2 thermal lens position, by less than the crystal thickness, may strongly modify the beam propagation, leading to both positive and negative shifts of the f_3 focus with the incident power on the TeO_2 crystal. Notably, the

overall trend of Δz_{th} is reproduced by our simple theoretical analysis, implying that, for our typical working conditions, Eq. (1) provides an excellent approximation to describe the thermal lenses of our setup. As shown in the inset of Fig. 3(b), the overall trend of Δz_{th} exhibits a much weaker dependence upon the distance $d_{3,2}$ between the second and the third lens. This can be understood considering that the beam behind the telescope has a Rayleigh length of the order of one meter, much larger than the one featured by the beam within the focus of the telescope, on the order of 3 mm.

Based on the experimental data and the simulation results shown in Fig. 3(b), one can notice that thermal lensing can be zeroed for two, rather than one, distinct AOM positions. Indeed, besides the $\delta z_{AOM} = 0$ configuration, negligible thermal shifts were also observed for $\delta z_{AOM} \sim 30$ mm. By inspecting the simulated beam propagation through the whole setup sketched in Fig. 3(a), we found that this second $\Delta z_{th} = 0$ point occurs for a position of the AOM that yields, at the plane of the third lens, a radius of curvature that coincides with the one of the unperturbed beam, obtained for $|f_{th}| = \infty$. While also this second configuration enables to strongly suppress thermal lensing, it is however less robust than the $\delta z_{AOM} = 0$ one. Given that in this case the radii of curvature associated with different power levels coincide only at the f_3 plane, rather than throughout the whole optical path, the beam magnification due to f_{th} at the f_3 plane may significantly differ from unity. As a consequence, although the position of the focus produced by f_3 will only weakly depend upon the specific value of f_{th} (i.e. of incident power), the beam waist may sizable vary, relative to the $|f_{th}| = \infty$ case.

Aside for understanding the detailed behavior of Δz_{th}, this proof-of-principle experiment shows that it is indeed possible to cancel out the thermal lensing effect introduced by the AOM by properly adjusting its position to match a beam waist along the optical path. Importantly, this holds irrespective of the systematic uncertainty in the determination of δz_{AOM} within the optical setup and, possibly, of a small deviation from the perfect $f_1 - f_2$ telescope configuration. On the other hand, the present configuration cannot be employed in a realistic optical trapping setup. Indeed, the beam waist in the focus of the $f_1 - f_2$ telescope is about 45 μm, which drastically reduces the diffraction efficiency of the TeO_2 crystal, and that would yield at the highest power level of our laser source an intensity exceeding the AOM damage threshold.

In order to overcome this issue while keeping the TeO_2 crystal within a focus of the optical trapping beam, among different solutions, we opted for a scheme based on the same elements depicted in Fig. 3(a), with the first two lenses no longer in a telescope configuration but rather acting as an equivalent lens with effective focal length $f_{1,2}^{eq}$. The latter will generally depend upon the parameter δz, defined as:

$$\delta z = L_2 - L_1 - (f_1 + f_2) \tag{5}$$

Here L_i and f_i denote the position and the focal length of the $i - th$ lens, respectively. The first lens was mounted on a translation stage with a resolution of 10^{-2} mm, and the position of the focus produced by $f_{1,2}^{eq}$ was determined by Gaussian beam matrices as a function of the L_1 position, hence of δz.

From our theoretical analysis we found that there exist various L_1 configurations, all for small and positive δz values, yielding a focus at relatively short distances from the second lens f_2, with the beam waist ranging between 550 and 500 μm. Therefore, we proved the feasibility of such a scheme by fixing the AOM crystal at two different exemplifying distances $d_{AOM,2}$ from the second lens f_2: $d_{AOM,2} = 23(2)$ cm and $d_{AOM,2} = 3(1)$ cm, respectively. In particular, the latter one corresponds to the focus position of the equivalent lens with $\delta z \simeq 0$, i.e. with the two lenses $f_1 - f_2$ very close to the collimated condition. At this point, and for each of the two AOM configurations, we finely scanned δz upon varying the position L_1 of the first lens, hence modifying the resulting $f_{1,2}^{eq}$ and the associated focus location. This procedure is less intuitive than the one previously described when discussing Fig. 3(b) data, since the change in position of the first lens, rather than the AOM one, simultaneously modifies the focal length $f_{1,2}^{eq}$ and

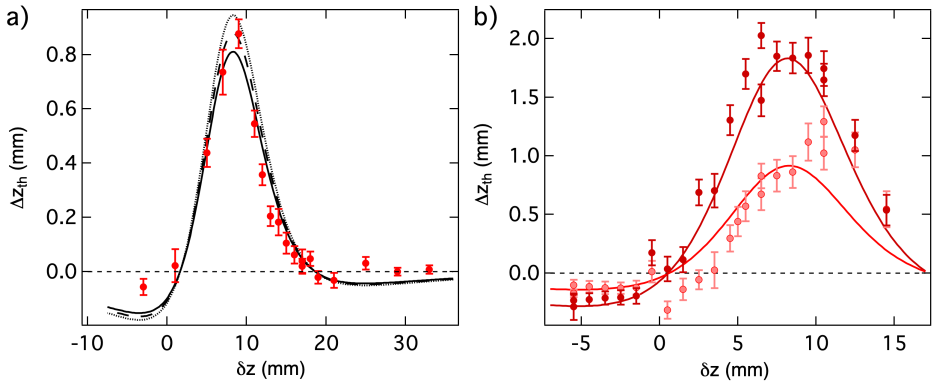

Fig. 4. Controlling the AOM thermal lensing through an equivalent lens. The two panels show the measured thermal shift Δz_{th} (red circles) of the focus created by the last lens f_3 as a function of the parameter δz given by Eq. (5), for the two different AOM locations discussed in the main text. **a)** The AOM was positioned at $d_{AOM,2} = 23(2)$ cm relative to the plane of the second lens. Δz_{th} was obtained by comparing the focus position measured at $P = 75(1)W$ and $P = 9.0(5)W$, respectively. Black lines show the simulated Δz_{th} for different high power levels: 80 W (dotted lines), 75 W (dashed lines) and 70 W (solid lines). **b)** Experimentally measured thermal shift as in panel a), but with the AOM positioned at $d_{AOM,2} = 3(1)$ cm. Two high power values have been checked, relative to the low power reference at $P = 9.0(5)$ W: 80(1) W (light red circles) and 150(2) W (dark red circles). Solid lines show the simulated trend expected for the two power levels. For both data sets, $f_1 = 300$ mm and $f_2 = 75$ mm, and the last lens f_3 was kept fixed at $d_{3,2} = 155(2)$ cm. In both panels, error bars combine the standard error of the axial intensity profile fitted to Eq. (4) for the high and low power data sets.

the position of the focal point relative to the TeO_2 crystal. On the other hand, this method has the advantage that it does not affect the alignment of the optical path behind the AOM once the diffracted first order beam is employed, as in standard working conditions of the trapping setup. Despite this slightly modified measuring protocol, thermal effects arising from the AOM crystal could be quantified by monitoring how the focus produced by the third lens f_3 varied with δz for two different levels of incident power, similarly to what discussed above the data shown in Fig. 3.

The results of this latter characterization are presented in Fig. 4 for the two $d_{AOM,2}$ values considered here. In particular, Fig. 4(a) shows the thermal shifts measured with the AOM positioned at $d_{AOM,2} = 23(2)$ cm from the second lens, whereas Fig. 4(b) presents the outcome of the analogous characterization for $d_{AOM,2} = 3(1)$ cm. For both AOM positions explored, the last f_3 lens was kept at a fixed distance $d_{3,2} = 155(2)$ cm from the second one. Aside for slight quantitative changes, the observed trends of Δz_{th} qualitatively agree with the one obtained when moving the TeO_2 crystal within the focus of the $f_1 - f_2$ telescope, see Fig. 3(b). Also in these cases, the measured thermal shifts appear to be reasonably reproduced by our theoretical analysis, featuring a sharp peak connected via two zero-crossing points to two outer regions characterized by a slowly-varying value of $\Delta z_{th} < 0$. In both cases the range of δz that can be investigated experimentally is limited on one side by the diffraction efficiency (too small beam waists on the AOM) and the finite TeO_2 crystal size on the other. These data demonstrate that even in this case it is possible to experimentally identify special configurations of the $f_1 - f_2$ setup for which the thermal lensing effect of the TeO_2 crystal can be zeroed, while guaranteeing an AOM diffraction efficiency exceeding 80%.

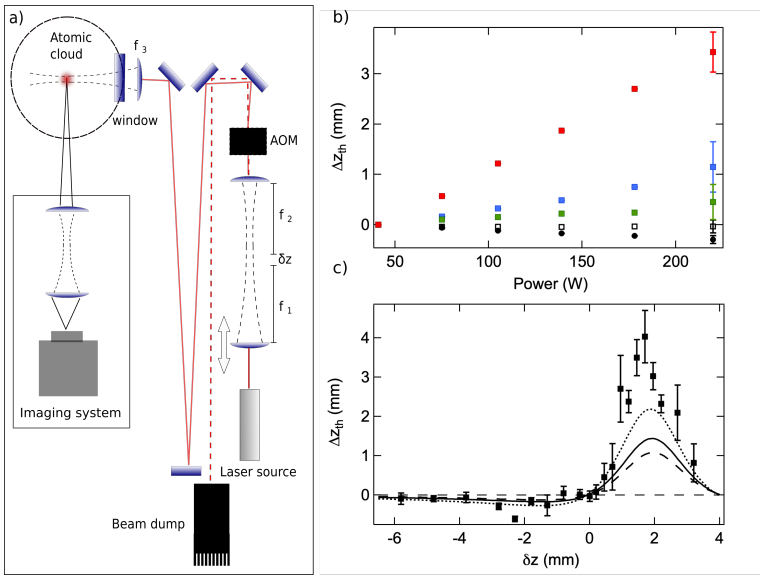

Fig. 5. Realizing an optical dipole trap without thermal lensing effects. **a)** Sketch of the setup employed to investigate thermal lensing by monitoring an atomic cloud trapped in the ODT. Typical atom number in the ODT after 400 ms illumination time ranges from 1×10^5 ($P = 40$ W) to 7×10^5 ($P = 220$ W). For this measurements, $f_1 = 200$ mm and $f_2 = 50$ mm while the last lens f_3 is placed at $d_{3,AOM} = 200(5)$ cm. **b)** Thermal shift Δz_{th} of the focus position as a function of the beam power P for different values of the parameter δz: $\delta z = 1.7(1)$ mm (red squares), $\delta z = 1.2(1)$ mm (blue squares), $\delta z = 0.45(1)$ mm (green squares), $\delta z = 0.0(1)$ mm (white squares) and $\delta z = -2.3(1)$ mm (black circles). **c)** Thermal shift Δz_{th} as a function of the parameter δz at a fixed power $P = 220(2)$ W. The solid line shows the thermal shift expected from the Gaussian beam matrices calculation considering the f_{th} of the AOM crystal given by Eq. (1) with the m_0 value shown in Table 1. The dashed (dotted) line shows the expected thermal shift for $f_{th} + \Delta f_{th}$ ($f_{th} - \Delta f_{th}$) where Δf_{th} is our estimate of f_{th}'s uncertainty of around 35%. Error bars combine the statistical uncertainties of the high and low power reference data sets on the atomic cloud barycenter, obtained for each point from an average of 4 independent measurements.

We finally tested the efficacy of our scheme by directly monitoring the axial position of a cold atomic cloud confined within the high power beam, employing a configuration of the optical setup analogous to the one considered in Fig. 4(b), with $d_{AOM,2} = 3(1)$ cm, see sketch in Fig. 5(a). By following procedures that will be described in a forthcoming publication, we produced cold clouds of about $2.0(2) \times 10^8$ ^6Li atoms at $T \simeq 80$ μK, which we subsequently illuminated with the ODT beam. After an illumination time of 400 ms, long enough to ensure that stationary conditions were attained, the position of the trapped sample along the ODT axis was obtained by Gaussian fits to the atomic density profiles, obtained through *in situ* absorption imaging performed along one direction perpendicular to the trapping beam, see Fig. 5(a). In turn, for any value of incident power and of δz, the axial barycenter of the atom cloud reflects the waist position of the ODT beam, corresponding to the energy minimum of the optical potential. Fig. 5(b) shows examples of the experimentally determined shifts of the cloud position along the beam axis, relative to the one obtained at the lowest possible power enabling to capture a detectable atomic fraction ($P = 40(1)$ W), as a function of the power level for different δz values. Also, these data show that one can adjust the δz parameter to induce either positive or negative thermal

shifts of variable magnitude and, most importantly, to cancel them out.

Finally, Fig. 5(c) shows, as a function of δz, the thermal shift obtained by comparing the atomic cloud positions recorded under high ($P = 220(2)$ W) and low ($P = 40(1)$ W) power conditions. The resulting trend qualitatively matches the one presented in Fig. 4, albeit featuring a poorer agreement with the simulation (solid line). In particular, our theoretical model systematically underestimates the measured shifts (black squares) around the region of maximum Δz_{th}, even when allowing for a ±35% uncertainty in the determination of the AOM thermal lens (dashed and dotted curves). We ascribe this mismatch to some degree of astigmatism that affected the trapping beam for this specific δz range, likely caused by a non-perfect centering of the beam on the AOM crystal. These non-ideal conditions enhance the thermal lensing effect since astigmatism significantly modifies the potential landscape experienced by the cold atomic cloud, yielding weaker effective confinement along the axial direction and amplifying the thermal shift of the trap minimum. On the other hand, we find quantitative agreement between the experimental data and the simulated curve around the Δz_{th} zero crossing points, whose identification represents the main focus of our study. Most importantly, Fig. 5(c) data confirm again the possibility to cancel out thermal lensing effects from a high power optical trapping setup by properly adjusting the AOM position with respect to the beam waist.

5. Conclusions

In conclusion, we have characterized the sources of thermal lensing associated with the various elements composing a typical high power setup for optical trapping of cold atomic clouds. From this survey, we identified the TeO_2 crystal of the AOM as the sole relevant thermal lens affecting the optical system, whereas we found that inexpensive fused silica lenses and quartz windows provide a negligible contribution. We then devised a simple, totally passive scheme that enables to cancel thermal lensing effects on the trapping beam up to very high intensities. Our strategy relies on placing the thermal lens within one focus of the laser beam. This allowed to stabilize the waist position of the high power beam used as optical dipole trap, with thermal shifts below our experimental resolution, as low as a few tens of microns. Our data are reasonably reproduced by a simple Gaussian beam matrices calculation, by treating the AOM crystal as a thin thermal lens f_{th}, employing the power dependence previously reported in literature for TeO_2 substrates [8]. Although this study was specifically oriented to the implementation of a high power optical dipole trap for cold atom experiments, our strategy may find applications within any generic optical setup featuring one or few thermal lensing sources. Furthermore, this configuration could be also integrated into more complex setups, aiming to cure, besides thermal shifts of the focus position, thermal induced phase aberrations which can significantly distort the beam waist when this approaches the diffraction limit.

Funding

This work was supported under European Research Council grant No. 637738 PoLiChroM, and under Italian MIUR FARE grant No. R168HMHFYM P-HeLiCS.

Acknowledgments

We acknowledge insightful discussions with the members of the LENS Quantum Gases group, and in particular with Giacomo Roati and Francesco Scazza.

References

1. K. C. Neuman and S. M. Block, "Optical trapping," Rev. Sci. Instrum. **75**, 2787–2809 (2004).
2. R. Grimm, M. Weidemüller, and Y. B. Ovchinnikov, "Optical dipole traps for neutral atoms," (Academic, 2000), pp. 95–170.

3. J. P. Gordon, R. C. C. Leite, R. S. Moore, S. P. S. Porto, and J. R. Whinnery, "Long-transient effects in lasers with inserted liquid samples," J. Appl. Phys. **36**, 3–8 (1965).
4. M. Sparks, "Optical distortion by heated windows in high-power laser systems," J. Appl. Phys. **42**, 5029–5046 (1971).
5. B. Bendow and P. D. Gianino, "Optics of thermal lensing in solids," Appl. Opt. **12**, 710–718 (1973).
6. S. J. Sheldon, L. V. Knight, and J. M. Thorne, "Laser-induced thermal lens effect: a new theoretical model," Appl. Opt. **21**, 1663 (1982).
7. R. G. Beausoleil, E. K. Gustafson, M. M. Fejer, E. D'Ambrosio, W. Kells, and J. Camp, "Model of thermal wave-front distortion in interferometric gravitational-wave detectors I: Thermal focusing," J. Opt. Soc. Am. B **20**, 1247 (2003).
8. C. Bogan, P. Kwee, S. Hild, S. H. Huttner, and B. Willke, "Novel technique for thermal lens measurement in commonly used optical components," Opt. Express **23**, 15380 (2015).
9. K. M. O'Hara, S. L. Hemmer, M. E. Gehm, S. R. Granade, and J. E. Thomas, "Observation of a strongly interacting degenerate Fermi gas of atoms," Science **298**, 2179–2182 (2002).
10. S. Jochim, M. Bartenstein, A. Altmeyer, G. Hendl, S. Riedl, C. Chin, J. Hecker Denschlag, and R. Grimm, "Bose-Einstein condensation of molecules," Science **302**, 2101–2103 (2003).
11. A. Burchianti, G. Valtolina, J. A. Seman, E. Pace, M. De Pas, M. Inguscio, M. Zaccanti, and G. Roati, "Efficient all-optical production of large ^{6}Li quantum gases using D_1 gray-molasses cooling," Phys. Rev. A **90**, 043408 (2014).
12. E. Wille, F. M. Spiegelhalder, G. Kerner, D. Naik, A. Trenkwalder, G. Hendl, F. Schreck, R. Grimm, T. G. Tiecke, J. T. M. Walraven, S. J. J. M. F. Kokkelmans, E. Tiesinga, and P. S. Julienne, "Exploring an ultracold Fermi-Fermi mixture: Interspecies Feshbach resonances and scattering properties of ^{6}Li and ^{40}K," Phys. Rev. Lett. **100**, 053201 (2008).
13. F. M. Spiegelhalder, A. Trenkwalder, D. Naik, G. Kerner, E. Wille, G. Hendl, F. Schreck, and R. Grimm, "All-optical production of a degenerate mixture of ^{6}Li and ^{40}K and creation of heteronuclear molecules," Phys. Rev. A **81**, 043637 (2010).
14. C. Chin, R. Grimm, P. Julienne, and E. Tiesinga, "Feshbach resonances in ultracold gases," Rev. Mod. Phys. **82**, 1225–1286 (2010).
15. R. Onofrio and C. Presilla, "Reaching Fermi degeneracy in two-species optical dipole traps," Phys. Rev. Lett. **89**, 100401 (2002).
16. S. Tassy, N. Nemitz, F. Baumer, C. Höhl, A. Batär, and A. Görlitz, "Sympathetic cooling in a mixture of diamagnetic and paramagnetic atoms," J. Phys. B: At. Mol. Opt. Phys. **43**, 205309 (2010).
17. A. H. Hansen, A. Y. Khramov, W. H. Dowd, A. O. Jamison, B. Plotkin-Swing, R. J. Roy, and S. Gupta, "Production of quantum-degenerate mixtures of ytterbium and lithium with controllable interspecies overlap," Phys. Rev. A **87**, 013615 (2013).
18. V. D. Vaidya, J. Tiamsuphat, S. L. Rolston, and J. V. Porto, "Degenerate Bose-Fermi mixtures of rubidium and ytterbium," Phys. Rev. A **92**, 043604 (2015).
19. K. Uchiyama, A. Hibara, H. Kimura, T. Sawada, and T. Kitamori, "Thermal lens microscope," Jpn. J. Appl. Phys. **39**, 5316–5322 (2000).
20. M. Tokeshi, J. Yamaguchi, A. Hattori, and T. Kitamori, "Thermal lens micro optical systems," Anal. Chem. **77**, 626–630 (2005).
21. C. A. Klein, "Thermally induced optical distortion in high-energy laser systems," Opt. Eng. **18**, 591 – 601 (1979).
22. C. A. Klein, "Materials for high-power laser optics: the thermal lensing issue," Proc. SPIE 10286 (1996).
23. R. M. Waxler and G. Cleek, "The effect of temperature and pressure on the refractive index of some oxide glasses," J. Res. Natl. Bureau Standards Sect. A: Phys. Chem. **77A**, 755 (1973).
24. P. Hello and J.-Y. Vinet, "Analytical models of thermal aberrations in massive mirrors heated by high power laser beams," J. Phys. **51**, 1267–1282 (1990).
25. S. A. Self, "Focusing of spherical Gaussian beams," Appl. Opt. **22**, 658–661 (1983).
26. R. Silva, M. A. C. de Araújo, P. Jali, S. G. C. Moreira, P. Alcantara, and P. C. de Oliveira, "Thermal lens spectrometry: Optimizing amplitude and shortening the transient time," AIP Adv. **1**, 022154 (2011).
27. T. Toyoda and M. Yabe, "The temperature dependence of the refractive indices of fused silica and crystal quartz," J. Phys. D: Appl. Phys. **16**, L97–L100 (1983).
28. T. A. Hahn and R. K. Kirby, "Thermal expansion of fused silica from 80 to 1000 K-standard reference material 739," AIP Conf. Proc. **3**, 13–24 (1972).
29. M. Khashan and A. Nassif, "Dispersion of the optical constants of quartz and polymethyl methacrylate glasses in a wide spectral range: 0.2– 3 μm," Opt. Commun. **188**, 129 – 139 (2001).
30. B. D. Leviton, H. K. Miller, M. A. Quijada, and U. F. Grupp, "Temperature-dependent refractive index measurements of CaF_2, $Suprasil3001$, and $S-FTM16$ for the euclid near-infrared spectrometer and photometer," Proc. SPIE 9578 (2015).

Ringraziamenti

Scusandomi con il lettore per il repentino cambiamento, dedico questa ultima pagina nella mia lingua madre a coloro senza i quali il raggiungimento di questo traguardo non mi sarebbe mai stato possibile.
Innanzitutto, ringrazio il mio supervisore, il Prof. Massimo Inguscio, ed il mio tutore, Matteo Zaccanti, non solo per avermi dato la possibilità di lavorare a questo progetto, ma anche e specialmente per aver fatto sì che esso abbia preso le sue prime mosse. In particolare ringrazio Matteo, per aver impiegato la sua audacia, le sue capacità immaginifiche e la sua dedizine alla nascita di questo nuovo esperimento, e per aver tentato di trasmettermele. Lo ringrazio anche per essere stato un amico, e per il tempo perso insieme a discutere su come fare a perdere meno tempo.
In secundis, ringrazio Andreas. Lo ringrazio per la facilità con cui sa essere un infinito pozzo di conoscenza del mestiere, ma soprattutto per aver capito la mia persona con la discrezione e gentilezza d'animo che gli sono proprie.
Ringrazio poi Michael, Cristiano e Alessio, con cui ho condiviso relativamente poco tempo nel laboratorio 9, ma con cui ho saputo imparare, e soprattutto ridere. Poiché poter ridere laddove si lavora è un grande privilegio, sono loro profondamente riconoscente.
Ringrazio anche gli studenti che hanno lavorato presso il nostro laboratorio, per avermi insegnato a condividere e dove possibile a insegnare. Tra loro ringrazio soprattutto Marco e Irene, per essere rimasti genuini amici, oltre che colleghi.
Ringrazio poi i miei amici. Essi sono così preziosi che senza di loro non avrei concluso molto in questi anni. Tra tutti loro non posso non nominare Chiara, Barbara, Lorenza e Francesco, per l'infinita pazienza con cui hanno saputo sostenermi. Con loro, e per gli stessi motivi, nonché per aver condiviso con me tanto della sua vita in questi anni, ringrazio Jacopo. Grazie per le sere, per le gite e per la condivisione ai miei compagni del Mercoledì sera.

Infine, ringrazio la mia famiglia tutta, mia mamma e mio babbo in primis per non aver smesso mai di insegnarmi a farmi domande su di me e sul Mondo.

Bibliography

[1] O. I. Kartavstev and A. V. Malyhk *J. Phys. B*, vol. **40**, p. 1429, 2007.

[2] D. S. Petrov *hys. Rev. A*, vol. **67**, p. 010703(R), 2003.

[3] B. Naylor *et al. Phys. Rev. A*, vol. **91**, p. 011603(R), 2015.

[4] R. Chicireanu. Phd thesis, Université Paris-Nord - Paris XIII, 2007.

[5] C. Simonelli *et al. arXiv:1904.01965*, 2019. Accepted by *Optics Express*.

[6] K. Xhani *et al. arXiv:1905.08893*, 2019. Submitted to *Phys. Rev. Lett.*

[7] L. D. Landau and E. M. Lifshitz, *-Quantum Mechanics - Non relativistic theory-*. Pergamon Press, 1965.

[8] C. Chin *et al. Rev. Mod. Phys.*, vol. **82**, p. 1225, 2010.

[9] D. S. Petrov *arXiv:1206.5752v2*, 2012.

[10] P. Massignan, M. Zaccanti, and G. M. Bruun *Rep. Prog. Phys.*, vol. **77**, p. 034401, 2014.

[11] Y. Castin, "*-Basic theory tools for degenerate Fermi gases-*," in *Proceedings of the International School of Physics "Enrico Fermi"*, pp. 289–349, 2007.

[12] L. Pricoupenko and Y. Castin *Phys. Rev. A*, vol. **69**, p. 051601(R), 2004.

[13] Y. Zhenhua *et al. J. Phys. B*, vol. **44**, p. 195207, 2011.

[14] F. Dalfovo *et al. Rev. Mod. Phys.*, vol. **71**, p. 463, 1999.

[15] W. Zwerger, -*The BCS-BEC crossover and the unitary Fermi gas*-, vol. **836**. Springer Science & Business Media, 2011.

[16] A. J. Leggett, -*Quantum liquids: Bose condensation and Cooper pairing in condensed-matter systems*-. Oxford University Press, 2006.

[17] G. Bertsch *Int. J. Mod. Phys. B*, vol. **15**, 2001.

[18] D. S. Petrov *Phys. Rev. Lett.*, vol. **94**, p. 143201, 2004.

[19] P. Zou and F. Dalfovo *Journal of Low Temperature Physics*, vol. **177**, p. 240, 2014.

[20] A. Bulgac *et al. Phys. Rev. Lett.*, vol. **112**, p. 025301, 2014.

[21] J. Bardeen, L. N. Cooper, and J. R. Schrieffer *Phys. Rev.*, vol. **108**, no. 5, p. 1175, 1957.

[22] W. Meissner and R. Ochsenfeld *Naturwissenschaften*, vol. **21**, no. 44, pp. 787–788, 1933.

[23] H. Fröhlich *Phys. Rev.*, vol. **79**, no. 5, p. 854, 1950.

[24] H. Fröhlich, "-*Interaction of electrons with lattice vibrations*-," *Proceedings of the Royal Society of London. Series A. Mathematical and Physical Sciences*, vol. 215, no. 1122, pp. 291–298, 1952.

[25] J. F. Annett, -*Superconductivity, Superfluids and Condensates*-. Oxford University Press, 2004.

[26] R. Casalbuoni and G. Nardulli *Rev. Mod. Phys.*, vol. **76**, p. 263, 2004.

[27] A. Adams *et al. New Jour. Phys.*, vol. **15**, p. 045022, 2013.

[28] A. M. Clonston *Phys. Rev. Lett.*, vol. **9**, no. 6, p. 266, 1962.

[29] S. Pilati and S. Giorgini *Phys. Rev. Lett.*, vol. **100**, p. 030401, 2008.

[30] G. V. Skorniakov and K. A. Ter-Martirosian *Sov. Phys. JEPT*, vol. **4**, no. 5, p. 648, 1957.

[31] E. Fulde and R. A. Ferrel *Phys. Rev. A*, vol. **135**, p. A550, 1964.

[32] A. I. Larkin and Y. N. Ovchinnikov *Zh. Eksp. Teor. Fiz.*, vol. **47**, p. 1136, 1964.

[33] E. Gubankova, W. V. Liu, and F. Wilczek *Phys. Rev. Lett.*, vol. **91**, p. 032001, 2003.

[34] G. Sarma *J. Phys. Chem. Solids*, vol. **24**, p. 1029, 1963.

[35] W. V. Liu and F. Wilczek *Phys. Rev. Lett.*, vol. **90**, p. 047002, 2003.

[36] G. B. Partridge *et al.*

[37] M. Zwierlein *et al. Science*, vol. **311**, p. 492, 2006.

[38] Y. Shin *et al. Phys. Rev. Lett.*, vol. **101**, p. 070404, 2008.

[39] Y. Shin *et al. Nature*, vol. **451**, p. 689, 2008.

[40] Y. Liao *et al. Nature*, vol. **467**, pp. 567–569, 2010.

[41] Y. Matsuda and H. Shimahara *J. Phys. Soc. Jpn.*, vol. **76**, p. 051005, 2007.

[42] J. Singleton *et al. Journal of Physics: Condensed Matter*, vol. **12**, no. 40, p. L641, 2000.

[43] R. Lortz *et al. Phys. Rev. Lett.*, vol. **99**, p. 187002, 2007.

[44] R. Beyer and J. Wosnitza *Low Tem. Phys.*, vol. **39**, p. 225, 2013.

[45] H. Guo *et al. Phys. Rev. Lett.*, vol. **80**, p. 011601(R), 2009.

[46] J. E. Baarsma *et al. Physical Review A*, vol. **82**, p. 013624, 2010.

[47] J. Wang *et al. Scientific Reports*, vol. **7**, p. 39783, 2017.

[48] T. A. Corcovilos *et al. Phys. Rev. A*, vol. **81**, p. 013415, 2010.

[49] R. A. Hart *et al. Nature*, vol. **519**, pp. 211–214, 2015.

[50] L. W. Cheuk *et al. Phys. Rev. Lett.*, vol. **116**, p. 235301, 2016.

[51] M. Boll *et al. Science*, vol. **353**, pp. 1257–1260, 2016.

[52] T. A. Hilker *et al. Science*, vol. **3557**, pp. 484–487, 2017.

[53] C. Gross and I. Bloch *Science*, vol. **357**, pp. 995–1001, 2017.

[54] A. Mazurenko *et al. Nature*, vol. **545**, pp. 462–466, 2017.

[55] C. S. Chiu *et al. Phys. Rev. Lett.*, vol. **120**, p. 243201, 2018.

[56] G. B. Jo *et al. Science*, vol. **325**, p. 1521, 2009.

[57] C. Sanner *et al. Phys. Rev. Lett.*, vol. **108**, p. 240404, 2012.

[58] G. Valtolina *et al. Nature Physics*, vol. **13**, no. 7, p. 704, 2017.

[59] A. Amico *et al. Phys. Rev. Lett.*, vol. **121**, p. 253602, 2018.

[60] E. Stoner *Philos. Mag.*, vol. **15**, p. 1018, 1933.

[61] R. A. Duine and A. H. MacDonald *Phys. Rev. Lett.*, vol. **95**, p. 230403, 2005.

[62] D. Belitz, T. R. Kirkpatrick, and T. Vojta *Phys. Rev. Lett.*, vol. **82**, p. 4707, 1999.

[63] S. Pilati *et al. Phys. Rev. Lett.*, vol. **105**, p. 030405, 2010.

[64] G. J. Conduit, A. G. Green, and B. D. Simond *Phys. Rev. Lett.*, vol. **103**, p. 207201, 2009.

[65] X. Cui and T. L. Ho *Phys. Rev. Lett.*, vol. **110**, p. 165302, 2013.

[66] A. C. Fonseca *et al. Nucl. Phys. A*, vol. **320**, p. 273, 1979.

[67] J. Levinsen and D. S. Petrov *Eur. Phys. J. D*, vol. **65**, p. 67, 2011.

[68] V. N. Efimov *Sov. J. Nucl. Phys*, vol. **12**, p. 101, 1971.

[69] V. N. Efimov *Nucl. Phys. A*, vol. **210**, p. 157, 1973.

[70] E. Braaten and H.-W. Hammer *Annals of Physics*, vol. **1**, pp. 10–163, 2007.

[71] M. Jag *et al. Phys. Rev. Lett.*, vol. **112**, p. 075302, 2014.

[72] P. F. Bedaque, H.-W. Hammer, and U. van Kolck *Phys. Rev. Lett.*, vol. **82**, p. 463, 1999.

[73] B. D. Esry, C. H. Greene, and J. P. Burke Jr *Phys. Rev. Lett.*, vol. **83**, p. 1751, 1999.

[74] E. Nielsen and J. H. Macek *Phys. Rev. Lett.*, vol. **83**, p. 1566, 1999.

[75] P. F. Bedaque, E. Braaten, and H.-W. Hammer *Phys. Rev. Lett.*, vol. **85**, p. 908, 2000.

[76] M. Zaccanti *et al. Nature Physics*, vol. 5, p. 586, 2009.

[77] M. Mcneil *et al. hys. Rev. Lett.*, vol. **94**, p. 017001, 2005.

[78] B. Bazak and D. S. Petrov *Phys. Rev. Lett.*, vol. **118**, p. 083002, 2017.

[79] M. Wutz, H. Adam, and W. Walcher, *-Theorie und Praxis der Vakuumtechnik-*. Brauschewig, De: Friedr. Vieweg and Sohn, 1988.

[80] P. V. webpage, "*-Know How-*."

[81] S. T. Barashkin *et al. J. Appl. Mech. Tech. Phys.*, vol. **20**, p. 547, 1979.

[82] G. Valtolina. Master thesis, Università degli Studi di Milano - Bicocca, 2012.

[83] M. E. Ghem. Phd thesis, Duke University, 2003.

[84] C. A. Stan. PhD thesis, Massachusetts Intitute of Technology, 2005.

[85] E. Lucioni *et al. Eur. Phys. J. Spec. Top.*, vol. **226**, p. 2775, 2017.

[86] C. J. Foot, *-Atomic Physics-*. New York, US: Oxford University Press, 2005.

[87] M. Bernardini *et al. J. Vac. Sci. Technol. A*, vol. **16**, p. 188, 1998.

[88] P. Chiggiato, "*-Thermal outgassing of hydrogen: models and methods for reduction-*," in *conference Vacuum in Accelerators*, 16-24 May 2006.

[89] P. Marin *et al. Vacuum*, vol. **49**, p. 309, 1998.

[90] D. L. Ride, *-CRC Handbook of Chemistry and Physics, Internet Version 2005-*. CRC Press, 2005.

[91] C. C. Bradley *et al. Phys. Rev. A*, vol. **61**, p. 053407, 2000.

[92] R. Chicireanu *et al. Phys. Rev. A*, vol. **76**, p. 023406, 2007.

[93] A. Burchianti *et al. Phys. Rev. A*, vol. **90**, p. 043408, 2014.

[94] C. W. Thie, *-Four-wave mixing and its applications-*. Faculty of Washington, Washington DC, 2008.

[95] F. S. Di Noia. master thesis, Università degli Studi diFirenze, 2015.

[96] A. Cosco. bachelor thesis, Università degli Studi diFirenze, 2016.

[97] K. M. O'Hara *et al. Science*, vol. **298**, pp. 2179–2182, 2002.

[98] S. Jochim *et al. Science*, vol. **302**, pp. 2101–2103, 2003.

[99] E. Wille *et al. Phys. Rev. Lett.*, vol. **100**, p. 053201, 2008.

[100] F. M. Spiegelhalde *et al. Phys. Rev. A*, vol. **81**, p. 043637, 2010.

[101] R. Grimm, M. Weidemüller, and Y. B. Ovchinnikov, "*-Optical Dipole Traps for Neutral Atoms-*," vol. **42** of *Advances In Atomic, Molecular, and Optical Physics*, pp. 95–170, Academic, 2000.

[102] G. Valtolina. Phd thesis, Scuola Normale Superiore di Pisa, 2016.

[103] J. P. Gordon *et al. Journal of Applied Physics*, vol. **36**, pp. 3–8, 1965.

[104] R. G. Beausoleil *et al. Journal of the Optical Society of America B*, vol. **20**, p. 1247, 2003.

[105] T. Toyoda and M. Yabe *Journal of Physics D: Applied Physics*, vol. **16**, pp. L97–L100, 1983.

[106] T. A. Hahn and R. K. Kirby *AIP Conference Proceedings*, vol. **3**, pp. 13–24, 1972.

[107] W. Ketterle and M. Zwierlein, "*-Making, probing and understanding ultracold Fermi gases-*," in *Proceedings-International School of Physics Enrico Fermi*, vol. **164**, p. 95, 2007.

[108] A. T. Grier *et al. Phys. Rev. A*, vol. **87**, p. 063411, 2013.

[109] F. Sievers *et al. Phys. Rev. A*, vol. **91**, p. 023426, 2015.

[110] E. Arimondo and G. Orriols *Lettere Al Nuovo Cimento*, vol. 17, pp. 333–338, 1976.

[111] I. Fritsche. Master thesis, University of Innsbruck, 2013.

[112] B. D. Josephson *Phys. Lett.*, vol. **1**, p. 251, 1962.

[113] P. W. Anderson *Rev. Mod. Phys.*, vol. **38**, p. 298, 1966.

[114] G. Valtolina *et al. Science*, vol. **350**, pp. 1505–1508, 2015.

[115] M. Zaccanti and W. Zwerger *arXiv preprint arXiv:1907.08052*, 2019.

[116] P. W. Anderson and J. M. Rowell *Phys. Rev. Lett.*, vol. **10**, p. 230, 1963.

[117] O. Avenel and E. Varoquaux *Phys. Rev. Lett.*, vol. **55**, p. 2704, 1985.

[118] R. Feynman, "*-Chapter II Application of Quantum Mechanics to Liquid Helium-*," vol. 1 of *Progress in Low Temperature Physics*, pp. 17 – 53, Elsevier, 1955.

[119] R. E. Packard *Rev. Mod. Phys*, vol. **70**, p. 641, 1998.

[120] Y. Sato and R. E. Packard *Rep. Prog. Phys*, vol. **75**, p. 616401, 2014.

[121] K. Sukhatme *et al. Nature*, vol. **411**, p. 280, 2001.

[122] D. S. Hall *et al. Phys. Rev. Lett.*, vol. 81, pp. 1539–1542, 1998.

[123] B. P. Anderson and M. A. Kasevich *Science*, vol. 282, pp. 1686–1689, 1998.

[124] F. Cataliotti *et al. Science*, vol. **293**, pp. 843–846, 2001.

[125] T. Schumm *et al. Nat. Phys.*, vol. **1**, pp. 57–62, 2005.

[126] L. J. LeBlanc *et al. Phys. Rev. Lett.*, vol. **106**, p. 025302, 2011.

[127] A. Ramanathan *et al. Phys. Rev. Lett.*, vol. **106**, p. 130401, 2011.

[128] M. Abad *et al. EPL*, vol. **109**, p. 4005, 2015.

[129] G. Spagnolli *et al. Phys. Rev. Lett.*, vol. **118**, p. 230403, 2017.

[130] A. Smerzi *et al. Phys. Rev. Lett.*, vol. **79**, p. 4950, 1997.

[131] I. Zapata, F. Sols, and A. J. Leggett *Phys. Rev. A*, vol. **57**, pp. R28–R31, 1998.

[132] S. Raghavan *et al. Phys. Rev. A*, vol. **59**, pp. 620–633, 1999.

[133] A. Salgueiro *et al. The European Physical Journal D*, vol. **44**, p. 537, 2007.

[134] R. Gati and M. K. Oberthaler *J. Phys. B: At. Mol. Opt. Phys.*, vol. **40**, p. R61, 2007.

[135] F. Piazza *et al. New Journal of Physics*, vol. **13**, p. 043008, 2011.

[136] F. Meier and W. Zwerger *Phys. Rev. A*, vol. **64**, p. 033610, 2001.

[137] E. Goldobin *et al. Phys. Rev. B*, vol. **76**, p. 224523, 2007.

[138] A. Spuntarelli *et al. Phys. Rev. Lett.*, vol. **99**, p. 040401, 2007.

[139] A. Spuntarelli, P. Pieri, and G. C. Strinati *Phys. Rep.*, vol. **488**, pp. 111–167, 2010.

[140] S. K. Adhikari, H. Lu, and H. Pu *Physical Review A*, vol. **80**, p. 063607, 2009.

[141] L. Salasnich *et al. Laser Physics*, vol. **19**, p. 636, 2009.

[142] F. Ancilotto, L. Salasnich, and F. Toigo *Physical Review A*, vol. **79**, p. 033627, 2009.

[143] M. Albiez *et al. Phys. Rev. Lett.*, vol. **95**, p. 010402, 2005.

[144] A. Burchianti *et al. Phys. Rev. Lett.*, vol. **120**, p. 025302, 2018.

[145] S. Giorgini *et al. Rev. Mod. Phys.*, vol. **80**, p. 1215, 2008.

[146] M. Albert *et al. Phys. Rev. Lett.*, vol. **100**, p. 250405, 2008.

[147] A. Buzdin and A. E. Koshelev *Phys. Rev. B*, vol. **67**, p. 220504(R), 2003.

[148] A. Barone and G. Paterno, *Physics and applications of the Josephson effect*. Wiley, 1982.

[149] G. E. Astrakharchik *et al. Phys. Rev. Lett.*, vol. **95**, p. 230405, 2005.

[150] A. Griffin, T. Nikuni, and E. Zaremba, *-Bose-condensed gases at finite temperatures-*. Cambridge University Press, 2009.

[151] I. Bloch, J. Dalibard, and W. Zwerger *Rev. Mod. Phys.*, vol. **80**, p. 885, 2008.

[152] L. Salasnich, N. Manini, and A. Parola *Phys. Rev. A*, vol. **72**, p. 023621, 2005.

[153] R. S. Lous *et al. Phys. Rev. A*, vol. **95**, p. 053627, 2017.

[154] B. Huang *et al. Phys. Rev. A*, vol. **99**, p. 041602(R), 2019.

[155] C. Ravensbergen *et al. Phys. Rev. A*, vol. **98**, p. 063624, 2018.

[156] J. Werner *et al. Phys. Rev. Lett.*, vol. **94**, p. 183201, 2005.

[157] J. Stuhler *et al. Journal of Modern Optics*, vol. **54**, no. 5, pp. 647–660, 2007.

[158] Y. Kim, M. J. Park, and M. J. Gilbert *Phys. Rev. B*, vol. 93, p. 214511, 2016.

[159] A. Q. Chen *et al. Nat. Comm.*, vol. 9, p. 3478, 2018.